



THE HONG KONG
POLYTECHNIC UNIVERSITY

香港理工大學

Pao Yue-kong Library

包玉剛圖書館

Copyright Undertaking

This thesis is protected by copyright, with all rights reserved.

By reading and using the thesis, the reader understands and agrees to the following terms:

1. The reader will abide by the rules and legal ordinances governing copyright regarding the use of the thesis.
2. The reader will use the thesis for the purpose of research or private study only and not for distribution or further reproduction or any other purpose.
3. The reader agrees to indemnify and hold the University harmless from and against any loss, damage, cost, liability or expenses arising from copyright infringement or unauthorized usage.

IMPORTANT

If you have reasons to believe that any materials in this thesis are deemed not suitable to be distributed in this form, or a copyright owner having difficulty with the material being included in our database, please contact lbsys@polyu.edu.hk providing details. The Library will look into your claim and consider taking remedial action upon receipt of the written requests.

**A GENERAL AND UNIFIED THEORY OF FLUX-
MODULATED ELECTRIC MACHINES AND ITS
APPLICATION TO INNOVATION OF MACHINE
TOPOLOGIES**

YIDUAN CHEN

PhD

The Hong Kong Polytechnic University

2020

The Hong Kong Polytechnic University

Department of Electrical Engineering

A General and Unified Theory of Flux-modulated Electric Machines
and its Application to Innovation of Machine Topologies

Yiduan Chen

A thesis submitted in partial fulfilment of the requirements for the
degree of Doctor of Philosophy

May 2019

CERTIFICATE OF ORIGINALITY

I hereby declare that this thesis is my own work and that, to the best of my knowledge and belief, it reproduces no material previously published or written, nor material that has been accepted for the award of any other degree or diploma, except where due acknowledgement has been made in the text.

Signed _____

January 2020

ABSTRACT

Electric machines (EMs) play a main role to convert mechanical and electrical energy interchangeably. As there are many EMs, small increment in the efficiency of energy conversion will save huge energy. Exploring novel EMs with high efficiency, high torque density, and low cost is always an interesting research topic.

In recent decades many different types of new EMs have emerged. Among others, these machines include a basic flux-modulated motor which uses the variation of magnetic reluctance to produce constant torque, a Vernier motor which has special slot combinations, a doubly-fed magnetic reluctance machine which has two sets of windings on its stator, a flux-switching motor which has permanent magnets (PMs) on its stator, a dual-PM-excited motor with PMs on both rotor and stator. These machines have their own merits in specific applications.

All these EMs follow a basic operating principle and it is possible to establish a general and unified theory for such types of machines. As the operating principle of these machines is relatively new and the combinations of variation of different topologies are large, there is a great possibility to invent more novel machines. In this thesis, a general theory, which can explain the operating principle of all these machines, is introduced. The unified design guidelines are employed to design and construct new motors.

The thesis mainly includes the following contents.

a) A literature review on the development of different types of magnetic gears and flux-modulated (FM) machines is present. FM machines include magnetic-gear machines, basic FM machines, Vernier machines, doubly-fed magnetic reluctance machines, stator flux-switching machine, and dual-permanent-magnet machines.

b) The internal relationships and operating mechanisms of general flux-modulated machines (GFMMs), which all employ non-uniform magnetic reluctance to modulate their

magnetic flux to produce constant torque, are studied. A general theory to explain the operating principle of all these FM machines is proposed.

c) Based on the proposed general theory, a doubly-fed dual-stator (DFDS) motor is presented. The performances of the machines are evaluated by finite-element method (FEM) of magnetic field. A prototype is made, and the test bench is established. Experimental results are presented to showcase the performance of the proposed DFDS motor.

d) To improve the torque capability, different PM arrangements of a dual-layer PM-excited (DPME) synchronous motor are compared. The configurations of the PM arrangement in the motors are designed in general patterns and optimized by a multi-objective genetic algorithm. A novel triple-layer PM-excited (TPME) synchronous motor is further presented, which has tactfully integrated the three parts of flux-modulated motors inside one frame with one shared set of armature windings.

e) A dual-electrical-port synthetic-slot permanent-magnet (SSPM) motor is proposed. With dual-airgap configuration the torque capability of the SSPM motor can be improved by virtue of the increased total area of air-gap surface. A new general pattern of a synthetic-slot structure, containing copper, permanent magnets, ferromagnetic materials, and insulators, is put forward and ingeniously employed to boost the torque density of the proposed SSPM motor. The simulation results using FEM are discussed and verified by experimental results of a prototype and vehicle-test results.

PUBLICATIONS ARISING FROM THE THESIS

Journal Papers:

- [1] Yiduan Chen, W. N. Fu, S. L. Ho, and Huijuan Liu, "A quantitative comparison analysis of radial-flux, transverse-flux and axial-flux magnetic gears," *IEEE Trans. Magn.*, vol. 50, no. 11, Nov. 2014, Art. no. 8104604.
- [2] Weinong Fu and Yiduan Chen, "Data structures and program techniques of finite element methods for analysis and optimization of electric devices," *Int. J. Appl. Electromagnet. Mech.*, vol. 47, no. 4, pp. 875-883, 2015.
- [3] W. N. Fu, Yiduan Chen, and Xinhua Guo, "Novel dual-layer and three-layer permanent-magnet-excited synchronous motors," *IEEE Trans. Magn.*, vol. 51, no. 11, Nov. 2015, Art. No. 8108404.
- [4] Yiduan Chen and Weinong Fu, "A novel hybrid-flux magnetic gear and its performance analysis using the 3-D finite element method," *Energies*, vol. 8, no. 5, pp. 3313-3327, 2015.
- [5] W. N. Fu and Yiduan Chen, "A post-assembly magnetization method for a line-start permanent-magnet motor," *IEEE Trans. Appl. Supercond.*, vol. 26, no. 4, June 2016, Art. no. 0602604.
- [6] Yiduan Chen, W. N. Fu and Wei Li, "Performance analysis of a novel triple-permanent-magnet-excited magnetic gear and its design method," *IEEE Trans. Magn.*, vol. 52, no. 7, July 2016, Art. No. 8001304.
- [7] Yiduan Chen, W. N. Fu and Xu Weng, "A concept of general flux-modulated electric machines based on a unified theory and its application to developing a novel doubly-fed dual-stator motor," *IEEE Trans. Ind. Electron.*, vol. 64, no. 12, pp. 9914-9923, Dec. 2017.

- [8] Yiduan Chen, W. N. Fu and Xu Weng, "A dual-electrical-port PM motor with synthetic slots for in-wheel direct drive of electric vehicles," *IEEE Trans. Ind. Electron.*, Jan. 2019, under revised.

Conference Papers:

- [1] W. N. Fu, and Yiduan Chen, "A transient finite element method for power electronic driven electric machines," *5th Int. Conf. on Power Electron. Syst. Appl. (PESA)*, Hong Kong, Dec. 11-13, 2013.
- [2] W. N. Fu, and Yiduan Chen, "A convenient algorithm for circuit parameters of eddy-current field based on circuit-field coupling formulation," *5th Int. Conf. on Power Electron. Syst. Appl. (PESA)*, Hong Kong, Dec. 11-13, 2013.

ACKNOWLEDGEMENTS

I would like to express my most sincere gratitude and appreciation to my chief supervisor Prof. Weinong Fu for his great guidance and supervision on my study as well as constant encouragement during the last three years. I have learnt a lot from his attitude and dedication to academic activities. I would also like to deliver my gratitude to Dr. Shuangxia Niu for her help on my work.

Many thanks are also given to all the students and research assistants in my research team for their support, encouragement and opinions, most notably Dr. Yanpu Zhao, Dr. Lin Yang, Dr. Yulong Liu, Dr. Yunchong Wang, Mr. Linghan Li, Dr. Tiantian Sheng, Mr. Xing Zhao, Mr. Yunpeng Zhang, Mr. Huihuan Wu, Miss Xu Weng, Mr. Shaozhe Wu, Mr. Jinyuan Fu.

I wish to thank my family for their constant understanding and encouragement as well as support. My special gratitude goes to my husband Mr. Runtian Guo, who always supports me for every choice I make. Without these, this work would have been much more difficult.

Table of contents

CERTIFICATE OF ORIGINALITY	III
ABSTRACT	IV
PUBLICATIONS ARISING FROM THE THESIS	VI
ACKNOWLEDGEMENTS	VIII
Chapter 1 Introduction	1
1.1 Background.....	1
1.2 Review of magnetic gears.....	2
1.3 Review of flux modulated machines	5
1.3.1 Magnetic-gearred machine.....	6
1.3.2 Basic flux-modulated machine	7
1.3.3 Vernier machine.....	8
1.3.4 Doubly-fed magnetic reluctance machine	10
1.3.5 Stator flux-switching machine	13
1.3.6 Dual-PM-excited machine	15
1.4 Research objectives	17
1.5 Thesis outline.....	18
Reference Part A	19
Chapter 2 Unified theory of flux-modulated machines	24
2.1 Introduction	24
2.2 Unified theory of flux-modulated machines.....	25
2.2.1 Basic flux-modulated motor	31

2.2.2 Flux-switching motor	32
2.2.3 Vernier motor	32
2.2.4 Dual-PM-excited motor.....	33
2.3 Conclusion.....	35
Reference Part B.....	35
Chapter 3 Analysis of a doubly-fed dual-stator flux-modulated motor	36
3.1 Introduction	36
3.2 The operating theory of the proposed DFDS motor.....	37
3.3 Optimization of the proposed DFDS motor	40
3.3.1 Optimization of the pole-pair/slot combination	41
3.3.2 Optimization of parameters	42
3.3.3 Performance analysis.....	45
3.4 The experiment results of the DFDS motor	48
3.4.1 The test platform	48
3.4.2 No-load test	50
3.4.3 Loaded test	54
3.5 Conclusion.....	57
Reference Part C.....	57
Chapter 4 Design and optimization of PM arrangement for a DPME synchronous motor	60
4.1 Introduction	60
4.2 DPME motors with different PM arrangement	61
4.2.1 Conventional PM arrangement.....	61

4.2.2	Simplified consequent-pole Halbach array PM arrangement.....	63
4.2.3	Spoke type PM arrangement.....	65
4.3	Optimization of the DPME motors.....	66
4.4	Performance comparison	68
4.4.1	Torque waveforms	68
4.4.2	Back EMF.....	69
4.4.3	Space harmonics	70
4.4.4	Torque comparison	71
4.4.5	Losses and efficiency comparison	72
4.4.6	Flux and magnetic field distribution.....	72
4.5	Conclusion.....	74
	Reference Part D.....	74
Chapter 5	Three-layer PM-excited synchronous motor.....	77
5.1	Introduction	77
5.2	Configurations	78
5.2.1	Conventional PM synchronous motor	78
5.2.2	Conventional DPME synchronous motor.....	79
5.2.3	New DPME synchronous motor	80
5.2.4	Novel TPME synchronous motor	81
5.3	Working principle	82
5.4	Performance analysis.....	85
5.4.1	Torque waveforms	86
5.4.2	Flux line contours	86

5.4.3 Comparison of torque density	88
5.4.4 Losses and efficiency comparison.....	88
5.5 Conclusion.....	89
Reference Part E.....	90
Chapter 6 Dual-electrical-port synthetic-slot PM motor.....	92
6.1 Introduction	92
6.2 Machine configurations.....	94
6.3 Working principle of the SSPM motor.....	96
6.4 Design and optimization of the SSPM motor.....	97
6.4.1 Excitation distribution of the two sets of windings	97
6.4.2 Relative position between the inner rotor and the outer rotor	100
6.4.3 Optimization of parameters	101
6.5 Simulation results and analysis	104
6.5.1 Performance comparison	104
6.5.2 Optimized configuration.....	104
6.5.3 Torque and induced voltage	106
6.5.4 Harmonics analysis.....	107
6.5.5 Flux and magnetic field distributions	108
6.6 Prototype and experimental investigation	109
6.6.1 Prototyped SSPM motor.....	109
6.6.2 Designed EV frame	110
6.6.3 Test bench and real EV frame	111
6.6.4 Back EMF.....	112

6.6.5 Inductance test	119
6.6.6 No-load mechanical loss	119
6.6.7 Loaded winding current	120
6.6.8 Mechanical characteristic	122
6.6.9 Efficiency map	123
6.6.10 On-vehicle test	123
6.7 Conclusion	124
Reference Part F	125
Chapter 7 Summary and future work	128
7.1 Summary	128
7.2 Future work	130

LIST OF FIGURES

Fig. 1.1. Magnetic gears (MGs). (a) Radial-flux MG [A3]. (b) Flux-focusing radial-flux MG [A4]. (c) Transverse-flux MG [A10]. (d) Axial-flux MG [A7]. (e) MG with intersecting axes [A9]. (f) Hybrid-flux MG [A11].	4
Fig. 1.2. Doubly-coupled magnetic gears [A13].	5
Fig. 1.3. Configuration of an outer-rotor magnetic-gear machine [A14].	6
Fig. 1.4. Configuration of a magnetically coupled magnetic-gear machine [A16].	7
Fig. 1.5. Configuration of a basic outer-rotor flux-modulated machine [A17].	8
Fig. 1.6. Different configurations of Vernier machines [A20, A22]. (a) A Vernier reluctance motor. (b) A Vernier PM motor. (c) A dual-stator Vernier PM machine. (d) Split-pole type and open-slot type of the stator configurations.	10
Fig. 1.7. Configuration of a high-power-factor Vernier machine [A25].	10
Fig. 1.8. Configuration of a brushless doubly-fed reluctance machine [A27].	12
Fig. 1.9. Different configurations of reluctance rotors [A34].	12
Fig. 1.10. Configuration of a dual-stator doubly-fed machine [A31].	12
Fig. 1.11. Topologies of flux-switching (FS) machines [A37]. (a) Conventional FSPM machine with all poles wound. (b) Conventional FSPM machine with alternate poles wound. (c) Multitooth FSPM machine. (d) E-core FSPM machine.	14
Fig. 1.12. Configuration of a transverse flux FSPM machine [A38].	14
Fig. 1.13. Configuration of a conventional dual-PM-excited motor [A41].	16
Fig. 1.14. Configuration of a triple-PM-excited motor [A44].	16
Fig. 2.1. A magnetic gear.	25
Fig. 2.2. A basic radial flux-modulated motor.	31
Fig. 2.3. A flux-switching motor.	32
Fig. 2.4. A Vernier motor.	33

Fig. 2.5. A dual-PM-excited motor.	34
Fig. 3.1. The presented doubly-fed dual-stator (DFDS) motor.	38
Fig. 3.2. The flow chart of the pole-pair/slot combination optimization.....	42
Fig. 3.3. The flow chart of the parameter optimization.	43
Fig. 3.4. Radial flux density in the inner airgap.	46
Fig. 3.5. Radial flux density in the outer airgap.	46
Fig. 3.6. Flux line contour.	47
Fig. 3.7. Magnetic field distribution.	47
Fig. 3.8. The prototyped outer stator of the proposed DFDS motor.....	49
Fig. 3.9. The prototyped inner stator of the proposed DFDS motor.....	49
Fig. 3.10. The prototyped middle rotor of the proposed DFDS motor.....	49
Fig. 3.11. The test system of the proposed DFDS motor.....	50
Fig. 3.12. Measured and simulated induced voltage of the inner winding at the speed of 100 r/min.	51
Fig. 3.13. Measured and simulated induced voltage of the inner winding at the speed of 924 r/min.	52
Fig. 3.14. Measured and simulated induced voltage of the outer winding at the speed of 100 r/min.	52
Fig. 3.15. Measured and simulated induced voltage of the outer winding at the speed of 924 r/min.	53
Fig. 3.16. No-load mechanical loss.	54
Fig. 3.17. The mechanical characteristics of the proposed motor.	55
Fig. 3.18. Measured current and induced voltage in the inner winding at the speed of 218 r/min.	56
Fig. 3.19. Measured current and induced voltage in the outer winding at the speed of	

218 r/min.	56
Fig. 3.20. Measured current and induced voltage in the inner winding at the speed of 924 r/min.	56
Fig. 3.21. Measured current and induced voltage in the outer winding at the speed of 924 r/min.	57
Fig. 4.1. DPME synchronous motor with the conventional PM arrangement (Motor I).	61
Fig. 4.2. A conventional PM arrangement in the rotor of Motor I.	62
Fig. 4.3. DPME synchronous motor with simplified consequent-pole Halbach array PM arrangement inserted in the rotor (Motor II).	64
Fig. 4.4. A simplified consequent-pole Halbach array type PM arrangement in the rotor of Motor II.	64
Fig. 4.5. DPME synchronous motor with simplified consequent-pole Halbach PM arrangement inserted in the rotor and spoke type PMs in the stator slots (Motor III).	65
Fig. 4.6. A spoke type PM arrangement on the stator of Motor III.	66
Fig. 4.7. The optimization process.	67
Fig. 4.8. The electromagnetic torque waveforms of the three motor types.	69
Fig. 4.9. The no-load back EMF of Motor I.	69
Fig. 4.10. The no-load back EMF of Motor II.	69
Fig. 4.11. The no-load back EMF of Motor III.	70
Fig. 4.12. The harmonic spectra of flux density in the air gap. (a) Motor I. (b) Motor II. (c) Motor III.	71
Fig. 4.13. The flux and magnetic field distributions of Motor I.	73
Fig. 4.14. The flux and magnetic field distributions of Motor II.	73

Fig. 4.15. The flux and magnetic field distributions of Motor III.	74
Fig. 5.1. A conventional outer-rotor PM synchronous motor (Motor I).....	79
Fig. 5.2. A conventional DPME synchronous motor (Motor II).	80
Fig. 5.3. The proposed novel DPME synchronous motor (Motor III).....	81
Fig. 5.4. The proposed novel triple-PM-excited (TPME) synchronous motor (Motor IV).	82
Fig. 5.5. Torque at full-load operation with different configurations.	86
Fig. 5.6. Flux line contour of different configurations.	87
Fig. 6.1. A conventional PM motor.	95
Fig. 6.2. The proposed SSPM motor and partially enlarged detail.	95
Fig. 6.3. A general pattern of the synthetic-slot structure.....	96
Fig. 6.4. The output torque waveforms when only one set of windings is excited. ...	100
Fig. 6.5. The relative position of the inner rotor and the outer rotor.	101
Fig. 6.6. The output torque with different relative positions of the two rotors.	101
Fig. 6.7. The flow chart of the parameter optimization of the SSPM motor.	102
Fig. 6.8. The optimized configuration of the proposed SSPM motor and partially enlarged detail.....	105
Fig. 6.9. The schematic installation topology of the proposed SSPM motor.	105
Fig. 6.10. The output torque waveform.	106
Fig. 6.11. The induced voltage waveform of the windings.	106
Fig. 6.12. The induced voltage vs input current of the outer winding.....	107
Fig. 6.13. The induced voltage vs input current of the inner winding.....	107
Fig. 6.14. Radial flux density in the outer airgap.	108
Fig. 6.15. Radial flux density in the inner airgap.	108
Fig. 6.16. Flux line contour.	109

Fig. 6.17. Magnetic density distribution.	109
Fig. 6.18. The prototype of the proposed synthetic-slot PM motor.	110
Fig. 6.19. The model of the automobile framework and the connection structure between the wheel and the frame.	111
Fig. 6.20. The test system of the proposed SSPM motor.	112
Fig. 6.21. The real EV frame with the SSPM motors, the controllers and the power supply.	112
Fig. 6.22. The simulated and experimental no-load back EMF of the outer windings of the proposed SSPM motor when the speed is 100 r/min.....	113
Fig. 6.23. The simulated and experimental no-load back EMF of the inner windings of the proposed SSPM motor when the speed is 100 r/min.....	114
Fig. 6.24. The simulated and experimental no-load back EMF of the outer windings of the proposed SSPM motor when the speed is 200 r/min.....	115
Fig. 6.25. The simulated and experimental no-load back EMF of the inner windings of the proposed SSPM motor when the speed is 200 r/min.....	116
Fig. 6.26. The simulated and experimental no-load back EMF of the outer windings of the proposed SSPM motor when the speed is 300 r/min.....	117
Fig. 6.27. The simulated and experimental no-load back EMF of the inner windings of the proposed SSPM motor when the speed is 300 r/min.....	118
Fig. 6.28. The self and mutual inductance of the windings.	119
Fig. 6.29. The no-load mechanical loss of the proposed SSPM motor.	120
Fig. 6.30. The relationship of electromagnetic torque and the winding current.	121
Fig. 6.31. The winding current under load conditions when the speed is 100 r/min.	121
Fig. 6.32. The winding current under load conditions when the speed is 200 r/min.	121
Fig. 6.33. The winding current under load conditions when the speed is 300 r/min.	122

Fig. 6.34. The mechanical characteristic of the proposed SSPM motor.....	122
Fig. 6.35. The efficiency map of the proposed SSPM motor.	123
Fig. 6.36. The operation condition of the EV in low speed.....	124

LIST OF TABLES

Table 3.1 Key design data of the proposed DFDS motor.....	45
Table 3.2 Performances comparison of different motor structures	48
Table 3.3 The relation between frequencies and motor speed	55
Table 4.1 Main design parameters of DPME motors	62
Table 4.2 Design parameters of the PM arrangement in Motor I.....	67
Table 4.3 Design parameters of the PM arrangement in Motor II	67
Table 4.4 Design parameters of the PM arrangement in Motor III	68
Table 4.5 Torque comparison of different motor configurations	72
Table 4.6 Performance comparison of different motor configurations	72
Table 5.1 Key design data of a conventional PM synchronous motor (Motor I).....	79
Table 5.2 Main Design Parameters of the Motors.....	81
Table 5.3 Torque comparison of four configurations	88
Table 5.4 Performance comparison of four configurations.....	89
Table 6.1 Key design data of the proposed SSPM motor.....	103
Table 6.2 Performance of the proposed SSPM motor	104
Table 6.3 Peak to peak values of the no-load back EMF of the windings	118

LIST OF ABBREVIATIONS

BFM	Basic flux-modulated
DC	Direct current
DFDS	Doubly-fed dual-stator
DPME	Dual-layer PM-excited
EM	Electric machine
EV	Electric vehicle
FEM	Finite-element method
FM	Flux-modulated
GFMM	General flux-modulated machine
MMF	Magnetomotive force
MG	Magnetic gear
PM	Permanent magnet
PMBL	Permanent-magnet brushless
SSPM	Synthetic-slot permanent-magnet
TPME	Triple-layer PM-excited

Chapter 1 Introduction

1.1 Background

Electric machines (EMs) play a main role to convert mechanical and electrical energy interchangeably. As there are many EMs, small increment in the efficiency of energy conversion will save huge energy. Exploring novel EMs with high efficiency, high torque density, and low cost is always an interesting research topic. In recent decades many different types of new EMs have emerged. Among others, these machines include a basic flux-modulated motor which uses the variation of magnetic reluctance to produce constant torque, a Vernier motor which has special slot combinations, a doubly-fed magnetic reluctance machine which has two sets of windings on its stator, a flux-switching motor which has permanent magnets (PMs) on its stator, a dual-PM-excited motor with PMs on both rotor and stator. These machines have their own merits in specific applications. All these EMs follow a basic operating principle and it is possible to establish a general and unified theory for such types of machines. As the operating principle of these machines is relatively new and the combinations of variation of different topologies are large, there is a great possibility to invent more novel machines.

This thesis aims to study the internal relationships and operating mechanisms of the basic flux-modulated motor, Vernier motor, doubly-fed reluctance machine, flux-switching motor, and dual-PM-excited motor. Since they all employ non-uniform magnetic reluctance to modulate their magnetic flux to produce constant torque, a general theory, which can explain

the operating principle of all these machines, will be proposed. Unified design guidelines of these machines can quickly identify the efficacy of different combinations of pole-pairs of the windings, PMs, special ferromagnetic segments and teeth/slots, as well as ac/dc excitations and the rotating speeds of the rotors. As application examples, the developed method will be applied to design, construct and test new motors.

1.2 Review of magnetic gears

Magnetic gears (MGs) have fascinated and inspired many researchers as they offer substantial advantages compared to mechanical gears. MGs can realize torque transmission with speed reduction and torque amplification by a contactless mechanism with physical and hermetic isolation between input and output shafts. They have significant advantages of having reduced maintenance, improved reliability and minimal acoustic noise. MGs have inherent overload protection and have very competitive torque transmission capability and efficiency compared to their mechanical counterparts [A1-A2].

A radial-flux MG topology which combines a highly competitive torque transmission capability with very high efficiency is described in [A3]. It shows that the choices of design parameters have a significant influence on the torque transmission capability. A high performance PM gear is presented in [A4-A5] with calculation and measurement results using rotors made of spoke type instead of surface mounted type of PMs. From the calculated flux lines shown, these magnets however have a poor utilization, and large end-effects may exist. A transverse-flux MG is proposed in [A6] with radially magnetized PMs, which has unique merits in applications which require airproof and small vibration. In [A7] an axial-

flux MG is described, which is particularly suitable for applications requiring flat outside shapes and hermetic isolation between the input and output shafts. Another axial-flux MG is investigated in [A8], in which the ferrite magnets are arranged in a flux focusing configuration in order to increase the air-gap flux density. A MG with intersecting axes was proposed in [A9].

In [A10], the performances of three types of MGs, which are radial-flux MGs, transverse-flux MGs, and axial-flux MGs, are quantitatively analyzed and compared using three-dimensional (3-D) finite element method (FEM) of magnetic field and mechanical motion coupled computation. In [A11-A12], hybrid-flux MGs were proposed to achieve higher electromagnetic torque density and compared with the transverse-flux MG and the axial-flux MG. Fig. 1.1 shows several different configurations of MGs.

The basic MG, as shown in Fig. 1.1 (a), has three parts. The outer part has PMs rotating at the speed ω_1 with p_1 pole-pairs, and the inner part has PMs rotating at the speed ω_2 with p_2 pole-pairs. The middle part has ferromagnetic segments rotating at the speed ω_{Fe} with p_{Fe} pole-pairs. In the MG, usually the ferromagnetic segments are stationary, that means, $\omega_{Fe}=0$.

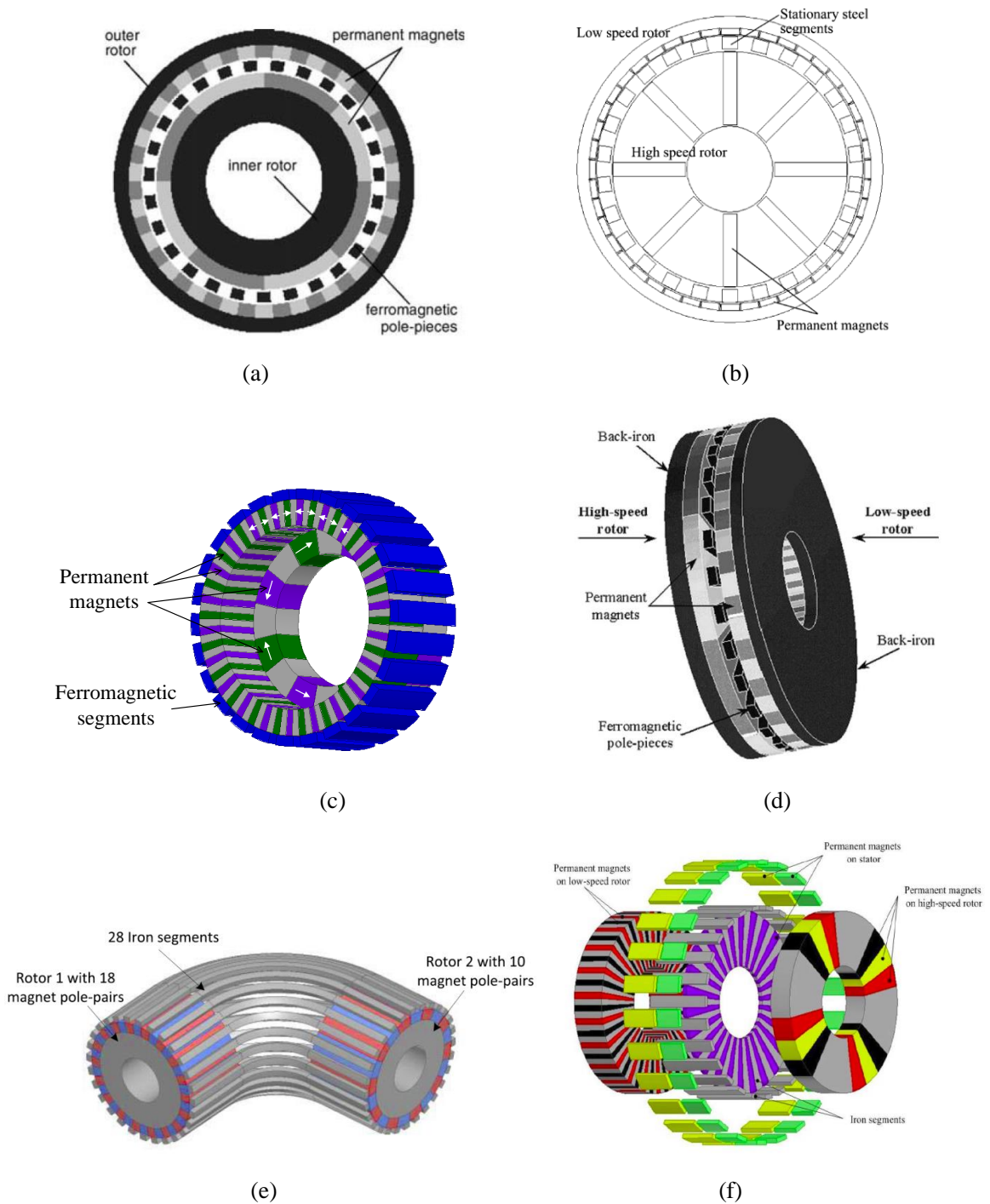


Fig. 1.1. Magnetic gears (MGs). (a) Radial-flux MG [A3]. (b) Flux-focusing radial-flux MG [A4]. (c) Transverse-flux MG [A10]. (d) Axial-flux MG [A7]. (e) MG with intersecting axes [A9]. (f) Hybrid-flux MG [A11].

A doubly-coupled MG was proposed in [A13]. Its topology is shown in Fig. 1.2. Inside this gear, one MG is the same as the conventional basic MG. Unlike the basic gear, the doubly-

coupled MG employs an extra stationary layer of PMs mounted between adjacent ferromagnetic segments and it has consequent PM poles in the outer rotor. The PMs in the middle part produce an extra set of magnetic field which is modulated by the magnetic reluctance of the outer rotor and reacts with the magnetic field produced by the PMs on the inner rotor to produce additional transmitted torque. That means, it constitutes another pair of MG inside the original volume. The two MGs can all work simultaneously. The proposed structure makes full use of the free space among ferromagnetic segments. The salient merit of the proposed gear is that it can transmit a bigger torque with the same overall volume.

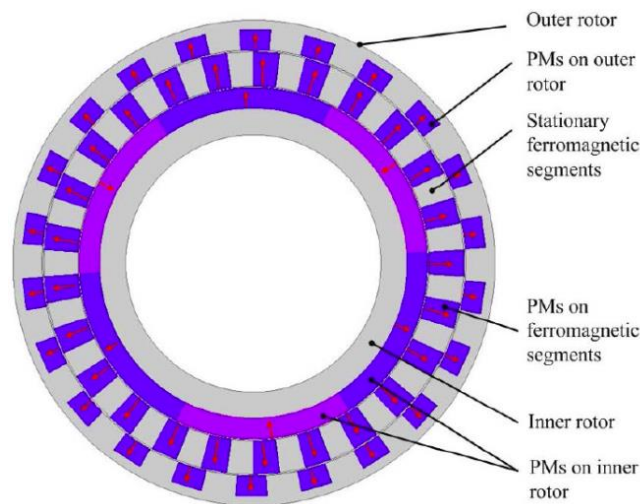


Fig. 1.2. Doubly-coupled magnetic gears [A13].

1.3 Review of flux modulated machines

Electric machines (EMs) play an important role to convert mechanical and electrical energy interchangeably. About half of the global electricity being generated is consumed by electric motors. If the power efficiency of all motors increases by 1%, the saving is enough for supplying electricity to 9.2 million families over a whole year. Ideally EMs should have high efficiency, small volume/weight and low cost. In recent decades many different EMs have

emerged, which provide the much-needed diverging topology variations and the possibility to develop new machines. These machines are described briefly as follows.

1.3.1 Magnetic-geared machine

Since the outstanding features of magnetic gears have been attracting increasing attentions, the concept of replacing mechanical gearboxes with MGs for non-contact torque transmission has driven researchers to put forward various innovative machine designs. A magnetic-geared outer-rotor PM motor, as shown in Fig. 1.3, which directly integrates a magnetic gear with a conventional outer-rotor permanent-magnet brushless (PMBL) DC motor, was proposed in [A14]. The MG and the PMBL DC motor can share a common PM rotor. The operating principle and mathematical modeling are detailed in [A15]. The integrated structure realizes both the low-speed requirement for direct driving and the high-speed requirement for motor operating. However, the complicated mechanical structure may make it difficult to be processed. In [A16], a magnetic gear and a PM brushless machine are coupled together both mechanically and magnetically, as shown in Fig. 1.4. The mechanical structure has been simplified to some extent.

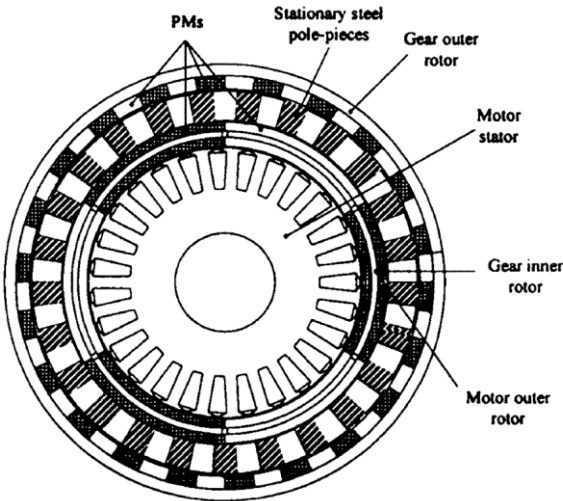


Fig. 1.3. Configuration of an outer-rotor magnetic-geared machine [A14].

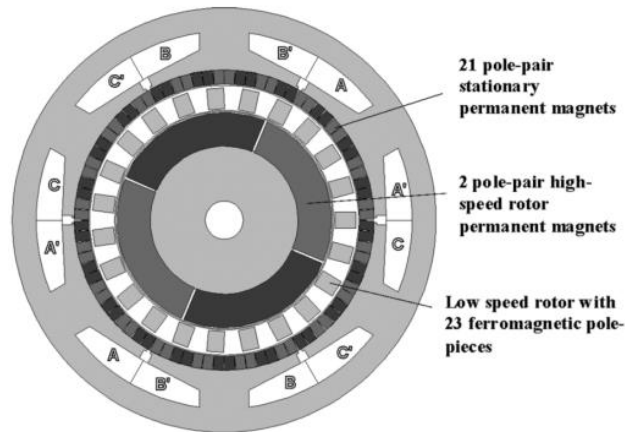


Fig. 1.4. Configuration of a magnetically coupled magnetic-geared machine [A16].

1.3.2 Basic flux-modulated machine

With further simplification of the magnetic-geared machine, an outer-rotor basic flux-modulated (BFM) motor was proposed for low-speed direct drive [A17] and its analytical modeling can be found in [A18]. The BFM motor has a stator with a set of three-phase windings and a rotor with permanent magnets (PMs). Between the stator and rotor, a set of stationary ferromagnetic segments is sandwiched, as shown in Fig. 1.5. The magnetic field produced by the PMs is modulated by the ferromagnetic segments and reacts with the magnetic field produced by the armature [A19]. The main merits of the BFM motor are that the number of pole-pairs of the armature windings can be small while the number of the pole-pairs of the PM rotor can be large, which is especially suitable for low-speed drive such as in-wheel motors in electric vehicles (EVs) and wind power generators. The naturally formed space between the ferromagnetic segments can be used as ventilating ducts for improving heat dissipation.

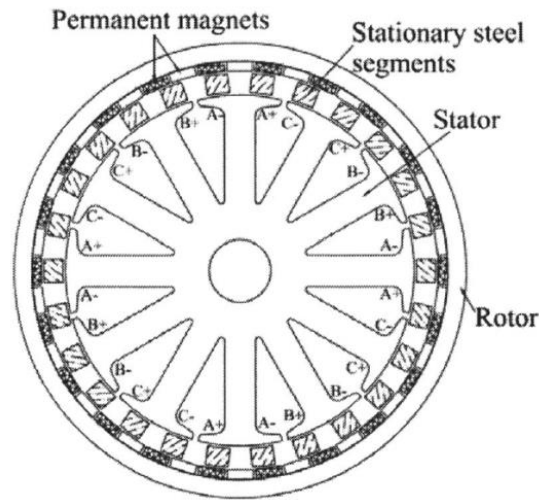
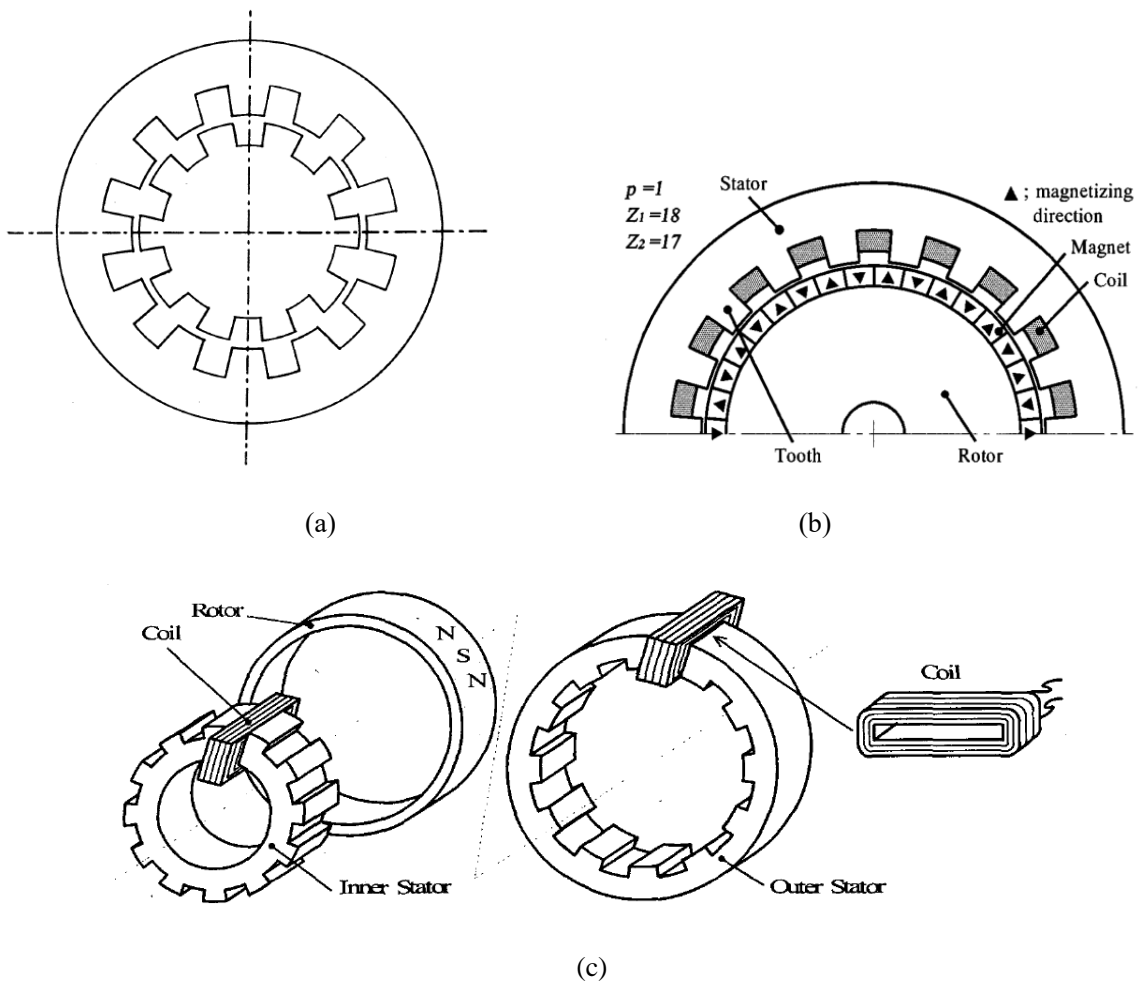


Fig. 1.5. Configuration of a basic outer-rotor flux-modulated machine [A17].

1.3.3 Vernier machine

A Vernier reluctance motor, as shown in Fig. 1.6 (a), was firstly presented in 1963 [A20]. With the advent of PM materials, a Vernier PM motor, as shown in Fig. 1.6 (b), was developed in the early 90s [A21]. The Vernier PM motor has different numbers of pole-pairs in the three-phase armature windings on the stator and PMs on the rotor. Its open-slot structure on the stator produces non-uniform magnetic reluctance. Fig. 1.6 (c) shows a dual-stator Vernier PM machine with the concept of dual excitation which was proposed in [A22] to improve its torque density. Fig. 1.6 (d) presents two types of the stator configurations, split-pole type and open-slot type. The results show that the open-slot type is more suitable for high power machines. Outer rotor Vernier PM machines were used for in-wheel propulsion of EVs and direct-drive wind power generation [A23-A24]. Fig. 1.7 displays a recent research which presented a dual-stator topology, whose inner stator teeth have half tooth displacement relative to the outer stator teeth and spoke-array of PMs is used to produce flux focusing effect. Its power factor can reach 0.9 [A25].

In the basic flux-modulated motor, if the stationary ferromagnetic segments are combined with the stator together, it is a Vernier motor. The open-slot structure is adopted to modulate the magnetic field in the airgap. A Vernier motor can be considered as a special situation of the basic flux-modulated motor when the number of stator slots and the number of ferromagnetic segments are the same. Compared with the basic flux-modulated motor, it has a simple structure at the expense of losing the flexible choice of the number of ferromagnetic segments.



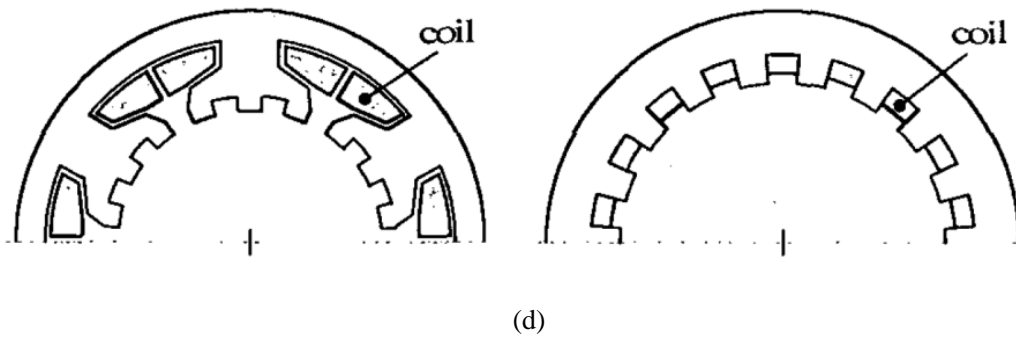


Fig. 1.6. Different configurations of Vernier machines [A20, A22]. (a) A Vernier reluctance motor. (b) A Vernier PM motor. (c) A dual-stator Vernier PM machine. (d) Split-pole type and open-slot type of the stator configurations.

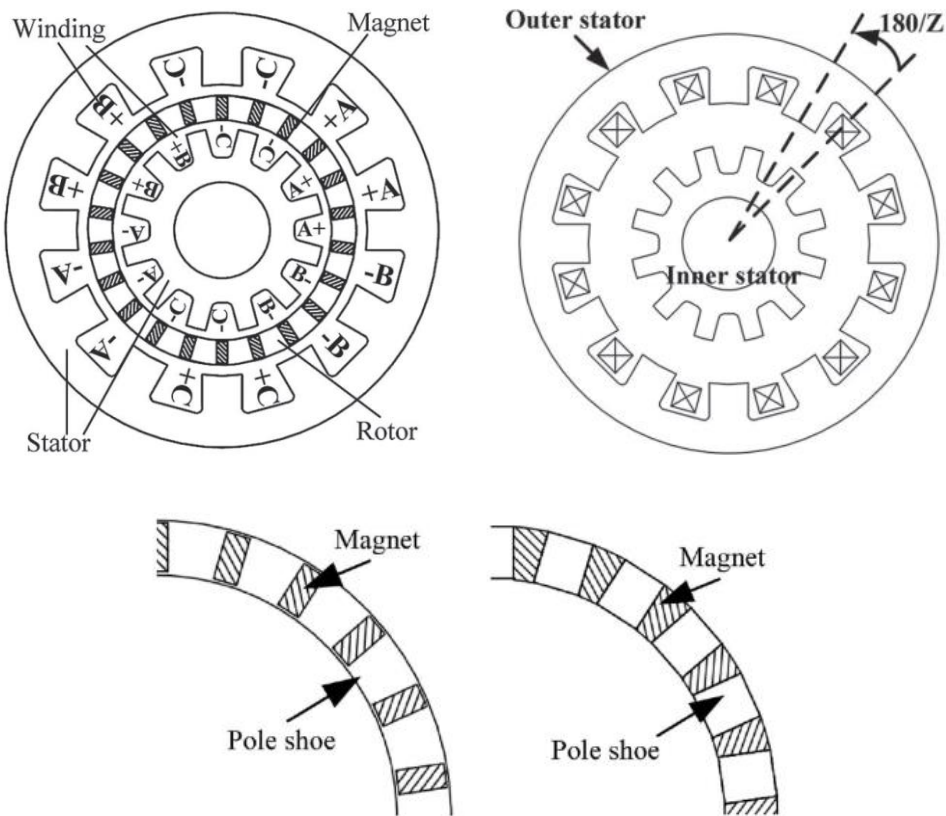


Fig. 1.7. Configuration of a high-power-factor Vernier machine [A25].

1.3.4 Doubly-fed magnetic reluctance machine

The stator of a doubly-fed magnetic reluctance machine has two sets of three-phase windings

with different numbers of pole-pairs and different frequencies [A26-A28]. The rotor has a salient pole structure. It has no brushes nor slip rings. The magnetic field produced by one set of windings is modulated by the salient poles on the rotor and reacts with the magnetic field produced by another set of stator windings. The relationship among the number of pole-pairs of the first set of windings p_1 with frequency f_1 , the number of pole-pairs of the second set of windings p_2 with frequency f_2 , and the rotor speed ω_r , follows: $\omega_r = 2\pi (f_1 \pm f_2) / (p_1 + p_2)$. Fig. 1.8 shows a brushless doubly-fed reluctance generator and Fig. 1.9 displays two types of reluctance rotors (reluctance rotor with simple salient poles and segment reluctance rotor with magnetic barriers). If the machine is used as a motor, it has a wide speed range [A29]; if the machine is used as a generator, it can realize constant-frequency output power with variable rotor speed [A30]. When compared with a conventional PM machine with a full-scale convertor for variable speed control, the doubly-fed machine only needs a partial-scale convertor, which significantly reduces the overall cost. However, the power factor of this machine is relatively low.

In the basic MG, if the rotating magnetic field of the outer part is produced by a set of stationary three-phase windings with the pole-pairs p_1 and frequency f_1 , and the rotating magnetic field of the inner part is produced by a set of stationary three-phase windings with pole-pairs p_2 and frequency f_2 , and the ferromagnetic segments rotate at the speed ω_{Fe} , it becomes a dual-stator doubly-fed magnetic reluctance machine. Based on this principle, a novel dual-stator doubly-fed machine was proposed in [A31]. It has a set of windings on the outer stator and another set of windings on the inner stator to fully use the inner space, as shown in Fig. 1.10. Compared with conventional doubly-fed machines, it has less copper loss. The conventional doubly-fed machines [A32-A33] can be considered as a special case with the two sets of windings being installed on the outer stator.

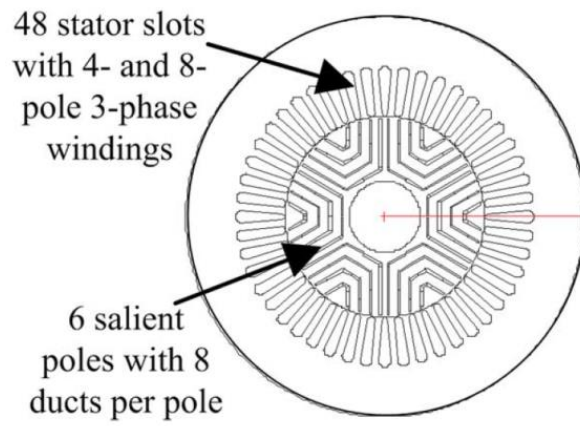


Fig. 1.8. Configuration of a brushless doubly-fed reluctance machine [A27].

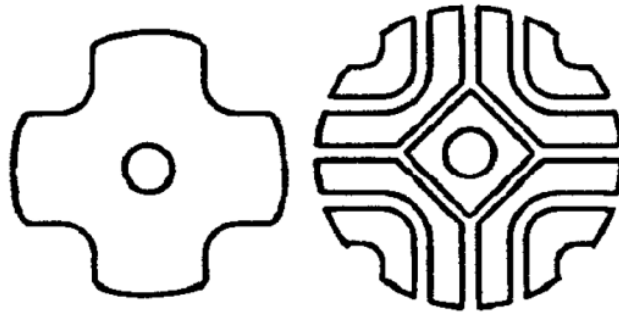


Fig. 1.9. Different configurations of reluctance rotors [A34].

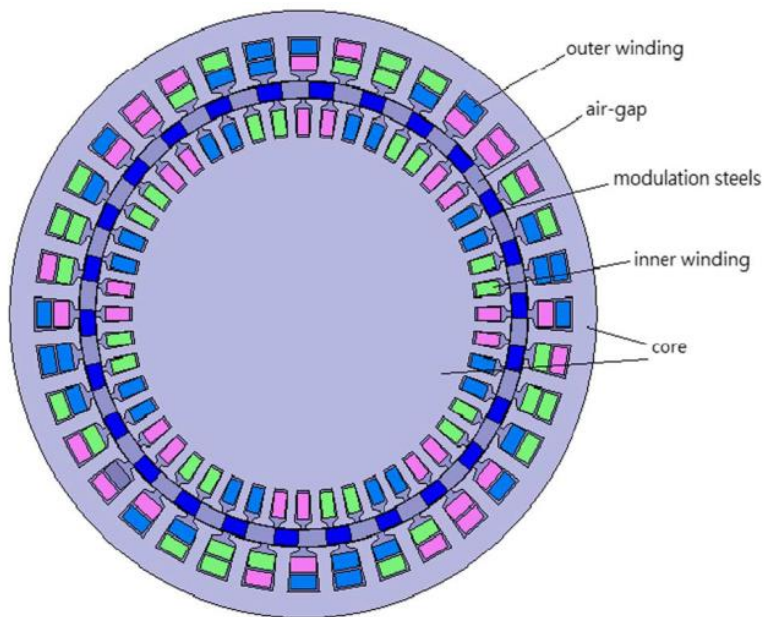


Fig. 1.10. Configuration of a dual-stator doubly-fed machine [A31].

1.3.5 Stator flux-switching machine

A stator flux-switching motor has three-phase windings on its stator. The rotor has a salient-pole structure. In contrast to conventional PM machines, it has PMs on its stator [A35-A36]. The magnetic field produced by the PMs on the stator is modulated by the salient poles on the rotor and reacts with the armature field to produce constant torque. The accommodation of both windings and the PMs on the stator is beneficial to cooling and the PMs are free from the centrifugal force. By virtue of its robust rotor structure, it is especially suitable for high speed motors. Flux-switching linear motors can significantly reduce the usage of PM materials. Various topologies have been proposed for low-speed applications such as in robots, wind power generation and EVs [A37-A38]. The flux-switching motor can be designed to have good flux-weakening capability as the flux linkage produced by its armature does not pass through the magnets [A39]. The main drawback of the flux-switching motor is its low PM utilization [A40]. Fig. 1.11 and Fig. 1.12 show several topologies of flux-switching PM motor.

In the basic MG, if the rotating magnetic field of the outer part with the speed $\omega_1 = 2\pi f_1 / p_1$ is produced by a set of stationary three-phase windings with pole pairs p_1 and frequency f_1 , the PMs on the inner part are stationary and combined with the outer part, the ferromagnetic segments rotate with the speed ω_{Fe} , the machine is a flux-switching motor. The speed of the rotor is $\omega_{Fe} = (p_1\omega_1 \pm p_2\omega_2) / p_{Fe} = 2\pi f_1 / p_{Fe}$.

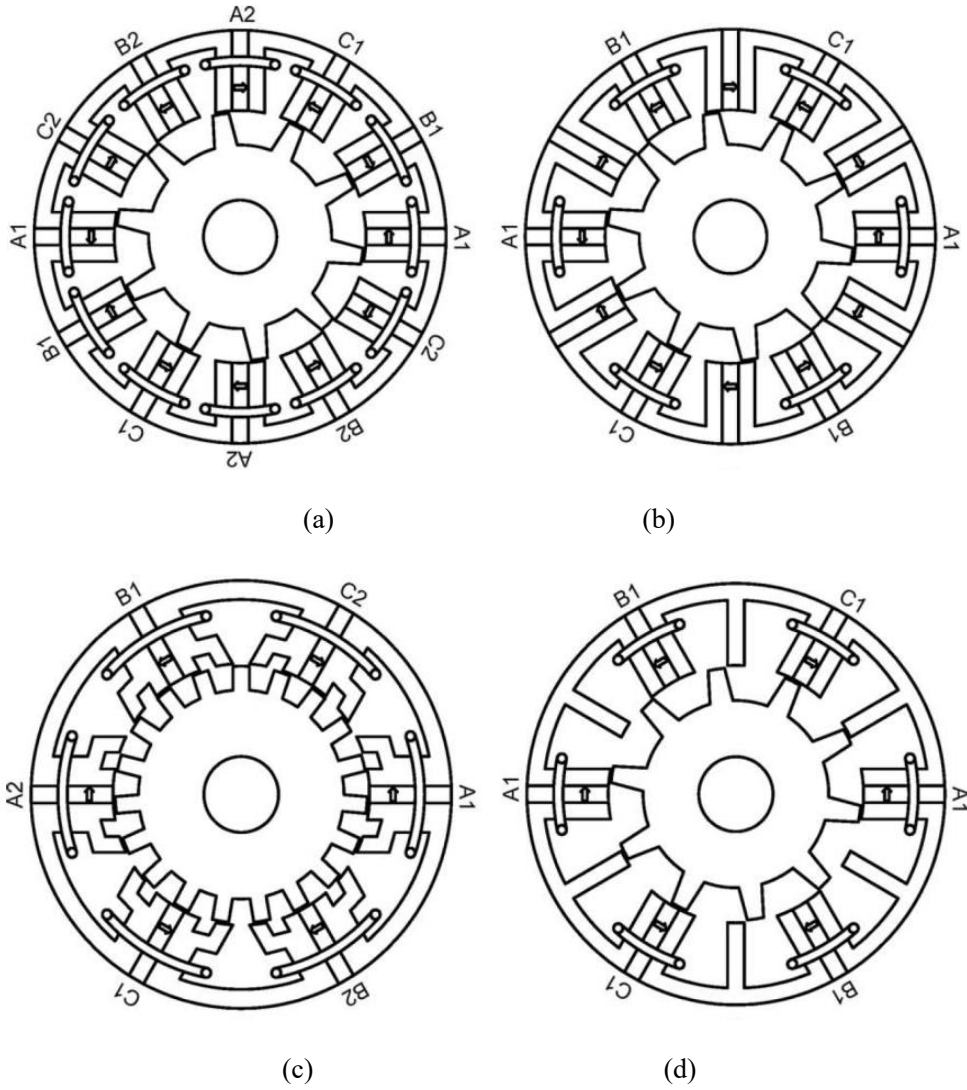


Fig. 1.11. Topologies of flux-switching (FS) machines [A37]. (a) Conventional FSPM machine with all poles wound. (b) Conventional FSPM machine with alternate poles wound. (c) Multitooth FSPM machine. (d) E-core FSPM machine.

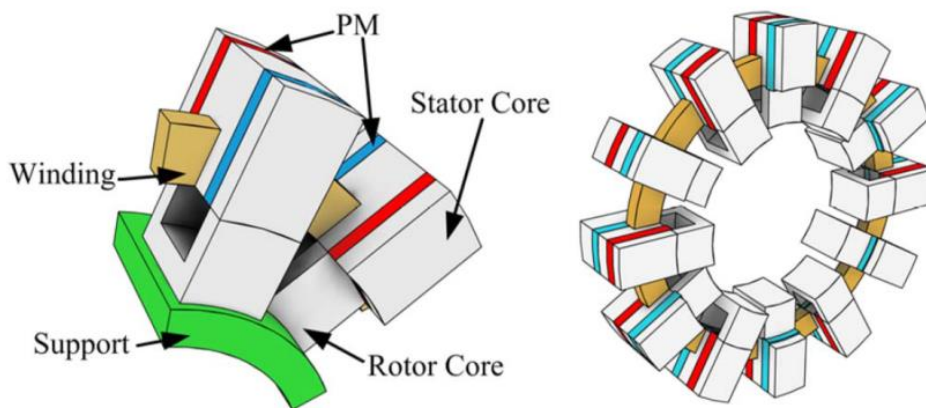


Fig. 1.12. Configuration of a transverse flux FSPM machine [A38].

1.3.6 Dual-PM-excited machine

Like other PM machines, a dual-PM-excited motor, as shown in Fig. 1.13, has a set of three-phase windings on its stator. Unlike conventional rotor-PM motors and stator-PM motors, the dual-PM-excited motor has PMs on both rotor and stator [A41-A42]. An open-slot structure is employed in the stator to modulate the magnetic field produced by the PMs on the rotor. The function of the open-slot structure can also be realized by a set of stationary ferromagnetic segments which is sandwiched between the stator and rotor [A43]. It has a consequent-pole PM rotor. Because of the iron teeth between the PMs on the rotor, the rotor has a salient-pole structure. In this machine, the flux modulation effect is achieved in two ways. Both the rotor PMs and stator PMs can interact with the windings via the stator teeth and rotor teeth, respectively. The stator windings and the PMs on the stator and the salient rotor constitute a flux-switching motor; the stator windings and the tooth-slot effect of the stator and the PMs on the rotor constitute a Vernier motor [A44]. The torque density of this machine is higher than when only one set of PMs is being used. According to this concept, a triple-PM-excited motor was proposed in [A44]. Unlike conventional DPME structures, it has one outer stator and one inner stator arranged along the radial direction. The additional inner stator carries surface mounted PMs and it also has an open-slot structure, as shown in Fig. 1.14.

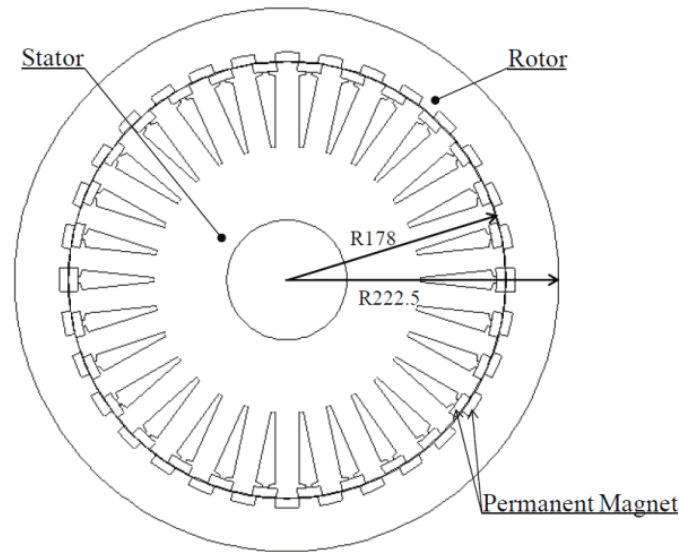


Fig. 1.13. Configuration of a conventional dual-PM-excited motor [A41].

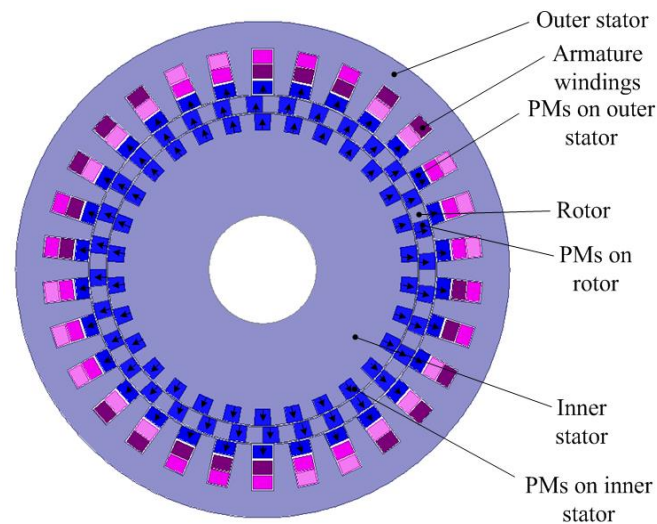


Fig. 1.14. Configuration of a triple-PM-excited motor [A44].

There are a lot of topology variations among these machines. Each machine was generally studied separately and reported in different literatures. Past studies lack a high-level principle to examine their internal relationships. It is very difficult for designers to choose the most suitable topologies as each one has its merits and demerits. For each specific application, the design should be optimized not only for its design parameters such as geometric sizes and numbers of winding turns, but also its type of machines and its topology. Therefore, the

regularity of topology variations among these EMs need to be examined. A design scheme, which uses a general and unified model to optimize these EMs with a general pattern of PM arrangement, is proposed.

Based on the above discussions, all topologies of basic flux-modulated motor, Vernier motor, flux-switching motor, and dual-PM-excited motor can be considered as special situations of general flux-modulated machines (GFMMs). All these machines can be derived from the MG. Therefore, a general and unified model of GFMMs can be established, with the following possible topologies: (1) Each part can be stationary or rotary. (2) Each part can have one or two sets of windings with ac/dc power connections. The slots can be split-pole, open-slot structure with variable airgap permeance for flux modulation. (3) The PMs can be arranged in different ways: surface mounted PM, spoke-type PM, V-type PM, and consequent PM poles which have the function of flux modulation. The PMs can also be located at different places. (4) The machine may have single/double stator, single/double rotor. The single rotor can be arranged in two separate parts to produce a two-airgap structure [A45]. (5) A GFMM and a conventional PM machine or a MG may be integrated together [A46-49].

1.4 Research objectives

The main objectives of this thesis include the following aspects:

(1) A general and unified theory of general flux modulated machines (GFMMs), which can explain the operating principle of basic flux-modulated motor, Vernier motor, doubly-fed magnetic reluctance machine, flux-switching motor, and dual-PM-excited motor, will be

developed. Design guidelines of GFMMs will be presented.

(2) Based on the developed general theory, a computer program which can automatically find possible topologies will be developed. The developed general theory of GFMMs will be served as initial fast screening of possible topology combinations.

(3) A finite-element model of the proposed machines which couples magnetic field, power electronic circuit, mechanical motion and thermal field, will be developed to quantitatively compare the performances of the machines. Their merits and demerits will be comprehensively identified.

(4) A multi-objective hybrid optimal design method for GFMMs will be developed. The design parameters include topology indices, geometric sizes, PM arrangement and windings.

(5) The developed method will be applied to design an in-wheel motor for direct-drive of EVs. The topology having the best overall performances will be constructed and extensively tested to verify the design concept against theoretical analysis and computer simulations.

1.5 Thesis outline

The thesis aims to study the operating theory of general flux-modulated machines and apply the unified theory to the innovation of machine topologies. The pros and cons are concluded through the study. Chapter 1 gives an overview of various types of magnetic gears and flux-modulated machines, including their historical development and brief working principles.

Chapter 2 presents a general and unified theory of general flux-modulated machines which is derived from a radial-flux magnetic gear model. The proposed theory can be used to explain the operating principles of the different types of flux-modulated machines. Chapter 3 presents a doubly-fed dual-stator (DFDS) motor, which is designed for in-wheel EV drive based on the unified theory proposed in Chapter 2. The DFDS motor is prototyped and tested for performance validation. In Chapter 4, the PM arrangements in a dual-layer PM-excited (DPME) motor are designed and optimized for having more competitive torque capability and higher efficiency. A novel three-layer PM-excited (TPME) motor is derived further, which has the merit of having higher torque density than conventional synchronous motors and the DPME motor. In Chapter 5, a dual-electrical-port synthetic-slot PM (SSPM) motor is designed with wide speed range for direct-drive in-wheel EV application. Two machine prototypes are manufactured, and experimental tests are conducted to verify the electromagnetic design. Chapter 6 gives the conclusions and recommendations for further study.

Reference Part A

- [A1] T. Lubin, S. Mezani, and A. Rezzoug, "Analytical computation of the magnetic field distribution in a magnetic gear," *IEEE Trans. Magn.*, vol. 46, no. 7, pp. 2611-2621, 2010.
- [A2] K. T. Chau, D. Zhang, J. Z. Jiang, and L. Jian, "Transient analysis of coaxial magnetic gears using finite element comodeling," *J. Appl. Phys.*, vol. 103, no. 7, p. 07F101, 2008.
- [A3] K. Atallah, S. D. Calverley, and D. Howe, "Design, analysis and realisation of a high-performance magnetic gear," *IEE Proc.: Electr. Power Appl.*, vol. 151, no. 2, pp. 135-143, 2004.
- [A4] P. O. Rasmussen, T. O. Andersen, F. T. Jorgensen, and O. Nielsen, "Development of a high-performance magnetic gear," *IEEE Trans. Ind. Appl.*, vol. 41, no. 3, pp. 764-770, 2005.
- [A5] K. Uppalapati and J. Bird, "A flux focusing ferrite magnetic gear," in *6th IET Int. Conf. Power*

Electron. Mach. Drives (PEMD 2012), 27-29 Mar. 2012, Bristol, UK.

- [A6] L. Yong, X. Jing-Wei, L. Yong-Ping, and Y. Zhi-Jun, "Torque analysis of a novel non-contact permanent variable transmission," *IEEE Trans. Magn.*, vol. 47, no. 10, pp. 4465-4468, 2011.
- [A7] S. Mezani, K. Atallah, and D. Howe, "A high-performance axial-field magnetic gear," *J. Appl. Phys.*, vol. 99, no. 8, p. 08R303, 2006.
- [A8] V. M. Acharya, J. Z. Bird, and M. Calvin, "A flux focusing axial magnetic gear," *IEEE Trans. Magn.*, vol. 49, no. 7, pp. 4092-4095, 2013.
- [A9] Y. Liu, S. L. Ho, and W. N. Fu, "A novel magnetic gear with intersecting axes," *IEEE Trans. Magn.*, vol. 50, no. 11, p. 8001804, 2014.
- [A10] Y. Chen, W. N. Fu, S. L. Ho, and H. Liu, "A quantitative comparison analysis of radial-flux, transverse-flux, and axial-flux magnetic gears," *IEEE Trans. Magn.*, vol. 50, no. 11, p. 8104604, 2014.
- [A11] S. Peng, W. N. Fu, and S. L. Ho, "A novel triple-permanent-magnet-excited hybrid-flux magnetic gear and its design method using 3-D finite element method," *IEEE Trans. Magn.*, vol. 50, no. 11, p. 8104904, 2014.
- [A12] Y. Chen and W. N. Fu, "A novel hybrid-flux magnetic gear and its performance analysis using the 3-D finite element method," *Energies*, vol. 8, no. 5, pp. 3313-3327, 2015.
- [A13] S. Peng, W. N. Fu, and S. L. Ho, "A novel high torque-density triple-permanent-magnet-excited magnetic gear," *IEEE Trans. Magn.*, vol. 50, no. 11, p. 8001704, 2014.
- [A14] K. T. Chau, D. Zhang, J. Z. Jiang, C. Liu, and Y. Zhang, "Design of a magnetic-gear outer-rotor permanent-magnet brushless motor for electric vehicles," *IEEE Trans. Magn.*, vol. 43, no. 6, pp. 2504-2506, 2007.
- [A15] L. Jian, K. T. Chau, and J. Z. Jiang, "An integrated magnetic-gear permanent magnet in-wheel motor drive for electric vehicles," *2008 IEEE Vehicle Power and Propulsion Conf.*, 3-5 Sept. 2008.
- [A16] K. Atallah, J. Rens, S. Mezani, and D. Howe, "A novel "pseudo" direct-drive brushless permanent magnet machine," *IEEE Trans. Magn.*, vol. 44, no. 11, pp. 4349-4352, 2008.
- [A17] L. L. Wang, J. X. Shen, Y. Wang, and K. Wang, "A novel magnetic-gear outer-rotor permanent magnet brushless motor," *4th IET Conf. Power Electronics, Machines and Drives*, pp. 33 -36, 2008.
- [A18] L. Jian, G. Xu, C. C. Mi, K. T. Chau, and C. C. Chan, "Analytical Method for Magnetic Field Calculation in a Low-Speed Permanent-Magnet Harmonic Machine," *IEEE Trans. Energy Convers.*, vol. 26, no. 3, pp. 862-870, 2011.

- [A19] W. N. Fu and S. L. Ho, "A quantitative comparative analysis of a novel flux-modulated permanent-magnet motor for low-speed drive," *IEEE Trans. Magn.*, vol. 46, no. 1, pp. 127-134, 2010.
- [A20] C. H. Lee, "Vernier motor and its design," *IEEE Trans. Power App. Syst.*, vol. 82, no. 66, pp. 343-349, 1963.
- [A21] A. Toba and T. A. Lipo, "Generic torque-maximizing design methodology of surface permanent-magnet Vernier machine," *IEEE Trans. Ind. Appl.*, vol. 36, no. 6, pp. 1539-1546, 2000.
- [A22] A. Toba and T. A. Lipo, "Novel dual-excitation permanent magnet Vernier machine," *1999 34th IAS Annual Meeting on Conf. Record of the Ind. Appl. Conf.*, vol. 4, pp. 2539-2544, 3-7 Oct. 1999.
- [A23] C. Liu, "Design of a new outer-rotor flux-controllable Vernier PM in-wheel motor drive for electric vehicle," in *2011 Int. Conf. Electr. Mach. Syst.*, 20-23 Aug. 2011, Beijing, China.
- [A24] J. Li, K. T. Chau, J. Z. Jiang, C. Liu, and W. Li, "A new efficient permanent-magnet Vernier machine for wind power generation," *IEEE Trans. Magn.*, vol. 46, no. 6, pp. 1475-1478, 2010.
- [A25] D. Li, R. Qu, and T. A. Lipo, "High-power-factor Vernier permanent-magnet machines," *IEEE Trans. Ind. Appl.*, vol. 50, no. 6, pp. 3664-3674, 2014.
- [A26] Y. Liao, L. Xu, and L. Zhen, "Design of a doubly fed reluctance motor for adjustable-speed drives," *IEEE Trans. Ind. Appl.*, vol. 32, no. 5, pp. 1195-1203, 1996.
- [A27] D. G. Dorrell, A. M. Knight, and R. E. Betz, "Improvements in brushless doubly fed reluctance generators using high-flux-density steels and selection of the correct pole numbers," *IEEE Trans. Magn.*, vol. 47, no. 10, pp. 4092-4095, 2011.
- [A28] M.-F. Hsieh, I. H. Lin, and D. Dorrell, "Magnetic circuit modeling of brushless doubly-fed machines with induction and reluctance rotors," *IEEE Trans. Magn.*, vol. 49, no. 5, pp. 2359-2362, 2013.
- [A29] S. Williamson, A. C. Ferreira, and A. K. Wallace, "Generalised theory of the brushless doubly-fed machine. I. Analysis," *IEE Proc.: Electric Power Appl.*, vol. 144, no. 2, pp. 111-122, 5-9 Oct. 1997.
- [A30] M. S. Boger, A. K. Wallace, and R. Spee, "Investigation of appropriate pole number combinations for brushless doubly fed machines applied to pump drives," *IEEE Trans. Ind. Appl.*, vol. 32, no. 1, pp. 189-194, 1996.
- [A31] Y. Wang, S. L. Ho, W. N. Fu, and J. X. Shen, "A novel brushless doubly fed generator for wind power generation," *IEEE Trans. Magn.*, vol. 48, no. 11, pp. 4172-4175, 2012.
- [A32] L. Xu, Y. Liu, and X. Wen, "Comparison study of singly-fed electric machine with doubly-fed machine for EV/HEV applications," *2011 Int. Conf. Electrical Machines and Systems*, 20-23 Aug. 2011.

- [A33] L. Xu, B. Guan, H. Liu, L. Gao, and K. Tsai, "Design and control of a high-efficiency Doubly-Fed Brushless machine for wind power generator application," *2010 IEEE Energy Conversion Congress and Exposition (ECCE)*, pp. 2409-2416, 12-16 Sept. 2010.
- [A34] L. Xu and F. Wang, "Comparative study of magnetic coupling for a doubly fed brushless machine with reluctance and cage rotors," *1997 32nd IAS Annual Meeting on Conf. Record of the Ind. Appl. Conf.*, vol. 1, pp. 326-332, 5-9 Oct. 1997.
- [A35] G. J. Li *et al.*, "Excitation winding short-circuits in hybrid excitation permanent magnet motor," *IEEE Trans. Energy Convers.*, vol. 29, no. 3, pp. 567-575, 2014.
- [A36] A. S. Thomas, Z. Q. Zhu, and L. J. Wu, "Novel modular-rotor switched-flux permanent magnet machines," *IEEE Trans. Ind. Appl.*, vol. 48, no. 6, pp. 2249-2258, 2012.
- [A37] Z. Q. Zhu and J. T. Chen, "Advanced flux-switching permanent magnet brushless machines," *IEEE Trans. Magn.*, vol. 46, no. 6, pp. 1447-1453, 2010.
- [A38] M. Cheng, W. Hua, J. Zhang, and W. Zhao, "Overview of stator-permanent magnet brushless machines," *IEEE Trans. Ind. Electron.*, vol. 58, no. 11, pp. 5087-5101, 2011.
- [A39] Y. Wang, Z. W. Huang, J. X. Shen, and C. F. Wang, "Comparison and study of 6/5- and 12/10-pole permanent magnet flux-switching motors considering flux-weakening capability," *2008 Int. Conf. Electrical Mach. Syst.*, pp. 3262-3265, 17-20 Oct. 2008.
- [A40] R. Cao, C. Mi, and M. Cheng, "Quantitative comparison of flux-switching permanent-magnet motors with interior permanent magnet motor for EV, HEV, and PHEV applications," *IEEE Trans. Magn.*, vol. 48, no. 8, pp. 2374-2384, 2012.
- [A41] R. Hosoya and S. Shimomura, "Apply to in-wheel machine of permanent magnet Vernier machine using NdFeB bonded magnet — Fundamental study," *8th Int'l Conf. Power Electronics - ECCE Asia*, pp. 2208-2215, 30 May - 3 June 2011.
- [A42] Y. Tasaki, R. Hosoya, Y. Kashitani, and S. Shimomura, "Design of the Vernier machine with permanent magnets on both stator and rotor side," *Proc.: The 7th Int. Power Electron. and Motion Control Conf.*, vol. 1, pp. 302-309, 2-5 June 2012.
- [A43] L. Jian, Y. Shi, C. Liu, G. Xu, Y. Gong, and C. C. Chan, "A novel dual-permanent-magnet-excited machine for low-speed large-torque applications," *IEEE Trans. Magn.*, vol. 49, no. 5, pp. 2381-2384, 2013.
- [A44] W. N. Fu, Y. Chen, and X. Guo, "Novel dual-layer and triple-layer permanent-magnet-excited

- synchronous motors," *IEEE Trans. Magn.*, vol. 51, no. 11, p. 8108404, 2015.
- [A45] C. Yu, S. Niu, S. L. Ho, and W. N. Fu, "Design and analysis of a magnetless double-rotor flux switching motor for low cost application," *IEEE Trans. Magn.*, vol. 50, no. 11, p. 8105104, 2014.
- [A46] Y. Liu, S. L. Ho, and W. N. Fu, "Novel electrical continuously variable transmission system and its numerical model," *IEEE Trans. Magn.*, vol. 50, no. 2, pp. 757-760, 2014.
- [A47] S. Niu, S. L. Ho, and W. N. Fu, "A novel direct-drive dual-structure permanent magnet machine," *IEEE Trans. Magn.*, vol. 46, no. 6, pp. 2036-2039, 2010.
- [A48] S. Niu, S. L. Ho, and W. N. Fu, "Design of a novel electrical continuously variable transmission system based on harmonic spectra analysis of magnetic field," *IEEE Trans. Magn.*, vol. 49, no. 5, pp. 2161-2164, 2013.
- [A49] S. Niu, S. L. Ho, and W. N. Fu, "A novel double-stator double-rotor brushless electrical continuously variable transmission system," *IEEE Trans. Magn.*, vol. 49, no. 7, pp. 3909-3912, 2013.

Chapter 2 Unified theory of flux-modulated machines

2.1 Introduction

In this chapter, the internal relationships and operating mechanisms of the basic flux-modulated motor, Vernier motor, doubly-fed reluctance machine, flux-switching motor, and dual-PM-excited motor will be scrutinized and all these machines will be summarized as general flux-modulated machines (GFMMs), as they all employ non-uniform magnetic reluctance to modulate their magnetic flux to produce constant torque.

A general theory to explain the operating principle of all these machines will be proposed. Unified design guidelines of these machines, which can quickly identify the efficacy of different combinations of pole-pairs of the windings, permanent magnets (PMs), special ferromagnetic segments and teeth/slots, as well as ac/dc excitations and the rotating speeds of the rotors, will be developed. A novel general pattern of PM arrangement will be presented. By optimizing its sizes, the best PM arrangement can be automatically determined. Based on the developed general theory, a computer program which can search possible topologies with single/double stators, single/double rotors, the combinations of pole-pairs and the magnetic field rotating speeds of different parts, the frequencies in different windings, will be developed. All candidates will be quantitatively investigated using transient magnetic

field, power electronic circuit, mechanical motion and thermal field coupled finite-element method (FEM). Based on the developed computer program, the best/novel topologies of EMs for specific applications can be automatically determined.

2.2 Unified theory of flux-modulated machines

A concept of general flux-modulated machines is presented. A basic flux-modulated motor, or a flux-switching motor, or a Vernier motor, or a dual-PM-excited motor can be considered as a special structure of the general flux-modulated machines. The operating principle of the general flux-modulated machines can be derived from a magnetic gear (MG) with the structure as shown in Fig. 2.1. The MG has three parts. The outer part is referred as Part 1 which has PMs with p_1 pole pairs, and the inner part is referred as Part 2 which has PMs with p_2 pole pairs. The middle part has ferromagnetic segments with pole pairs of p_{Fe} .

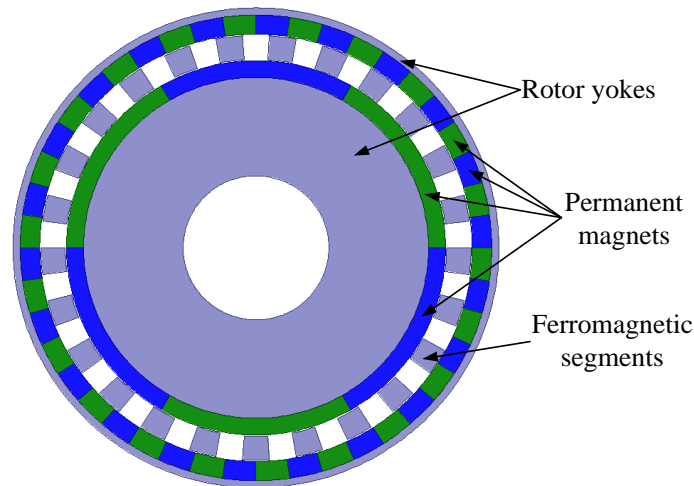


Fig. 2.1. A magnetic gear.

Since the relationship between the magnetomotive force (mmf) F and the magnetic flux density B in airgap can be expressed as:

$$F = \delta H = \frac{\delta}{\mu_0} B, \quad (2.1)$$

the magnetic flux density in the airgap is:

$$B = \frac{\mu_0}{\delta} F = \lambda F, \quad (2.2)$$

where the permeance per length of the airgap can be simply expressed as $\lambda = \mu_0 / \delta$. Here δ is the airgap length and μ_0 is the permeability of air.

The mmf produced by the PMs on Part 1 which rotates at the speed of ω_1 with the pole pairs of p_1 can be expressed as

$$F_1 = F_{1m} \cos(p_1\theta - d_1 p_1 \omega_1 t + \phi_1), \quad (2.3)$$

where F_{1m} is the magnitude of mmf; θ is the mechanical angular position; $d_1=1$ indicates the mmf rotating in positive direction and $d_1=-1$ indicates the mmf rotating in negative direction; ϕ_1 is the initial phase angle; ω_1 is the mechanical angular speed.

Similarly, the mmf produced by PMs on Part 2 in air gap of Part 1 which rotates at the speed of ω_2 with the pole pairs of p_2 can be expressed as

$$F_2 = F_{2m} \cos(p_2\theta - d_2 p_2 \omega_2 t + \phi_2), \quad (2.4)$$

where F_{2m} is the magnitude of mmf; θ is the mechanical angular position; $d_2=1$ indicates the mmf rotating in positive direction and $d_2=-1$ indicates the mmf rotating in negative direction; ϕ_2 is the initial phase angle; ω_2 is the mechanical angular speed.

The permeance per length of the airgap is a periodic function of space angle θ and its average value and fundamental component can be obtained using Fourier decomposition. Supposing

the ferromagnetic segments rotate at the speed of ω_{Fe} with the pole pairs of p_{Fe} , the average and fundamental components of the permeance can be expressed as:

$$\lambda = \lambda_{av} + \lambda_m \cos(p_{Fe}\theta - p_{Fe}\omega_{Fe}t + \phi_{Fe}). \quad (2.5)$$

From (2.2) and (2.3), and using mathematical identity:

$$\cos(x)\cos(y) = (1/2)[\cos(x-y) + \cos(x+y)],$$

the magnetic flux density produced by Part 1 in the air gap of Part 2 is:

$$\begin{aligned} B_1 &= \lambda F_1 \\ &= [\lambda_{av} + \lambda_m \cos(p_{Fe}\theta - p_{Fe}\omega_{Fe}t + \phi_{Fe})] F_{1m} \cos(p_1\theta - d_1 p_1 \omega_1 t + \phi_1) \\ &= \lambda_{av} F_{1m} \cos(p_1\theta - d_1 p_1 \omega_1 t + \phi_1) \\ &\quad + \lambda_m F_{1m} \cos(p_{Fe}\theta - p_{Fe}\omega_{Fe}t + \phi_{Fe}) \cos(p_1\theta - d_1 p_1 \omega_1 t + \phi_1) \\ &= \lambda_{av} F_{1m} \cos(p_1\theta - d_1 p_1 \omega_1 t + \phi_1) \\ &\quad + (1/2)\lambda_m F_{1m} \cos[(p_{Fe} - p_1)\theta - (p_{Fe}\omega_{Fe} - d_1 p_1 \omega_1)t + (\phi_{Fe} - \phi_1)] \\ &\quad + (1/2)\lambda_m F_{1m} \cos[(p_{Fe} + p_1)\theta - (p_{Fe}\omega_{Fe} + d_1 p_1 \omega_1)t + (\phi_{Fe} + \phi_1)] \\ &= B_{11} + B_{12} + B_{13}, \end{aligned} \quad (2.6)$$

where

$$B_{11} = \lambda_{av} F_{1m} \cos(p_1\theta - d_1 p_1 \omega_1 t + \phi_1), \quad (2.7)$$

$$B_{12} = (1/2)\lambda_m F_{1m} \cos[(p_{Fe} - p_1)\theta - (p_{Fe}\omega_{Fe} - d_1 p_1 \omega_1)t + (\phi_{Fe} - \phi_1)], \quad (2.8)$$

$$B_{13} = (1/2)\lambda_m F_{1m} \cos[(p_{Fe} + p_1)\theta - (p_{Fe}\omega_{Fe} + d_1 p_1 \omega_1)t + (\phi_{Fe} + \phi_1)]. \quad (2.9)$$

Similarly, the magnetic flux density produced by Part 2 in the air gap of Part 1 is:

$$B_2 = B_{21} + B_{22} + B_{23}, \quad (2.10)$$

where

$$B_{21} = \lambda_{av} F_{2m} \cos(p_2 \theta - d_2 p_2 \omega_2 t + \phi_2), \quad (2.11)$$

$$B_{22} = (1/2) \lambda_m F_{2m} \cos[(p_{Fe} - p_2) \theta - (p_{Fe} \omega_{Fe} - d_2 p_2 \omega_2) t + (\phi_{Fe} - \phi_2)], \quad (2.12)$$

$$B_{23} = (1/2) \lambda_m F_{2m} \cos[(p_{Fe} + p_2) \theta - (p_{Fe} \omega_{Fe} + d_2 p_2 \omega_2) t + (\phi_{Fe} + \phi_2)] \quad (2.13)$$

According to the expressions of B_{12} and B_{13} , the component B_{12} 's speed is:

$$\omega_{B12} = \frac{p_{Fe} \omega_{Fe} - d_1 p_1 \omega_1}{p_{Fe} - p_1} = \frac{p_{Fe} \omega_{Fe} - d_1 p_1 \frac{2\pi f_1}{p_1}}{p_{Fe} - p_1} = \frac{p_{Fe} \omega_{Fe} - d_1 2\pi f_1}{p_{Fe} - p_1}, \quad (2.14)$$

and the component B_{13} 's speed is:

$$\omega_{B13} = \frac{p_{Fe} \omega_{Fe} + d_1 p_1 \omega_1}{p_{Fe} + p_1} = \frac{p_{Fe} \omega_{Fe} + d_1 p_1 \frac{2\pi f_1}{p_1}}{p_{Fe} + p_1} = \frac{p_{Fe} \omega_{Fe} + d_1 2\pi f_1}{p_{Fe} + p_1}. \quad (2.15)$$

Similarly, according to the expressions of B_{22} and B_{23} , the component B_{22} 's speed is:

$$\omega_{B22} = \frac{p_{Fe} \omega_{Fe} - d_2 p_2 \omega_2}{p_{Fe} - p_2} = \frac{p_{Fe} \omega_{Fe} - d_2 p_2 \frac{2\pi f_2}{p_2}}{p_{Fe} - p_2} = \frac{p_{Fe} \omega_{Fe} - d_2 2\pi f_2}{p_{Fe} - p_2}, \quad (2.16)$$

and the component B_{23} 's speed is:

$$\omega_{B23} = \frac{p_{Fe} \omega_{Fe} + d_2 p_2 \omega_2}{p_{Fe} + p_2} = \frac{p_{Fe} \omega_{Fe} + d_2 p_2 \frac{2\pi f_2}{p_2}}{p_{Fe} + p_2} = \frac{p_{Fe} \omega_{Fe} + d_2 2\pi f_2}{p_{Fe} + p_2}. \quad (2.17)$$

Based on above general formulations, following situations are studied:

(1) Considering the components B_{11} and B_{22} , choosing $d_1=+1$, $d_2=\pm 1$, $\omega_1 = \omega_{B22}$,

$p_{Fe} = p_1 + p_2$, one has

$$\omega_{B22} = \frac{p_{Fe} \omega_{Fe} \mp 2\pi f_2}{p_{Fe} - p_2} = \omega_1 = \frac{2\pi f_1}{p_1}.$$

Therefore,

$$p_{\text{Fe}} \omega_{\text{Fe}} = 2\pi f_1 \pm 2\pi f_2, \quad (2.18)$$

and the speed of ferromagnetic segments can be expressed as

$$\omega_{\text{Fe}} = \frac{2\pi(f_1 \pm f_2)}{p_{\text{Fe}}},$$

that is

$$n_{\text{Fe}} = \frac{60\omega_{\text{Fe}}}{2\pi} = \frac{60(f_1 \pm f_2)}{p_{\text{Fe}}}. \quad (2.19)$$

(2) Considering the components B_{21} and B_{12} , choosing $d_1=+1$, $d_2=\pm 1$, $d_2\omega_2 = \omega_{B_{12}}$,

$p_{\text{Fe}} = p_1 + p_2$, one has

$$\omega_{B_{12}} = \frac{p_{\text{Fe}}\omega_{\text{Fe}} - 2\pi f_1}{p_{\text{Fe}} - p_1} = \pm\omega_2 = \pm \frac{2\pi f_2}{p_2}.$$

Therefore,

$$p_{\text{Fe}} \omega_{\text{Fe}} = 2\pi f_1 \pm 2\pi f_2,$$

and the speed of ferromagnetic segments also can be expressed as

$$\omega_{\text{Fe}} = \frac{2\pi(f_1 \pm f_2)}{p_{\text{Fe}}},$$

and

$$n_{\text{Fe}} = \frac{60\omega_{\text{Fe}}}{2\pi} = \frac{60(f_1 \pm f_2)}{p_{\text{Fe}}}.$$

(3) Considering the components B_{11} and B_{23} , choosing $d_1=+1$, $d_2=\pm 1$, $\omega_1 = \omega_{B_{23}}$,

$p_{\text{Fe}} = p_1 - p_2$, one has

$$\omega_{B_{23}} = \frac{p_{\text{Fe}}\omega_{\text{Fe}} \pm 2\pi f_2}{p_{\text{Fe}} + p_2} = \omega_1 = \frac{2\pi f_1}{p_1}.$$

Therefore,

$$p_{\text{Fe}} \omega_{\text{Fe}} = 2\pi f_1 \pm 2\pi f_2,$$

and the expression of the speed of ferromagnetic segments can be obtained:

$$n_{\text{Fe}} = \frac{60 \omega_{\text{Fe}}}{2\pi} = \frac{60(f_1 \pm f_2)}{p_{\text{Fe}}}.$$

(4) Considering the components B_{21} and B_{13} , choosing $d_1=-1$, $d_2=\pm 1$, $d_2 \omega_2 = \omega_{B13}$,

$p_{\text{Fe}} = p_2 - p_1$, one has

$$\omega_{B13} = \frac{p_{\text{Fe}} \omega_{\text{Fe}} - 2\pi f_1}{p_{\text{Fe}} + p_1} = \pm \omega_2 = \pm \frac{2\pi f_2}{p_2}.$$

Therefore,

$$p_{\text{Fe}} \omega_{\text{Fe}} = 2\pi f_1 \pm 2\pi f_2,$$

and the expression of the speed of ferromagnetic segments can also be obtained:

$$n_{\text{Fe}} = \frac{60 \omega_{\text{Fe}}}{2\pi} = \frac{60(f_1 \pm f_2)}{p_{\text{Fe}}}.$$

Therefore, to satisfy the mechanism of producing constant electromagnetic torque, the pole pairs of the outer part and the inner part and the number of ferromagnetic segments should meet the following relationship:

$$p_{\text{Fe}} = p_1 \pm p_2, \quad (2.20)$$

or

$$p_{\text{Fe}} = p_2 - p_1. \quad (2.21)$$

The rotational speeds of the outer part, middle part and inner part are ω_1 , ω_{Fe} , and ω_2 , respectively. Their basic relationship is:

$$p_{\text{Fe}} \omega_{\text{Fe}} = p_1 \omega_1 \pm p_2 \omega_2, \quad (2.22)$$

or

$$p_{Fe} \omega_{Fe} = p_2 \omega_2 - p_1 \omega_1. \quad (2.23)$$

For the example shown in Fig. 2.1, $p_1 = 22$, $p_{Fe} = 25$, $p_2 = p_{Fe} - p_1 = 25 - 22 = 3$. If the part of ferromagnetic segments is stationary, the gear ratio $\omega_2/\omega_1 = -p_1/p_2 = -22/3$.

When the part with PMs rotates, it will produce a rotating magnetic field. It is well-known that a three-phase winding system with symmetrical currents can also produce a rotating magnetic field. Therefore, if the parts with PMs are replaced by stationary three-phase windings, different types of electric machines can be produced.

2.2.1 Basic flux-modulated motor

If the inner part in Fig. 2.1 is replaced by a three-phase winding, a basic flux-modulated motor is produced [B1]. In the example shown in Fig. 2.2, the inner part is a stator. $p_{rotor} = 22$, $p_{Fe} = 25$, $p_{winding} = p_{Fe} - p_{rotor} = 25 - 22 = 3$. The stator winding has 3 pole pairs, but the outer rotor will rotate at a low speed. The motor is suitable for low-speed direct drive.

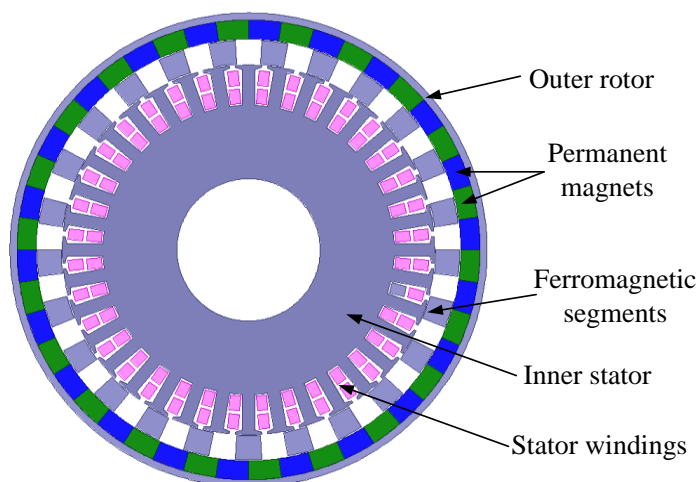


Fig. 2.2. A basic radial flux-modulated motor.

2.2.2 Flux-switching motor

In the basic magnetic gear, as shown in Fig. 2.1, if the rotating magnetic field of the outer part with the speed $\omega_1=2\pi f_1/p_1$ is produced by a set of stationary three-phase windings with pole pairs p_1 and frequency f_1 , the PMs on the inner part are stationary and combined with the outer part, the ferromagnetic segments rotate with the speed ω_{Fe} , the machine is a flux-switching motor [B2]. According to Eq. 2.22, the speed of the rotor is $\omega_{Fe} = (p_1\omega_1 \pm p_2\omega_2) / p_{Fe} = 2\pi f_1/p_{Fe}$. A typical flux-switching motor with flux-focusing PMs is shown in Fig. 2.3.

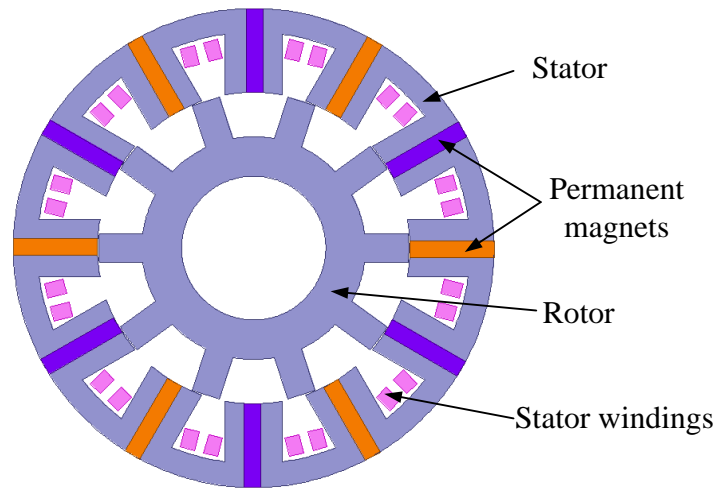


Fig. 2.3. A flux-switching motor.

2.2.3 Vernier motor

In the basic flux-modulated motor, if the stationary ferromagnetic segments are combined with the stator together, it is a Vernier motor [B3]. The Vernier motor can also adopt an open-slot structure to modulate the magnetic field in the airgap. The Vernier motor can be considered as a special situation of the basic flux-modulated motor when the number of stator slots and the number of ferromagnetic segments are the same. Compared with the basic flux-modulated motor, it has a simple structure at the expense of losing the flexible choice of the number of ferromagnetic segments. A typical Vernier motor with surface-mounted

PMs is shown in Fig. 2.4.

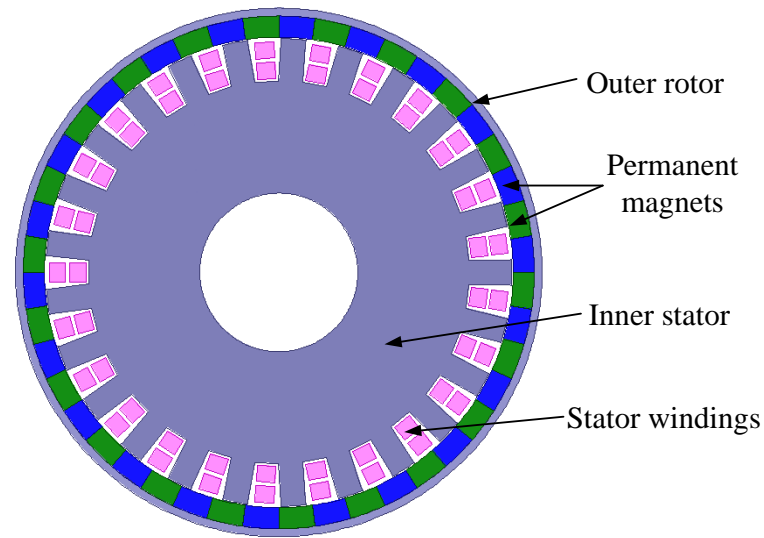


Fig. 2.4. A Vernier motor.

2.2.4 Dual-PM-excited motor

A dual-PM-excited motor, as shown in Fig. 2.5, can be derived from the combination of a flux-switching motor and a Vernier motor [B4]. In the Vernier motor, if additional PMs with consequent poles are inserted inside the slots of the open-slot stator and consequent-pole arrangement of PMs is also employed to the rotor, it is a dual-PM-excited motor. The additional PMs produce an extra set of magnetic field which is modulated by the magnetic reluctance of the rotor and reacts with the magnetic field produced by the stator windings to produce additional transmitted torque. That is, the stator windings and the PMs on the stator and the salient rotor constitute a flux-switching motor; the stator windings and the tooth-slot effect of the stator and the PMs on the rotor constitute a Vernier motor.

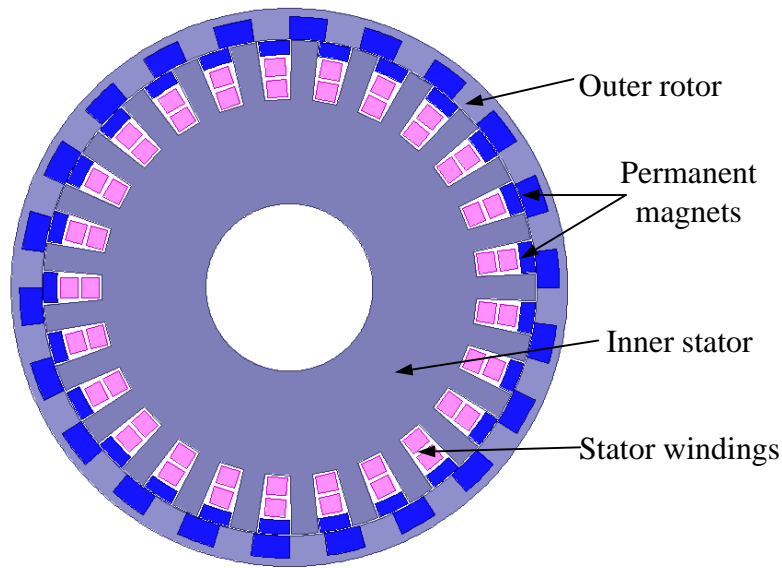


Fig. 2.5. A dual-PM-excited motor.

Based on the above discussions, all topologies of basic flux-modulated motor, Vernier motor, flux-switching motor, and dual-PM-excited motor can be considered as special situations of general flux-modulated machines (GFMMs). All these machines can be derived from the MG. Therefore, a general and unified model of GFMMs can be established, with the following possible topologies: (1) Each part can be stationary or rotary. (2) Each part can have one or two sets of windings with ac/dc power connections. The slots can be split-pole, open-slot structure with variable airgap permeance for flux modulation. (3) The PMs can be arranged in different ways: surface mounted PM, spoke-type PM, V-type PM, and consequent PM poles which have the function of flux modulation. The PMs can also be located at different places. (4) The machine may have single/double stator, single/double rotor. The single rotor can be arranged in two separate parts to produce a two-airgap structure [B5]. (5) A GFMM and a conventional PM machine or a MG may be integrated together [B6].

2.3 Conclusion

This chapter introduces a concept of general flux-modulated electric machines (GFMMs), which is based on a proposed unified theory for such types of machines. It can explain the operating principles of a basic flux-modulated motor, a flux-switching motor, a Vernier motor, and a dual-PM-excited motor with PMs on both rotor and stator. Unified design guidelines of these machines can be applied to the innovation of machine topologies.

Reference Part B

- [B1] J. Li, K. T. Chau, J. Z. Jiang, C. Liu, and W. Li, "A new efficient permanent magnet vernier machine for wind power generation," *IEEE Trans. Magn.*, vol. 46, no. 6, pp. 1475-1478, Jun. 2010.
- [B2] M. Cheng, W. Hua, J. Zhang, and W. Zhao, "Overview of stator-permanent-magnet brushless machines," *IEEE Trans. Ind. Electron.*, vol. 85, no. 11, pp. 5087-5101, Nov. 2011.
- [B3] L. Xu, G. Liu, W. Zhao, and X. Yang, "Hybrid stator design of fault-tolerant permanent-magnet vernier machines for direct-drive applications," *IEEE Trans. Ind. Electron.*, vol. 64, no. 1, pp. 179-190, Jan. 2017.
- [B4] L. Jian, Y. Shi, C. Liu, G. Xu, Y. Gong, and C. C. Chan, "A novel dual permanent-magnet-excited machine for low-speed large-torque applications," *IEEE Trans. Magn.*, vol. 49, no. 5, pp. 2381-2384, May 2013.
- [B5] C. Yu, S. X. Niu, S. L. Ho, and W. N. Fu, "Design and analysis of a magnetless double-rotor flux switching motor for low cost application," *IEEE Trans. Magn.*, vol. 50, no. 11, 2014.
- [B6] K. T. Chau, Z. Dong, J. Z. Jiang, L. Chunhua, and Z. Yuejin, "Design of a magnetic-g geared outer-rotor permanent-magnet brushless motor for electric vehicles," *IEEE Trans. Magn.*, vol. 43, no. 6, pp. 2504-2506, Jun. 2007.

Chapter 3 Analysis of a doubly-fed dual-stator flux-modulated motor

3.1 Introduction

In recent years several different kinds of novel electric machines emerged, including a basic flux-modulated motor [C1-C3], a Vernier permanent-magnet (PM) motor [C4-C7], a flux-switching motor [C8-C11], a doubly-fed magnetic reluctance machine [C12-C16], a dual-excited PM machine [C7, C17], and a magnetic-gear machine [C18]. They can be driven by a voltage source or a power electronic converter. These machines have special features which differ them from conventional synchronous machines. Their pole-pair number of the stator can be different from that of the rotor, which breaks the basic rule that the number of pole pairs of the stator and the rotor should be the same for the design of conventional electric machines.

In the previous chapter, a concept of general flux-modulated electric machines is introduced, which is based on a proposed unified theory for such types of machines. It can explain the operating principles of a basic flux-modulated motor, a flux-switching motor, a Vernier motor, and a dual-PM-excited motor with PMs on both rotor and stator.

In this chapter, based on the proposed theory, a novel doubly-fed dual-stator (DFDS) motor is presented. Finite-element method (FEM) of magnetic field with mechanical motion coupled computation is employed to evaluate the performances of the machine. Its design

method using an optimization algorithm is also presented. Experiment results of a prototype are presented to showcase the performance of the proposed DFDS motor.

3.2 The operating theory of the proposed DFDS motor

Based on the unified theory proposed in the last chapter, if both the inner part and outer part of the radial-flux magnetic gear are replaced by three-phase windings, a novel DFDS motor is produced [C19]. The DFDS motor has three parts. The outer part is referred as Outer Stator with a three-phase winding of p_{outer} pole pairs, and the inner part is referred as Inner Stator with a three-phase winding of p_{inner} pole pairs. The middle part is the rotor with ferromagnetic segments of p_{Fe} pole pairs. In the design shown in Fig. 3.1, $p_{\text{outer}} = 22$, $p_{\text{Fe}} = 25$, $p_{\text{inner}} = p_{\text{Fe}} - p_{\text{outer}} = 3$ (the phase sequence is opposite to that of the outer winding).

In the proposed DFDS motor, to produce constant electromagnetic torque, the number of pole pairs of the inner winding p_{inner} , the number of pole pairs of the outer winding p_{outer} and the number of ferromagnetic segments p_{Fe} should meet the relationship:

$$p_{\text{Fe}} = p_{\text{inner}} \pm p_{\text{outer}} . \tag{3.1}$$

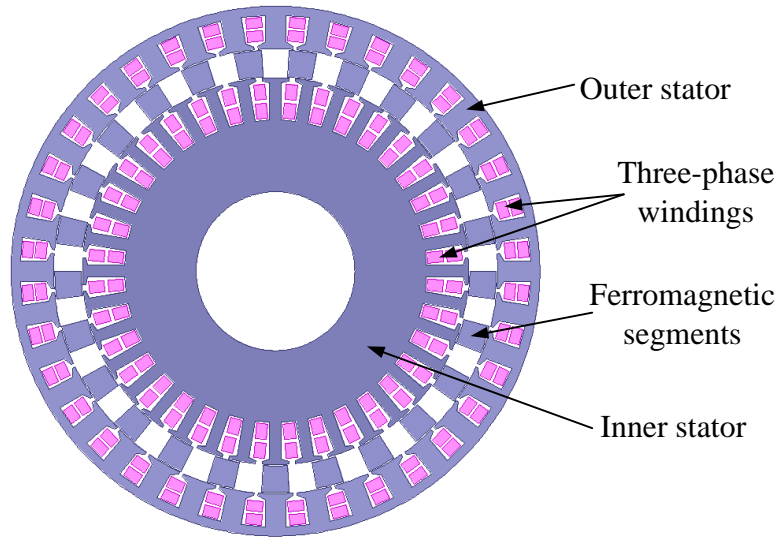


Fig. 3.1. The presented doubly-fed dual-stator (DFDS) motor.

The rotational velocity of the fundamental component of the magnetic field produced by the inner winding is:

$$\omega_{\text{inner}} = \frac{2\pi}{p_{\text{inner}}} f_{\text{inner}} ,$$

where f_{inner} is the frequency of the inner winding.

The rotational velocity of the fundamental component of the magnetic field produced by the outer winding (the phase sequence is opposite of the inner winding) is:

$$\omega_{\text{outer}} = -\frac{2\pi}{p_{\text{outer}}} f_{\text{outer}} ,$$

where f_{outer} is the frequency of the outer winding. The rotational velocity of the ferromagnetic segments is ω_{Fe} . In the proposed DFDS motor, the relationship of the rotational velocities of different parts can be expressed as

$$p_{\text{Fe}} \omega_{\text{Fe}} = p_{\text{inner}} \omega_{\text{inner}} + p_{\text{outer}} \omega_{\text{outer}} . \quad (3.2)$$

One designs: $p_{\text{outer}} = p_{\text{Fe}} - p_{\text{inner}}$, then we have

$$\omega_{\text{outer}} = -\frac{2\pi}{p_{\text{outer}}} f_{\text{outer}} = \frac{2\pi}{p_{\text{inner}} - p_{\text{Fe}}} f_{\text{outer}},$$

and one can obtain

$$\omega_{\text{Fe}} = \frac{2\pi(f_{\text{inner}} - f_{\text{outer}})}{p_{\text{Fe}}},$$

and

$$n_{\text{Fe}} = \frac{60(f_{\text{inner}} - f_{\text{outer}})}{p_{\text{Fe}}}. \quad (3.3)$$

In the example shown in Fig. 3.1, one designs

$$n_{\text{Fe}} = \frac{60(f_{\text{inner}} - f_{\text{outer}})}{p_{\text{Fe}}} = \frac{60 \times (100 - 95)}{25} = 12 \text{ (r/min)}.$$

So, in this example f_{inner} is 100 Hz and f_{outer} is 95 Hz. The rotating speed of the ferromagnetic segments is 12 r/min.

If the phase sequence of the outer winding is the same as the inner winding,

$$\omega_{\text{outer}} = \frac{2\pi}{p_{\text{outer}}} f_{\text{outer}} = \frac{2\pi}{p_{\text{Fe}} - p_{\text{inner}}} f_{\text{outer}},$$

then one can obtain

$$\omega_{\text{Fe}} = \frac{2\pi(f_{\text{inner}} + f_{\text{outer}})}{p_{\text{Fe}}},$$

and

$$n_{\text{Fe}} = \frac{60(f_{\text{inner}} + f_{\text{outer}})}{p_{\text{Fe}}} \quad (3.4)$$

In the example shown in Fig. 3.1, one designs

$$n_{Fe} = \frac{60(f_{inner} + f_{outer})}{p_{Fe}} = \frac{60 \times (100 + 95)}{25} = 468 \text{ (r/min)} .$$

In this example f_{inner} is 100 Hz and f_{outer} is 95 Hz. The rotating speed of the ferromagnetic segments can reach 468 r/min. It is beneficial to the control of the motor in low speed period and reduce the losses of the motor in high speed period, as relatively low frequency is required. For a conventional motor with a single excited winding the frequency is required changing from 5Hz to 195Hz. This shows that the proposed DFDS motor has wide speed range which is suitable for electrical vehicle direct-drive application.

3.3 Optimization of the proposed DFDS motor

The numerical method of finite-element method (FEM) [C20] presents the advantage of taking into account the real geometry of the motor as well as the magnetic saturation of the ferromagnetic parts, control circuit and high-order harmonics. Therefore, FEM is used for the performance analysis of the proposed DFDS motor.

The properties that are taken into account include the electromagnetic torque, torque ripple, torque per volume, core loss, copper loss regarding windings, input power, output power and corresponding power efficiency. The field and circuit coupled formulation for the modeling of the DFDS motor is

$$\left[\begin{array}{cc} \left(\begin{array}{cc} S_{11} + \frac{T_{11}}{\Delta t} & S_{12} \\ S_{12}^T & \Delta t S_{22} \end{array} \right) & \left(\begin{array}{cc} S_{13} & 0 \\ 0 & 0 \end{array} \right) B_{lb}^T \\ B_{lb} \left(\begin{array}{cc} S_{13}^T & 0 \\ 0 & 0 \end{array} \right) & B_{lb} \left(\begin{array}{cc} \Delta t S_{33} & 0 \\ 0 & -\frac{\Delta t}{lp} R_e \end{array} \right) B_{lb}^T \end{array} \right] \left\{ \begin{array}{l} \left(A^k \right) \\ \left(i_{ad}^k \right) \\ i_l^k \end{array} \right\}$$

$$= \left\{ \begin{array}{l} \left(\begin{array}{c} Q_A + \frac{T_{11}}{\Delta t} A^{k-1} \\ S_{12}^T A^{k-1} \end{array} \right) \\ B_{lb} \left(\begin{array}{c} S_{13}^T A^{k-1} \\ -\frac{\Delta t}{lp} Q_e \end{array} \right) \end{array} \right\}. \quad (3.5)$$

where A is the magnetic vector potential; i_l is the loop current. The details of the above formulation can be found in [C20-C23].

3.3.1 Optimization of the pole-pair/slot combination

To realize fabrication process more easily and reduce the core loss, the number of the ferromagnetic segments is expected to be chosen as small as possible. To compare the performance of different pole-slot combinations, the power load is kept as a constant value when the slot number is changed. The total electric loads in the outer stator and inner stator are also kept the same:

$$Z_{\text{inner}} \times N_{\text{inner}} \times I_{\text{inner}} = C_1,$$

$$Z_{\text{outer}} \times N_{\text{outer}} \times I_{\text{outer}} = C_2,$$

where Z_{inner} and Z_{outer} respectively refer to the slot numbers of the inner stator and the outer stator; N_{inner} and N_{outer} are the conductor numbers in each slot of the inner stator and the outer stator respectively; separately, I_{inner} and I_{outer} are the effective phase current values of the inner stator and the outer stator while the motor model is excited with current source. C_1 and C_2 are constant values. The flow chart of the pole-pair/slot combination optimization is shown in Fig. 3.2.

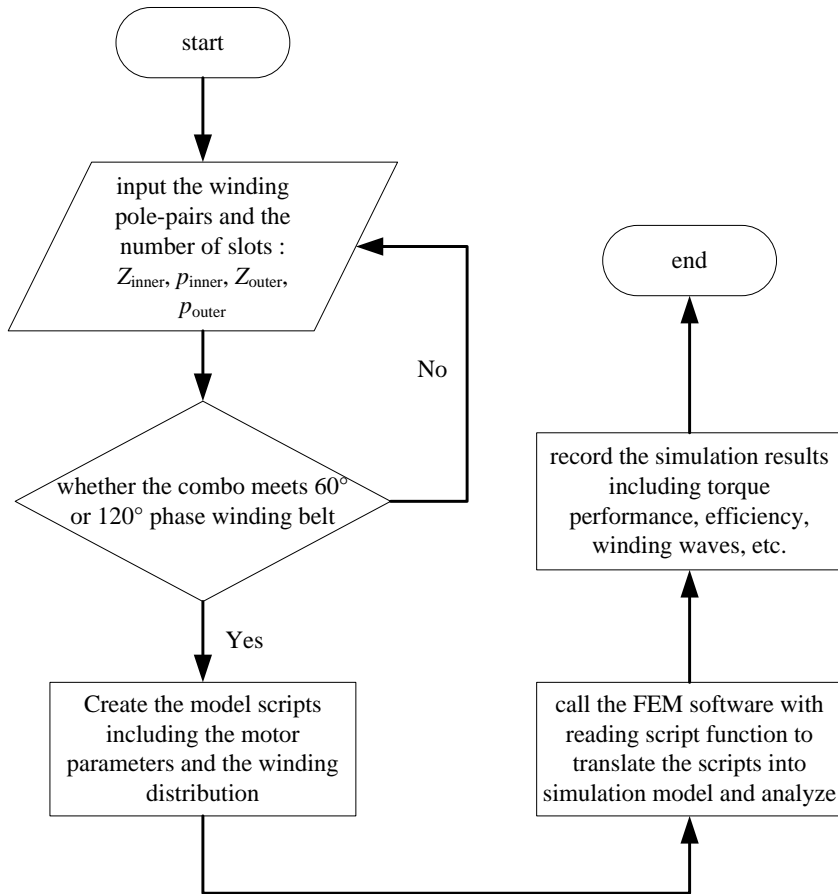


Fig. 3.2. The flow chart of the pole-pair/slot combination optimization.

Finally, an appropriate combination, with 36 slots and 6 pole pairs in the outer stator, as well as 24 slots and 5 pole pairs in the inner stator, is proposed with larger output torque, lower torque ripple and higher efficiency. The number of the ferromagnetic segments is chosen to be 11.

3.3.2 Optimization of parameters

A parameterized model of the proposed DFDS motor is presented to realize the parameter optimization process. The outer diameter and the stack length of the motor are determined by the space available in EV. Beyond that, all other parameters of the motor are optimally designed, such as the sizes of the outer stator and inner stator, the slot sizes and the sizes of

ferromagnetic segments.

An improved tabu search algorithm is employed to find the optimal values of the geometry parameters of the proposed DFDS motor with which an optimal torque performance and an optimal power efficiency value can be obtained. The flow chart of the parameter optimization process is shown in Fig. 3.3.

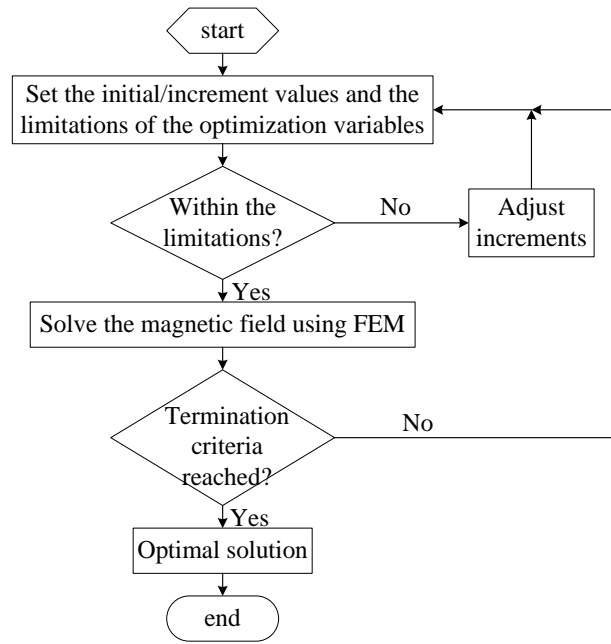


Fig. 3.3. The flow chart of the parameter optimization.

In the improved tabu search algorithm [C24-C25], the intervals of different variable directions are transformed into [0,1]. Then a universal step vector is given by

$$\{H|h_i = h_{i-1} / c_k (i = 1, 2, \dots, r, c_k = 10000^{1/(r-1)}, h_1 = 1)\}. \quad (3.6)$$

Then a feasible random move from the current state in the direction j for the neighbor h_i is given by

$$y_j = x_j + rp_j h_i, \quad (3.7)$$

where r is a random parameter within the interval of $[-1,1]$; $p_j = (b_j - a_j)/2$ ($j = 1, 2, \dots, n$), a_j, b_j are the inferior and superior bounds for the j -th variable.

Two termination criteria are employed to determine whether the global optimal solution has been found. The normal one is that when there are no improvements in the best objective function searched and the number of consecutive moves is larger than a threshold, then the search is terminated. The additional one is that after every cycle of iteration, the search is stopped if

$$|f_k^* - f_{k-p}^*| \leq \varepsilon \quad (p = 1, 2, \dots, n_p), \quad (3.8)$$

$$f_k - f_{opt} \leq \varepsilon, \quad (3.9)$$

where f_k^* is the best solution of the objective function searched in the k -th cycle, and f_{opt} is the best solution of the objective function searched so far.

The Tabu Search Algorithm is a simple but effective technique for optimization. It is sometimes combined with other metaheuristics to create hybrid methods. Since thousands of iterations are generally required in stochastic algorithms, the improved tabu search algorithm has the merit of simplicity in both algorithm structures and numerical implementations which improve the convergence performance and reduce the excessive computation burden. Because of the characteristics of the proposed doubly-fed dual-stator motor, not only the parameters of the motor but also the ratio of the currents applied to the two sets of windings and the corresponding frequencies are taken into consideration in the optimization process.

Smaller current would be applied to the windings in the stator with larger slot area in order to avoid large copper loss in the motor. To prevent from large core loss in the motor, the appropriate frequency combination is employed to the windings because high frequency leads to high core loss. Since the optimization process is implemented coupling with finite element analysis, the consumed time and memory are mainly determined by the scales of FEM mesh. A parallel computing method is also adopted in the optimization process.

The key design data of the proposed DFDS motor are listed in Table 3.1. The design parameters are analyzed systematically and determined after many times of FEM computations.

Table 3.1 Key design data of the proposed DFDS motor

Parameters	Initial value	Final value
Axial stack length	160.0 mm	160.0 mm
Outside radius of the outer stator	155.0 mm	155.0 mm
Air-gap length	0.6 mm	0.6 mm
Inner radius of the outer stator	117 mm	121.4 mm
Inner radius of the inner stator	30.0 mm	30.0 mm
Tooth width in the outer stator	12.0 mm	9.1 mm
Tooth width in the inner stator	12.0 mm	12.1 mm
Slot depth in the outer stator	19.0 mm	20.4 mm
Slot depth in the inner stator	24.0 mm	24.9 mm
Thickness of the ferromagnetic segments	12.0 mm	13.0 mm

3.3.3 Performance analysis

Fig. 3.4 and Fig. 3.5 show the radial flux density in the inner and outer airgaps, respectively. Different orders of harmonics are clearly presented. The fundamental radial flux density in

the inner and outer airgaps are 0.59 T and 0.79 T respectively. The harmonics are much obvious when the pole pairs are 11, 22 and 33 because the number of the modulation segments is 11. The flux line contour and magnetic field distribution of the DFDS motor are shown in Fig. 3.6 and Fig. 3.7, respectively.

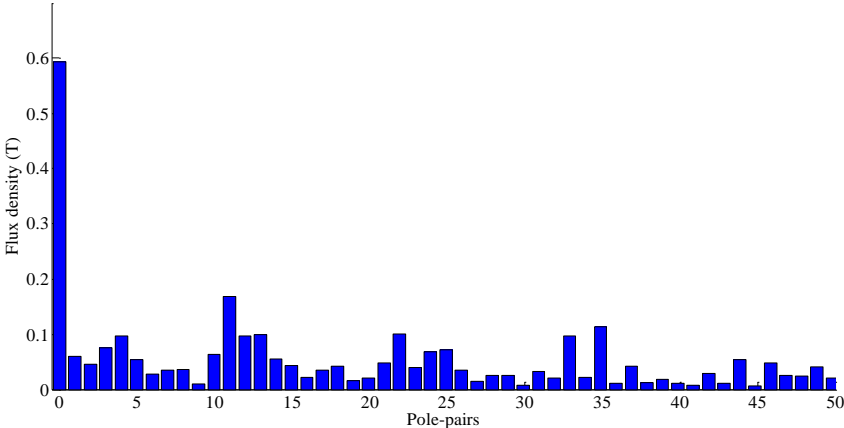


Fig. 3.4. Radial flux density in the inner airgap.

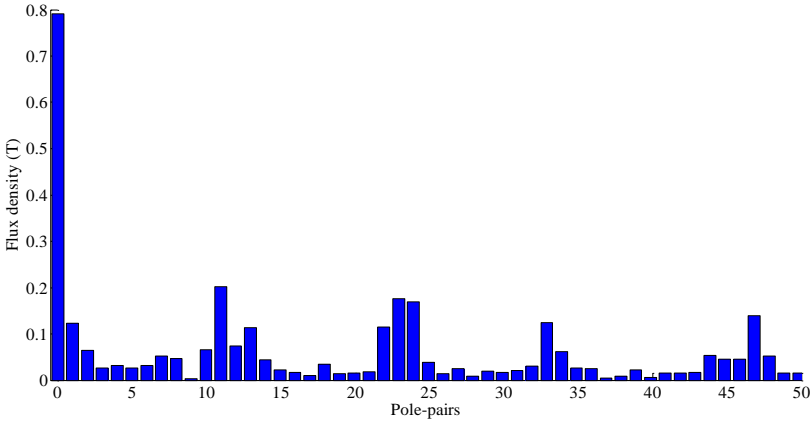


Fig. 3.5. Radial flux density in the outer airgap.

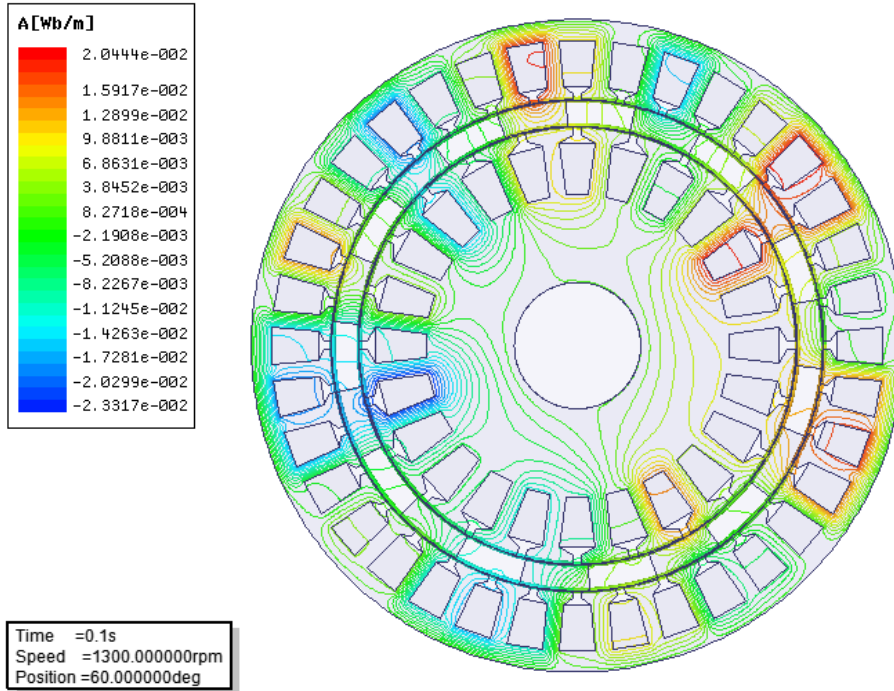


Fig. 3.6. Flux line contour.

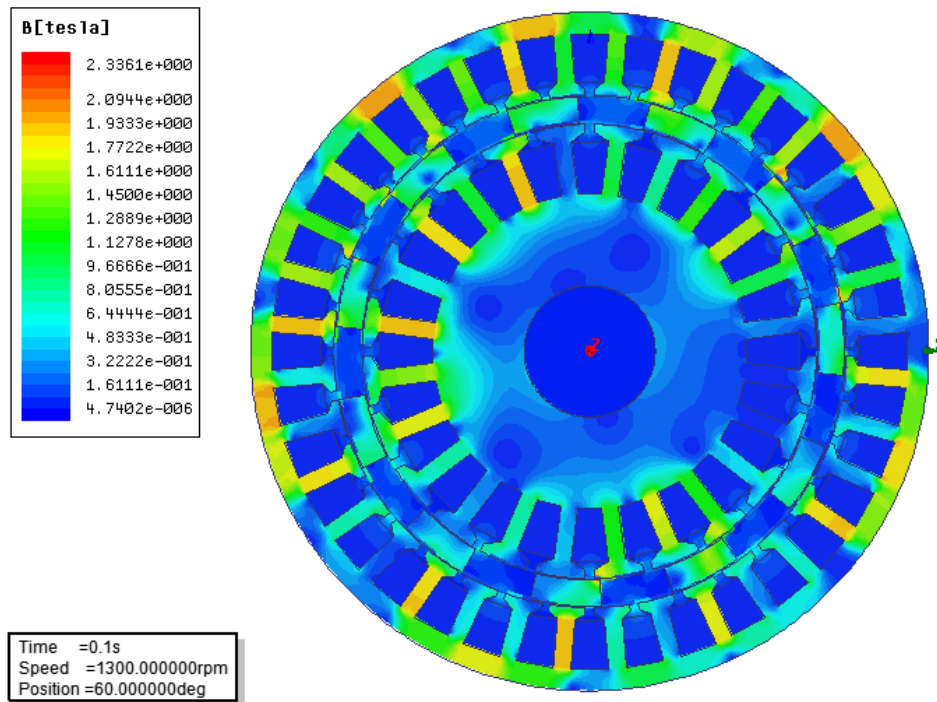


Fig. 3.7. Magnetic field distribution.

Table 3.2 compares performances of the torque, torque density, total loss, and efficiency of different motor structures. The proposed DFDS motor with the optimal design can achieve

larger torque density and higher efficiency compared with the doubly-fed reluctance motor. Due to the dual-stator structure its losses are also reduced, which means lower temperature rise. It also illustrates the effectiveness of the optimization method.

Table 3.2 Performances comparison of different motor structures

Motor structure	Torque (with the same total electric load) (N·m)	Torque density (with the same total electric load) (10 ⁻³ N·m/cm ³)	Total loss (with the same output torque) (W)	Efficiency (with the same output torque) (%)
Conventional induction motor	120	8.94	698	92.0
Doubly-fed reluctance motor	83	6.87	1087	88.1
DFDS motor with initial design	103	8.53	748	91.5
DFDS motor with optimal design	113	9.36	664	92.4

3.4 The experiment results of the DFDS motor

3.4.1 The test platform

A prototype of the proposed DFDS motor is fabricated for testing of its performance. Fig. 3.8 shows the outer stator wound with the outer windings. Fig. 3.9 shows the inner stator wound with the inner windings. Fig. 3.10 shows the middle rotor. An experiment platform, as shown in Fig. 3.11, is also established. The control system is based on Digital Signal Processor (DSP). Then the no-load and loaded performances of the DFDS motor are measured and the computed results are verified by experimental data.

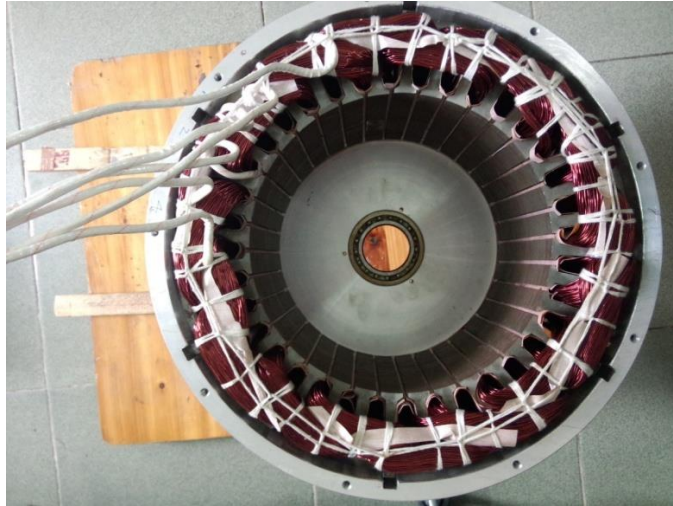


Fig. 3.8. The prototyped outer stator of the proposed DFDS motor.



Fig. 3.9. The prototyped inner stator of the proposed DFDS motor.



Fig. 3.10. The prototyped middle rotor of the proposed DFDS motor.

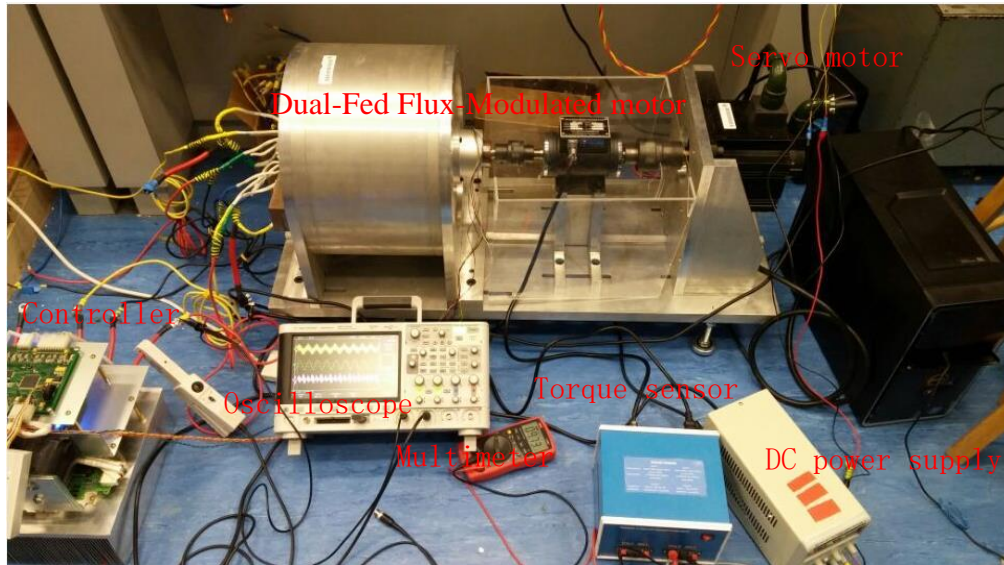


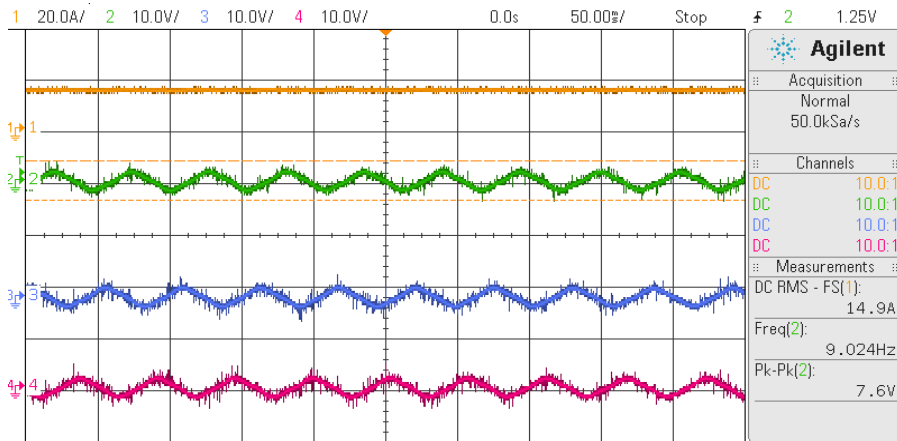
Fig. 3.11. The test system of the proposed DFDS motor.

3.4.2 No-load test

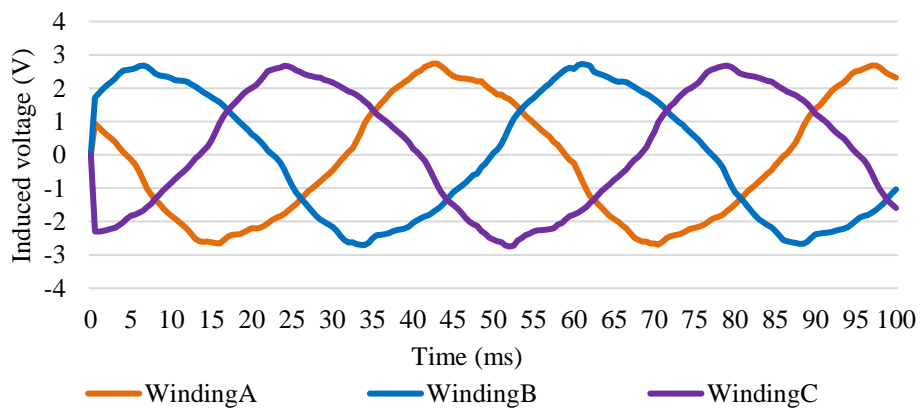
In experiment, a DC excitation ($I = 15 \text{ A}$) is applied to the phase *B* and phase *C* of outer winding when the rotor speed is 100 r/min, 200 r/min, 300 r/min, 400 r/min, 500 r/min, 600 r/min, 700 r/min, 800 r/min and 924 r/min (rated speed), respectively, and then the three-phase voltage of the inner winding are measured.

Similarly, a DC excitation ($I = 15 \text{ A}$) is applied to the phase *B* and phase *C* of the inner winding. The rotor is driven by the servo motor at different speeds. The three-phase voltage of the outer winding is measured and recorded. The experiment results and simulation results are compared.

Fig. 3.12 and Fig. 3.13 show the measured and simulated induced voltage of the inner windings at the speed of 100 r/min and 924 r/min, respectively. Fig. 3.14 and (b) Fig. 3.15 show the measured and simulated induced voltage of the outer windings at the speed of 100 r/min and 924 r/min, respectively. One can find that the measured induced voltage has very close values of frequencies and amplitudes with the simulated ones.

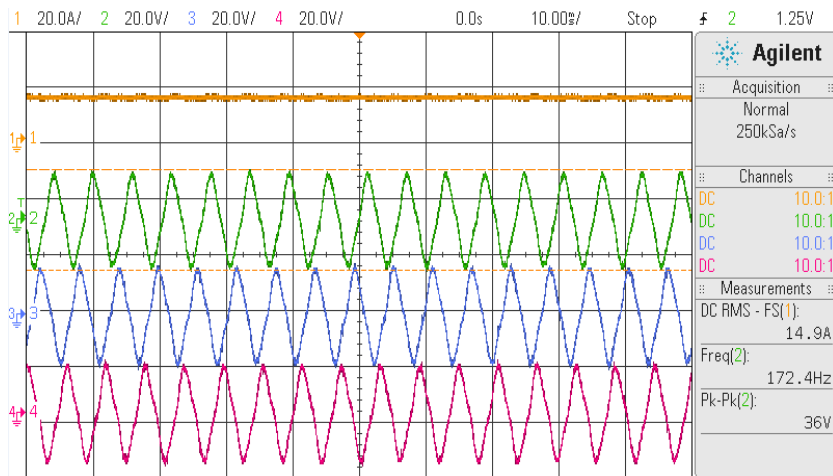


(a)

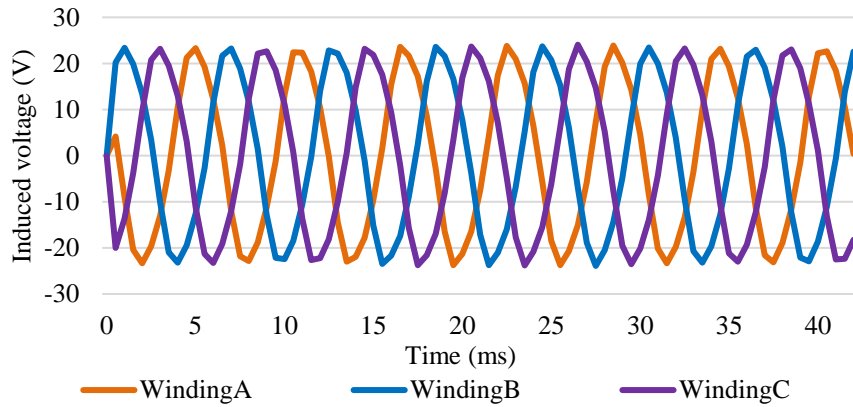


(b)

Fig. 3.12. Measured and simulated induced voltage of the inner winding at the speed of 100 r/min.

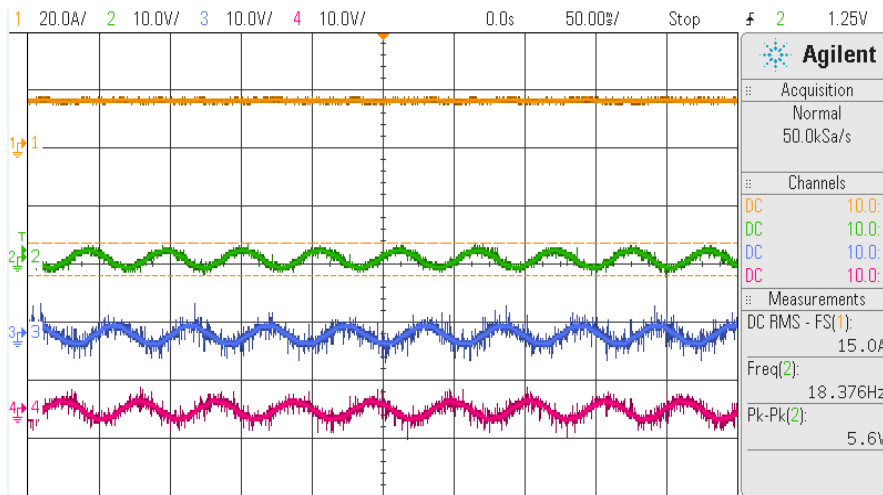


(a)

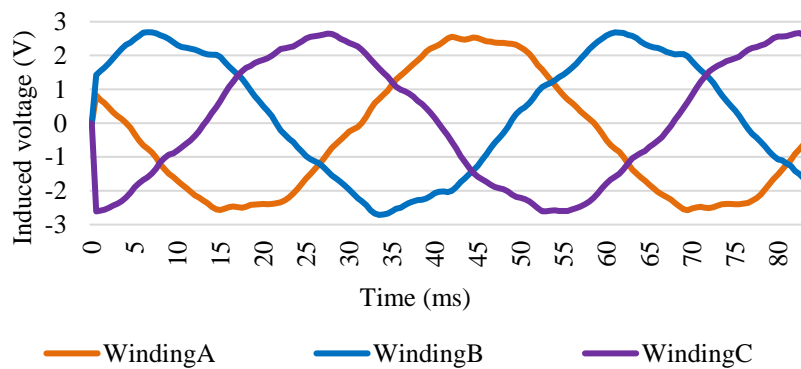


(b)

Fig. 3.13. Measured and simulated induced voltage of the inner winding at the speed of 924 r/min.

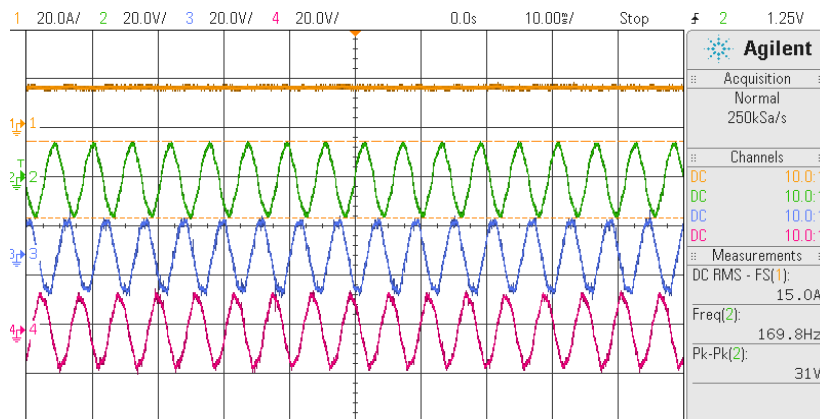


(a)

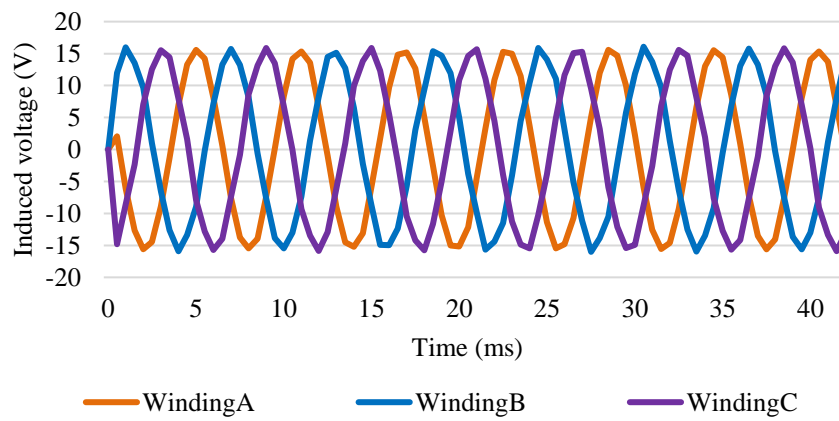


(b)

Fig. 3.14. Measured and simulated induced voltage of the outer winding at the speed of 100 r/min.



(a)



(a)

(b)

Fig. 3.15. Measured and simulated induced voltage of the outer winding at the speed of 924 r/min.

When the servo motor drives the motor to rotate at different speeds while the windings are in open circuit, all the output power of the servo motor is the mechanical loss, so the mechanical loss of the DFDS motor at different rotor speed can be obtained as shown in Fig. 3.16.

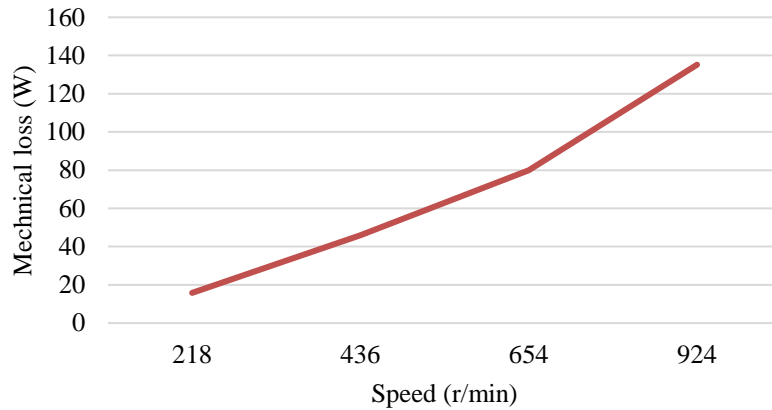


Fig. 3.16. No-load mechanical loss.

3.4.3 Loaded test

Firstly, an experiment has been done when the speed is 218 r/min to obtain the electromagnetic torque and current in two sets of windings in order to verify the relation between electromagnetic torque and winding current.

The results show that the electromagnetic torque is proportional to the product of the two currents of the inner and outer windings, that is $T \propto I_{\text{inner}} \times I_{\text{outer}}$. The rule may be broken if a saturation situation appears in the stator iron cores with rising currents. That is why the motor parameters should be designed and optimized with comprehensive consideration to ensure the condition is also satisfied at the rated speed.

In experiment, the frequencies of the two sets of windings are given in Table 3.3. One can find that when both f_{inner} and f_{outer} are 20 Hz, the rotor speed is 218 r/min. And when both f_{inner} and f_{outer} are 85 Hz, the rotor speed is 924 r/min which is the rated speed of the motor.

Table 3.3 The relation between frequencies and motor speed

Item	$f_{inner} +$ $f_{outer} =$ 40 Hz	$f_{inner} +$ $f_{outer} = 60$ Hz	$f_{inner} +$ $f_{outer} = 80$ Hz	$f_{inner} +$ $f_{outer} = 100$ Hz	$f_{inner} +$ $f_{outer} = 120$ Hz	$f_{inner} +$ $f_{outer} = 145$ Hz	$f_{inner} +$ $f_{outer} = 170$ Hz
Rotor speed (r/min)	218	327	436	545	654	764	924

The obtained results are in coincidence with the theoretical analysis, that is $n = 60 \times (f_{inner} + f_{outer}) / p_{Fe}$. The motor has been controlled using constant torque control method below the rated speed and flux-weakening control method above the rated speed. The mechanical characteristics of the proposed motor is shown in Fig. 3.17. The adjustment of the phase angle is adopted in the flux-weakening process. Fig. 3.18 and Fig. 3.19 show the measured current and induced voltage in the inner winding and outer winding at the speed of 218 r/min, respectively. Fig. 3.20 and Fig. 3.21 show the measured current and induced voltage in the inner winding and outer winding at the speed of 924 r/min, respectively.

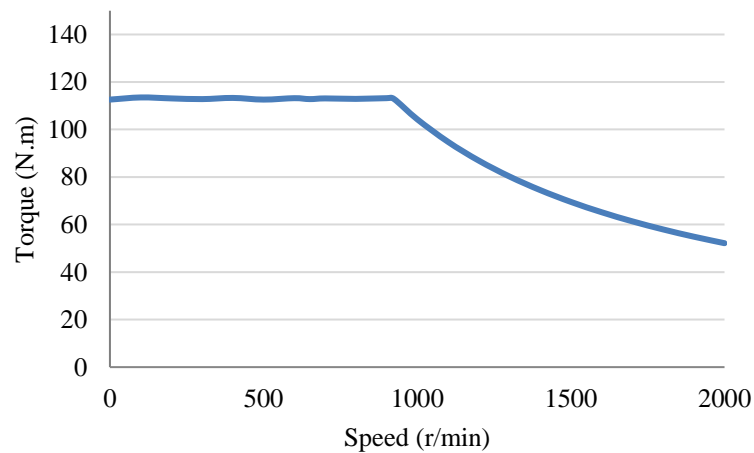


Fig. 3.17. The mechanical characteristics of the proposed motor.

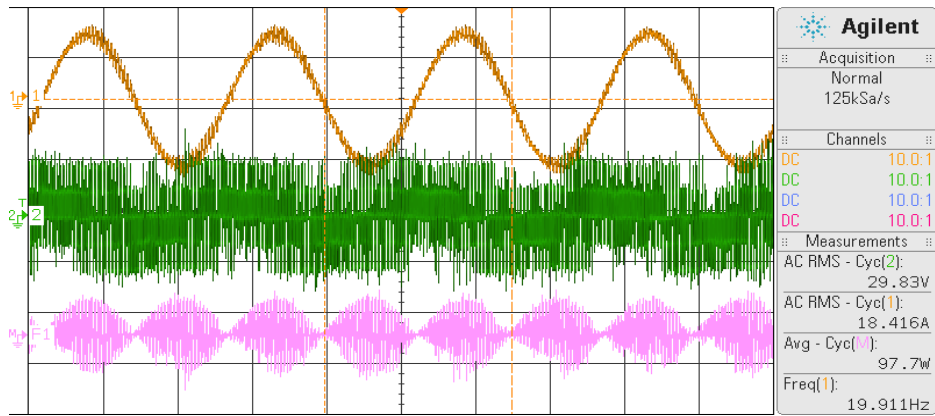


Fig. 3.18. Measured current and induced voltage in the inner winding at the speed of 218 r/min.

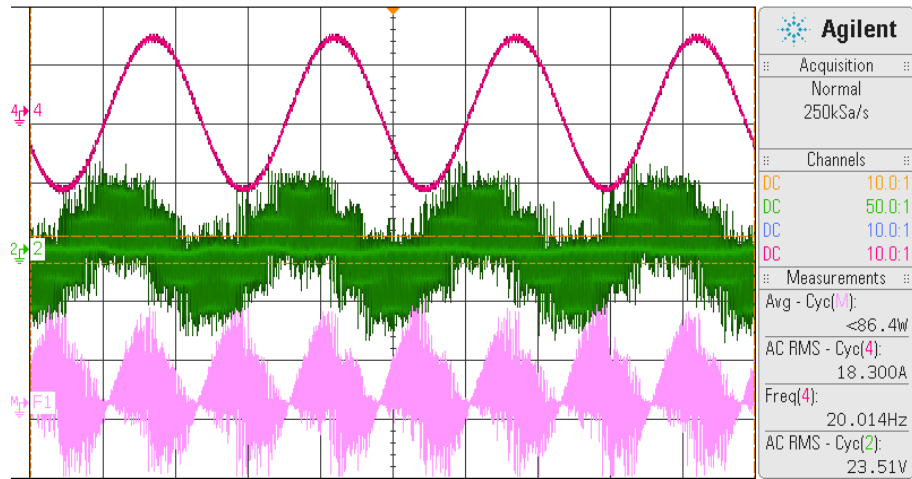


Fig. 3.19. Measured current and induced voltage in the outer winding at the speed of 218 r/min.

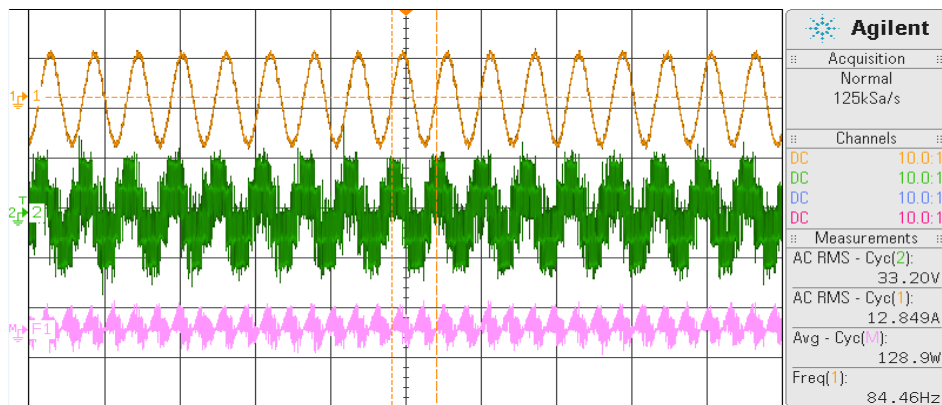


Fig. 3.20. Measured current and induced voltage in the inner winding at the speed of 924 r/min.

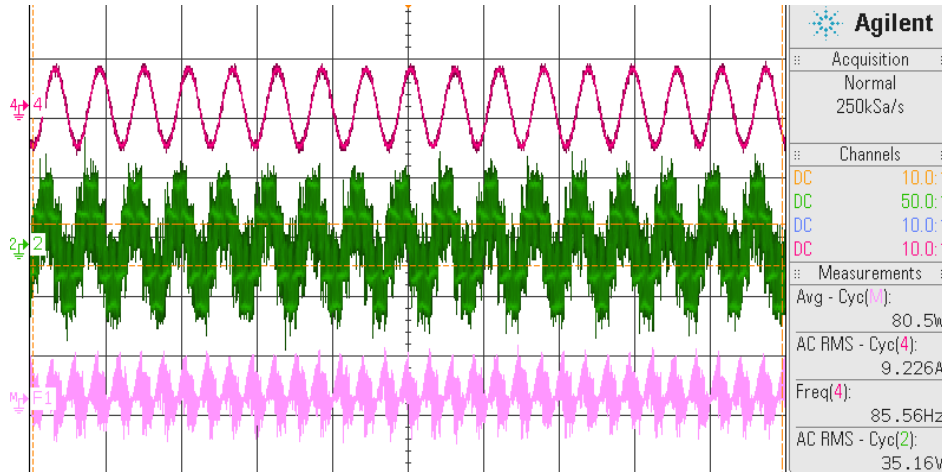


Fig. 3.21. Measured current and induced voltage in the outer winding at the speed of 924 r/min.

3.5 Conclusion

This chapter presents a doubly-fed dual-stator (DFDS) motor based on a unified theory of general flux-modulated machines which is proposed in the Chapter 2. A design method using numerical finite-element method (FEM) and optimization algorithm is performed to analyze the performance of the DFDS motor. A testing platform for the prototyped DFDS motor is established for performance verification. The experiment results verify the design concept of the proposed DFDS motor and show its outstanding potential.

Reference Part C

- [C1] W. N. Fu and S. L. Ho, "A quantitative comparative analysis of a novel flux-modulated permanent-magnet motor for low-speed drive," *IEEE Trans. Magn.*, vol. 46, no. 1, pp. 127-134, Jan. 2010.
- [C2] S. L. Ho, Shuangxia Niu, and W. N. Fu, "Design and Analysis of a Novel Axial-Flux Machine," *IEEE Trans. Magn.*, vol. 47, no. 10, pp. 4368-4371, Oct. 2011.

- [C3] Y. Fan, L. Zhang, M. Cheng, and K. T. Chau, "Sensorless SVPWM-FADTC of a new flux-modulated permanent-magnet wheel motor based on a wide-speed sliding mode observer," *IEEE Trans. Ind. Electron.*, vol. 62, no. 5, pp. 3143-3151, May 2015.
- [C4] J. Li, K. T. Chau, J. Z. Jiang, C. Liu, and W. Li, "A new efficient permanent magnet Vernier machine for wind power generation," *IEEE Trans. Magn.*, vol. 46, no. 6, pp. 1475-1478, Jun. 2010.
- [C5] L. Xu, G. Liu, W. Zhao, and X. Yang, "Hybrid stator design of fault-tolerant permanent-magnet Vernier machines for direct-drive applications," *IEEE Trans. Ind. Electron.*, vol. 64, no. 1, pp. 179-190, Jan. 2017.
- [C6] A. Toba and T. A. Lipo, "Novel dual-excitation permanent magnet Vernier machine," *Proc. Conf. Rec. IEEE IAS Annu. Meeting*, pp. 2539-2544, 1999.
- [C7] W. N. Fu, Yiduan Chen, and Xinhua Guo, "Novel dual-layer and three-layer permanent-magnet-excited synchronous motors," *IEEE Trans. Magn.*, vol. 51, no. 11, pp. 1-4, 2015.
- [C8] M. Cheng, W. Hua, J. Zhang, and W. Zhao, "Overview of stator-permanent-magnet brushless machines," *IEEE Trans. Ind. Electron.*, vol. 85, no. 11, pp. 5087-5101, Nov. 2011.
- [C9] Z. Q. Zhu, J. T. Chen, and Y. Pang, "Analysis of a novel multi-tooth flux-switching PM brushless AC machine for high torque direct-drive applications," *IEEE Trans. Magn.*, vol. 44, no. 11, pp. 4313-4316, Nov. 2008.
- [C10] J. Zhang, M. Cheng, Z. Chen, and W. Hua, "Comparison of stator-mounted permanent-magnet machines based on a general power equation," *IEEE Trans. Energy Convers.*, vol. 24, no. 4, pp. 826-834, Dec. 2009.
- [C11] C. Yu, S. X. Niu, S. L. Ho, and W. N. Fu, "Design and analysis of a magnetless double-rotor flux switching motor for low cost application," *IEEE Trans. Magn.*, vol. 50, no. 11, 2014.
- [C12] Y. Wang, S. L. Ho, W. N. Fu, and J. X. Shen, "A novel brushless doubly fed generator for wind power generation," *IEEE Trans. Magn.*, vol. 48, no. 11, pp.4172-4174, Nov. 2012.
- [C13] X. Y. Ma, G. J. Li, G. W. Jewell and Z. Q. Zhu, "Performance comparison of doubly salient reluctance machine topologies supplied by sinewave currents," *IEEE Trans. Ind. Electron.*, vol. 63, no. 7, pp. 4086-4096, Jul. 2016.
- [C14] F. Liang, L. Xu, and T. Lipo, "D-q analysis of a variable speed doubly AC excited reluctance motor," *Elect. Mach. Power Syst.*, vol. 19, pp. 125-138, Mar. 1991.
- [C15] Dawei Li, Ronghai Qu, and Jian Li, "Topologies and analysis of flux-modulation machines," *2015 IEEE Energy Conversion Congress and Exposition(ECCE)*, Canada, 20-24 Sept. 2015, pp. 2153-2160.

- [C16] L. Xu, F. Liang, and T. Lipo, "Transient model of a doubly excited reluctance motor," *IEEE Trans. Energy Conversion*, vol. 6, pp. 126-133, Mar. 1991.
- [C17] L. Jian, Y. Shi, C. Liu, G. Xu, Y. Gong, and C. C. Chan, "A novel dual permanent-magnet-excited machine for low-speed large-torque applications," *IEEE Trans. Magn.*, vol. 49, no. 5, pp. 2381-2384, May 2013.
- [C18] K. T. Chau, Z. Dong, J. Z. Jiang, L. Chunhua, and Z. Yuejin, "Design of a magnetic-g geared outer-rotor permanent-magnet brushless motor for electric vehicles," *IEEE Trans. Magn.*, vol. 43, no. 6, pp. 2504-2506, Jun. 2007.
- [C19] Yunchong Wang, S. L. Ho, W. N. Fu, and J. X. Shen, "A novel brushless doubly fed generator for wind power generation," *IEEE Trans. Magn.*, vol. 48, no. 11, pp. 4172-4175, Nov. 2012.
- [C20] W. N. Fu, P. Zhou, D. Lin, S. Stanton and Z. J. Cendes, "Modeling of solid conductors in two-dimensional transient finite-element analysis and its application to electric machines," *IEEE Trans. Magn.*, vol. 40, no. 2, pp. 426-434, Mar. 2004.
- [C21] W. N. Fu and S. L. Ho, "Enhanced nonlinear algorithm for the transient analysis of magnetic field and electric circuit coupled problems," *IEEE Trans. Magn.*, vol. 45, no. 2, pp. 701-706, Feb. 2009.
- [C22] W. N. Fu and S. L. Ho, "Elimination of nonphysical solutions and implementation of adaptive step size algorithm in time-stepping finite-element method for magnetic field - circuit - motion coupled problems," *IEEE Trans. Magn.*, vol. 46, no. 1, pp. 29-38, Jan. 2010.
- [C23] W. N. Fu, and S. L. Ho, "Extension of the concept of windings in magnetic field - electric circuit coupled finite-element method," *IEEE Trans. Magn.*, vol. 46, no. 6, pp. 2119-2123, June 2010.
- [C24] Siguang An, Shiyong Yang, S. L. Ho, Tao Li, and Weinong Fu, "A modified tabu search method applied to inverse problems," *IEEE Trans. Magn.*, vol. 47, no. 5, pp. 1234-1237, 2011.
- [C25] Siguang An, Lin Yang, Shiyong Yang, "An improved tabu search algorithm with application to single(multi)-objective optimization of inverse problems," Conference on Theory and Advance Technology of Electrical Engineering (CTATEE), 2009, pp. 192-195.

Chapter 4 Design and optimization of PM arrangement for a DPME synchronous motor

4.1 Introduction

Permanent magnet (PM) electric machines have wide applications as they can realize large electromagnetic torque transmission without extra external excitation [D1]. Most conventional PM synchronous motors have surface-mounted PM arrangement with N pole - S pole - N pole - S pole ... on the rotors. A magnetic gear (MG) can be directly combined with a conventional PM motor which will improve the system torque density significantly. However, it has the disadvantages of requiring two rotating parts and complicated mechanical structure [D2]. In [D3], a novel MG motor was presented in which MG is integrated into a conventional outer-rotor PM brushless motor, and it has only one rotary part, which is referred as a flux-modulated motor. In [D4], a dual-layer PM-excited (DPME) synchronous motor was presented which is designed with PMs on both stator and rotor. The PMs in the all slots have the same magnetization polarity. The PMs on the stator facing the air gap side are N poles and the PMs on the rotor facing the air gap side are S poles in consequent-pole-type PM arrangement. In this configuration the two sets of flux-modulated motor can be realized, and the torque density can be improved significantly.

In this chapter, different PM arrangements in a DPME synchronous motor are proposed,

which leads the motor having more competitive torque capability and higher efficiency compared with the conventional counterpart. The sizes of the PM configurations are determined by using multi-objective optimization algorithm. The performances of DPME synchronous motors with different PM arrangements are quantitatively analyzed and compared.

4.2 DPME motors with different PM arrangement

4.2.1 Conventional PM arrangement

A DPME synchronous motor with a conventional PM arrangement (Motor I) is shown in Fig. 4.1. The stator has 30 slots which carry one set of three-phase armature winding with p pole pairs. The rotor has 32 salient PM pole pairs with simple consequent-pole type arrangement of N pole - Iron - N pole - Iron ... as shown in Fig. 4.2. The main design parameters of the conventional DPME synchronous motor are listed in Table 4.1.

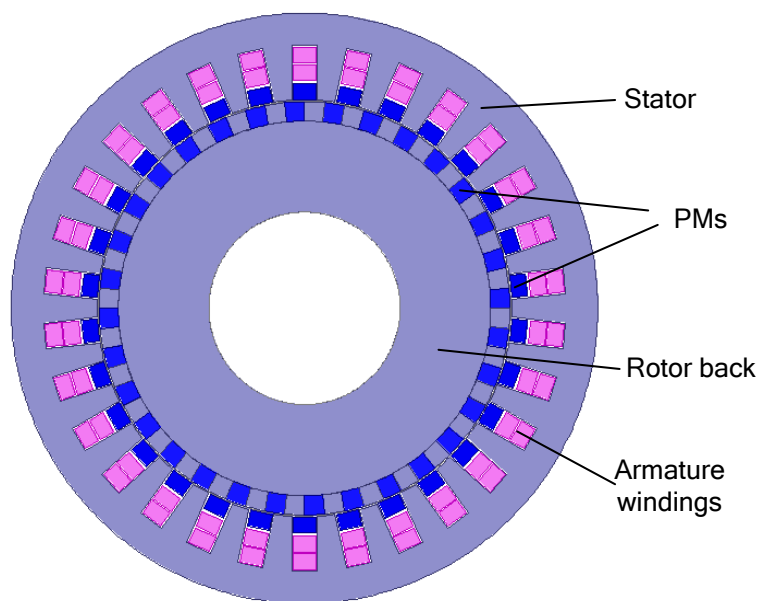


Fig. 4.1. DPME synchronous motor with the conventional PM arrangement (Motor I).

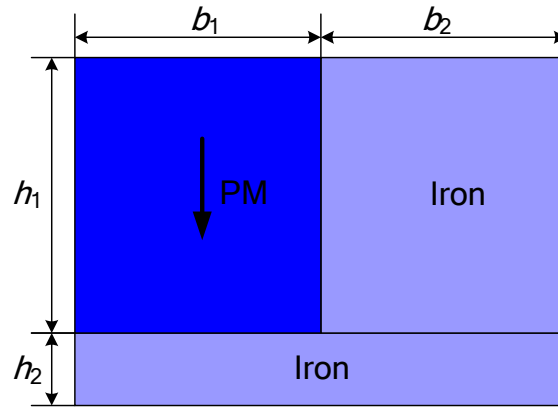


Fig. 4.2. A conventional PM arrangement in the rotor of Motor I.

There are four main parameters of the conventional PM arrangement, namely the thickness of PMs h_1 , the thickness of rotor back h_2 , the width of PMs with radial magnetization b_1 , and the width of ferromagnetic material on the rotor b_2 .

Table 4.1 Main design parameters of DPME motors

Parameter	Value
Axial length	40 mm
Outer radius of stator	92 mm
Inner radius of stator	65 mm
Length of airgap	0.6 mm
Inner radius of rotor	30 mm
The number of stator slots n_s	30
Pole pairs of the armature winding n_w	2
Pole pairs of the rotor n_r	32

According to the fundamental rule of flux modulation [D5-D7], for high output torque, in a flux-modulated machine the pole-pair numbers of different parts should meet the following relationship:

$$p_{PM} \pm p_W = p_{Fe} \quad (4.1)$$

where p_{PM} is the pole pairs of PMs; p_W is the pole pairs of the three-phase armature winding; and p_{Fe} is the number of ferromagnetic segments for flux modulation.

In this case, the pole pairs of the armature winding p_W , the pole pairs of the PMs on the rotor p_{PM_Rotor} , and the salient pole pairs produced by the open-slot structure in the stator p_{Fe_Stator} have the relationship as following:

$$p_{PM_Rotor} - p_W = p_{Fe_Stator} \quad (4.2)$$

The relationship meets the condition of a flux-modulated motor.

Furthermore, the pole pairs of the armature winding p_W , the pole pairs of the PMs in the stator p_{PM_stator} , and the salient pole pairs produced by the ferromagnetic segments in the rotor p_{Fe_Rotor} have the relationship as following:

$$p_{PM_Stator} + p_W = p_{Fe_Rotor} \quad (4.3)$$

The relationship also meets the condition of a flux-modulated motor.

4.2.2 Simplified consequent-pole Halbach array PM arrangement

A Halbach array magnet arrangement has attracted importance since it offers a number of attractive features. This arrangement can transmit a relatively high torque density whose magnet material is fully utilized, and it is very appropriate for slotless and brushless machines [D8-D10]. In this section, a simplified consequent-pole Halbach array PM arrangement is employed to replace the consequent-pole type one. A DPME synchronous motor with simplified consequent-pole Halbach array PM arrangement inserted in the rotor (Motor II) is shown in Fig. 4.3.

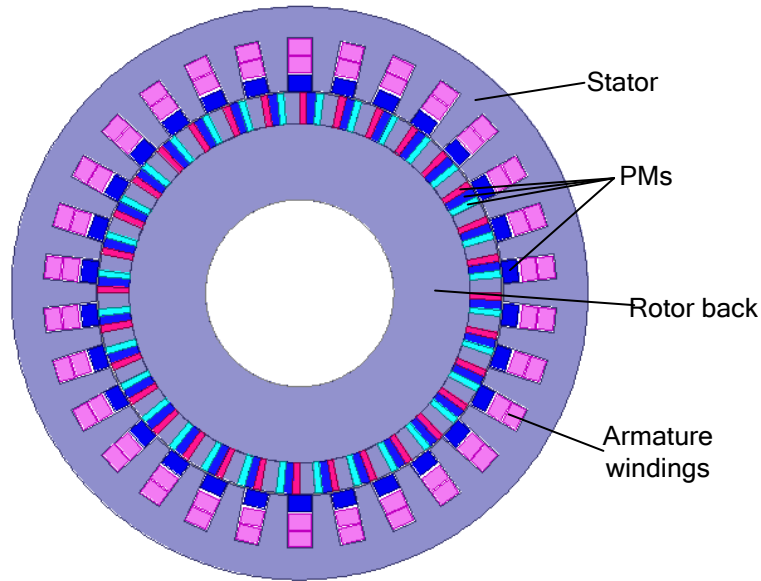


Fig. 4.3. DPME synchronous motor with simplified consequent-pole Halbach array PM arrangement inserted in the rotor (Motor II).

There are six main parameters of the simplified consequent-pole Halbach PM arrangement, namely the thickness of PMs on the rotor h_3 , the thickness of rotor back h_4 , the width of PMs with radial magnetization b_4 , the width of PMs with azimuthal magnetization b_3 , the width of PMs with opposite azimuthal magnetization b_5 , and the width of ferromagnetic material on the rotor b_6 , as shown in Fig. 4.4.

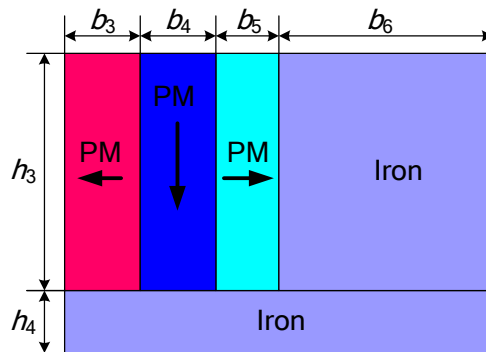


Fig. 4.4. A simplified consequent-pole Halbach array type PM arrangement in the rotor of Motor II.

4.2.3 Spoke type PM arrangement

As the spoke type PM arrangement of N pole - Iron - S pole - Iron - N pole - Iron ... which has the function of flux focusing can achieve high torque density and less centrifugal force [D11], the consequent-pole PMs in the stator slots can also be replaced by spoke type PMs. Then a new motor configuration (Motor III) can be achieved as shown in Fig. 4.5.

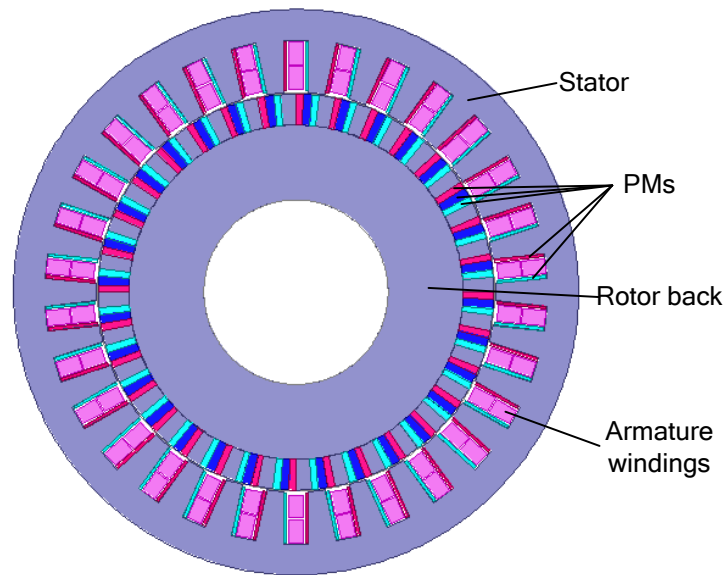


Fig. 4.5. DPME synchronous motor with simplified consequent-pole Halbach PM arrangement inserted in the rotor and spoke type PMs in the stator slots (Motor III).

There are six main parameters of the spoke type PM arrangement, namely the thickness of PMs in the stator slot h_5 , the thickness of stator yoke h_6 , the depth of the stator slot h_7 , the width of PMs with azimuthal magnetization b_7 , the width of PMs with opposite azimuthal magnetization b_9 , and the width of the stator teeth b_8 , as shown in Fig. 4.6.

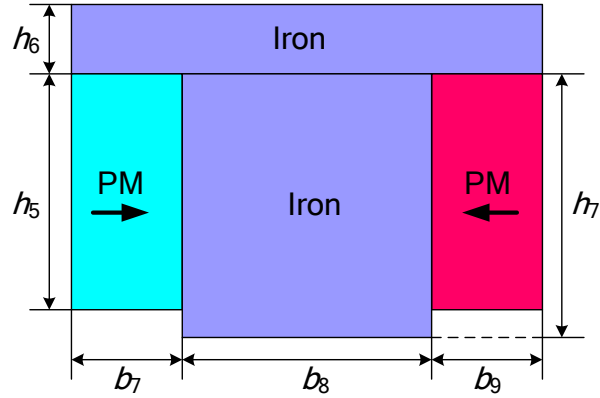


Fig. 4.6. A spoke type PM arrangement on the stator of Motor III.

4.3 Optimization of the DPME motors

A multi-objective genetic optimization algorithm, namely non-dominated sorting genetic algorithm-II (NSGA-II), is employed to find the optimal sizes of different PM arrangements. NSGA-II is the improved algorithm for NSGA. The simulation is conducted through the coupling of finite-element model and optimization procedure. The optimization process is shown in Fig. 4.7.

The objective function in this case is to reach high torque density and high efficiency of the motors. The rotor is rotated at a constant speed and the transient numerical solution is applied. The computer used to the optimization is 8-core and the RAM is 8 GB. The population is set as 40 and the maximum evaluations is 2000. To reduce the computing time, parallel computing method can be considered. The design parameters of the PM arrangements in Motor I, Motor II and Motor III are listed in Table 4.2, Table 4.3 and Table 4.4, respectively.

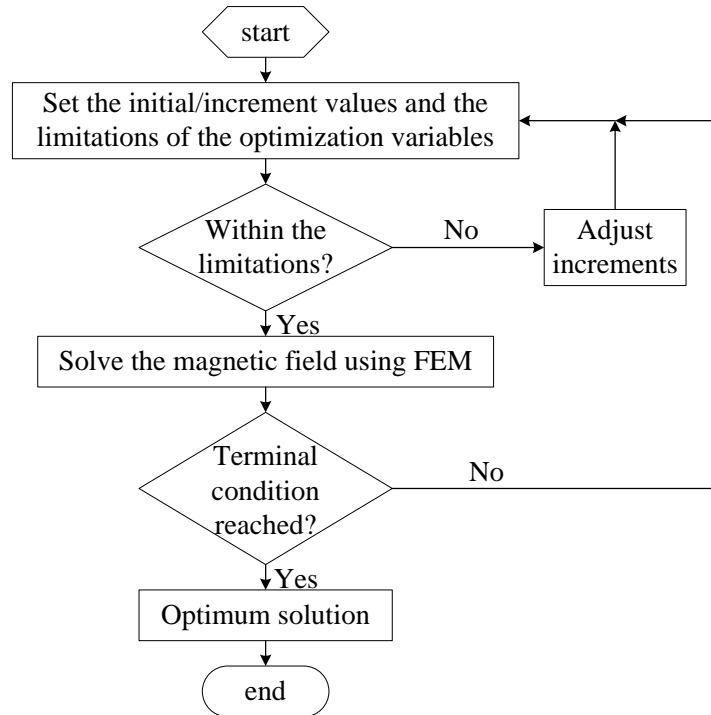


Fig. 4.7. The optimization process.

Table 4.2 Design parameters of the PM arrangement in Motor I

Parameter	Range	Step	Final value
Thickness of PMs on stator [mm]	4.0~6.0	0.1	5.0
Thickness of PMs on rotor h_1 [mm]	3.0~9.0	0.1	6.0
Width of PMs on the rotor b_1 [mm]	2.5~9.0	0.1	6.8
Width of ferromagnetic material on the rotor b_2 [mm]	2.5~9.0	0.1	4.5

Table 4.3 Design parameters of the PM arrangement in Motor II

Parameter	Range	Step	Final value
Thickness of PMs on the rotor h_3 [mm]	5.0~9.0	0.1	7.5
Width of PMs with radial magnetization on the rotor b_4 [mm]	1.6~4.6	0.1	2.7
Width of PMs with azimuthal magnetization on the rotor b_3 / b_5 [mm]	1.10~2.30	0.05	2.00
Width of ferromagnetic material on the rotor b_6 [mm]	3.3~5.6	0.1	4.4

Table 4.4 Design parameters of the PM arrangement in Motor III

Parameter	Range	Step	Final value
Thickness of PMs in the stator slot h_5 [mm]	13.0~18.0	0.1	14.5
Thickness of the stator yoke h_6 [mm]	8.0~13.0	0.1	11.5
Width of PMs with azimuthal magnetization on the rotor b_7 / b_9 [mm]	1.50~2.50	0.05	2.20
Width of the stator slot [mm]	9.5~11.0	0.1	10.5

4.4 Performance comparison

The magnetic fields of the three styles of motor configurations are analyzed using time-stepping finite element method (FEM) [D12-D14].

4.4.1 Torque waveforms

The electromagnetic torque waveforms of the three motor types are shown in Fig. 4.8. One can find that the torque of DPME synchronous motor with optimal simplified consequent-pole Halbach PM arrangement inserted in the rotor and spoke type PMs in the stator slots is improved significantly compared with the motor with the conventional PM arrangement.

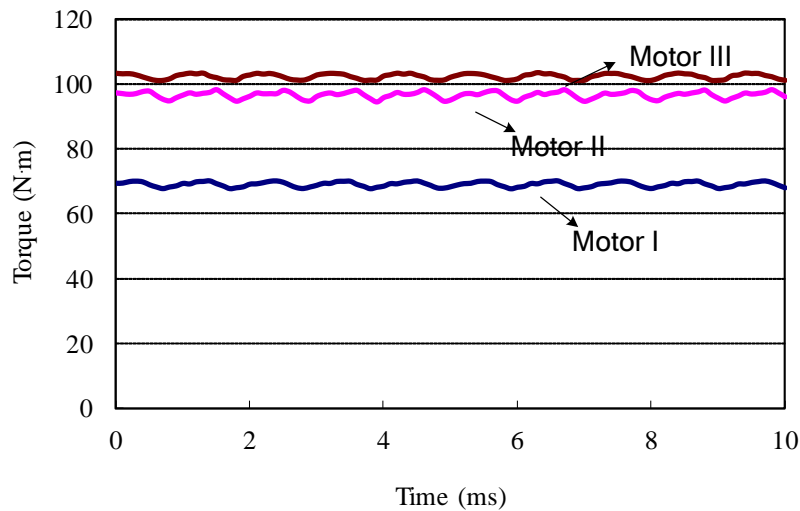


Fig. 4.8. The electromagnetic torque waveforms of the three motor types.

4.4.2 Back EMF

The three-phase no-load back EMF waveforms of Motor I, Motor II, and Motor III are shown in Fig. 4.9, Fig. 4.10 and Fig. 4.11, respectively.

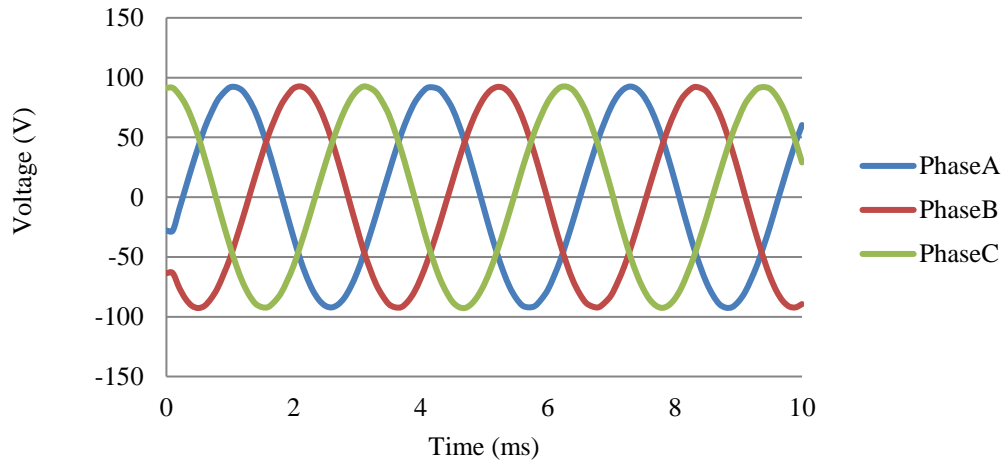


Fig. 4.9. The no-load back EMF of Motor I.

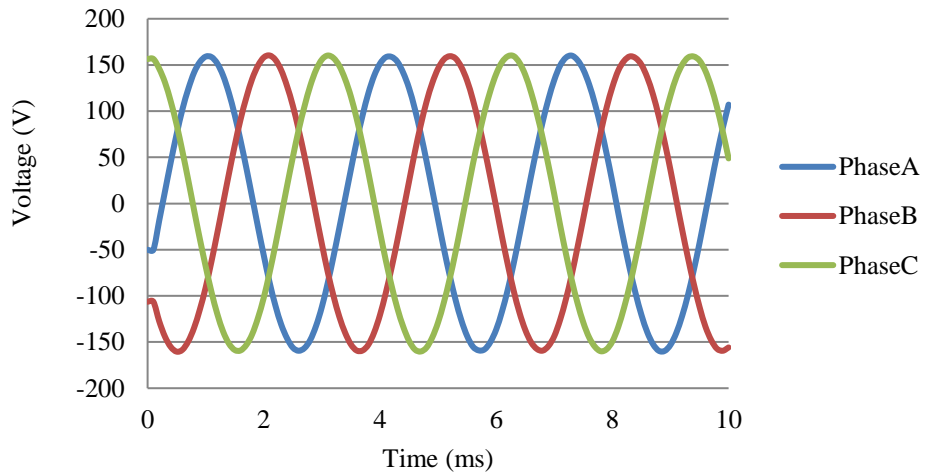


Fig. 4.10. The no-load back EMF of Motor II.

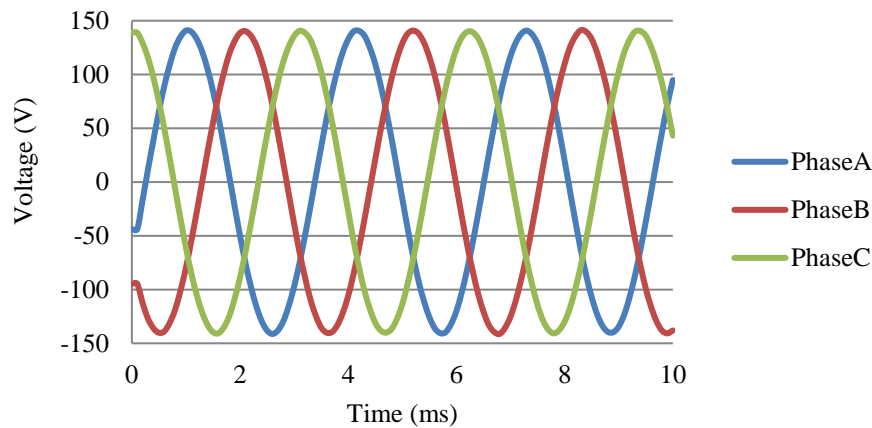
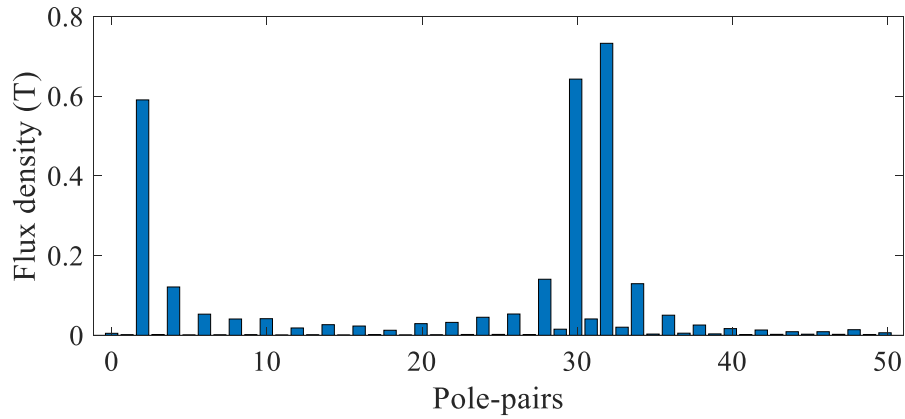


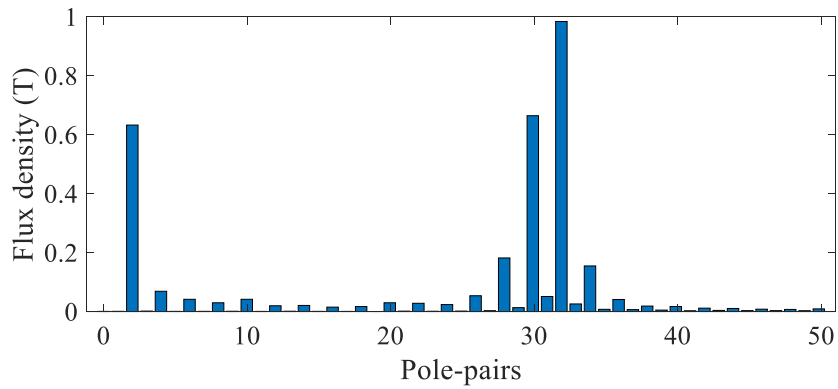
Fig. 4.11. The no-load back EMF of Motor III.

4.4.3 Space harmonics

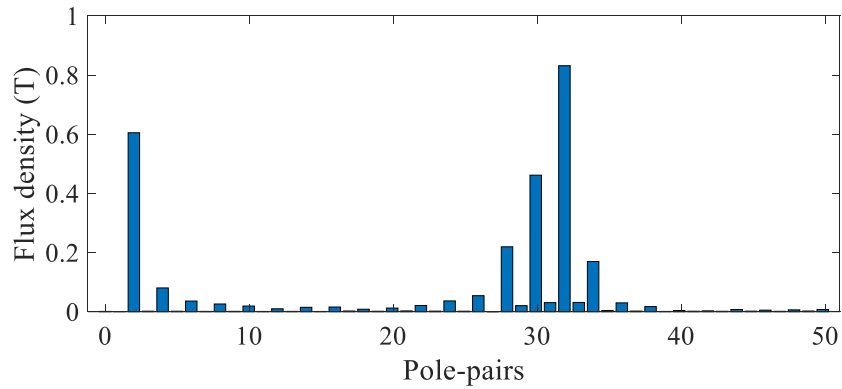
The space harmonics of magnetic flux density in the air gap of different motor configurations are shown in Fig. 4.12. From Fig. 4.12, one can see that the fields contain not only the 2 pole pairs component, 30 pole pairs component, and 32 pole pairs component, the 28th and 34th order harmonics are also significant due to the modulating effect of the ferromagnetic tooth in the rotor and the stator. The 2 pole pairs harmonic will react with the 2 pole pairs fundamental component of the armature field to produce a steady torque. The 30 pole pairs harmonic will interact with the magnetic fields excited by the stator PMs and contribute to torque transmission. The 32 pole pairs harmonic will also couple with the magnetic field excited by the rotor PMs when transmitting torque.



(a)



(b)



(c)

Fig. 4.12. The harmonic spectra of flux density in the air gap. (a) Motor I. (b) Motor II. (c) Motor III.

4.4.4 Torque comparison

The torque capability of the DPME synchronous motors with different PM arrangements are listed in Table 4.5. From Table 4.5, one can find that Motor II can produce 40% higher

electromagnetic torque than Motor I, and Motor III can transmit 5.9% higher electromagnetic torque than Motor II.

Table 4.5 Torque comparison of different motor configurations

Configuration	Torque (Nm)	Torque/Total volume	Torque/PM volume
		(kNm/m ³)	(kNm/m ³)
Motor I	68.99	65	781
Motor II	96.68	91	880
Motor III	102.34	96	709

4.4.5 Losses and efficiency comparison

The losses and corresponding power efficiency of the DPME synchronous motors with different PM arrangements are listed in Table 4.6. From Table 4.6, one can find that Motor III can reach 3.2% higher efficiency compared with Motor I while the total loss of the three motors are nearly equal.

Table 4.6 Performance comparison of different motor configurations

Configuration	Copper loss (W)	Core loss (W)	Solid loss	Output	Efficiency (%)
			(W)	Power (W)	
Motor I	173.11	214	27	4334.6	91.28
Motor II	173.11	200	35	6074.6	93.70
Motor III	176.00	194	26	6430.2	94.20

4.4.6 Flux and magnetic field distribution

The flux line contours and magnetic field distributions of the DPME synchronous motors with the three PM arrangements are shown in Fig. 4.13, Fig. 4.14, and Fig. 4.15, respectively.

The optimal PM arrangement is employed to achieve higher flux focusing effect and obtain higher torque.

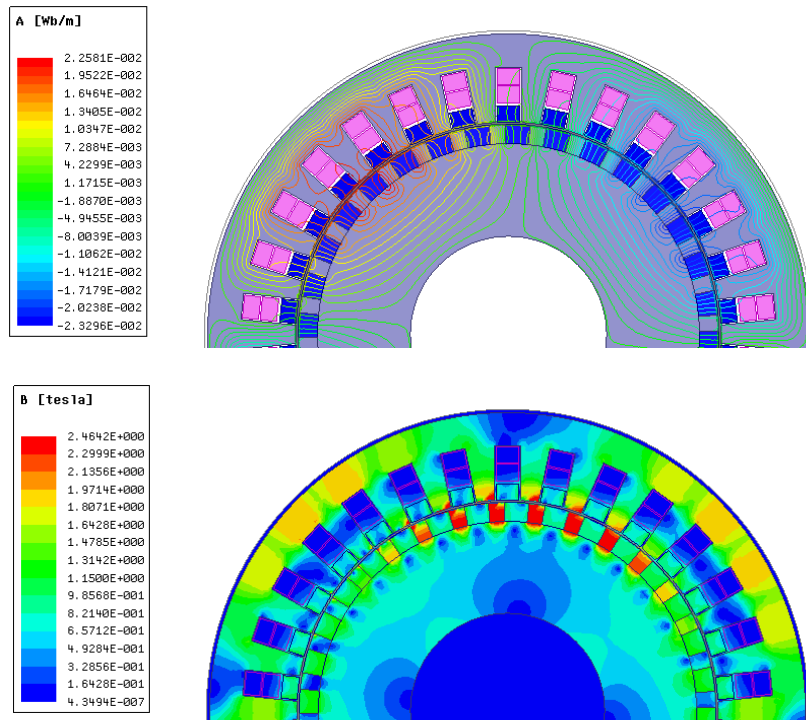


Fig. 4.13. The flux and magnetic field distributions of Motor I.

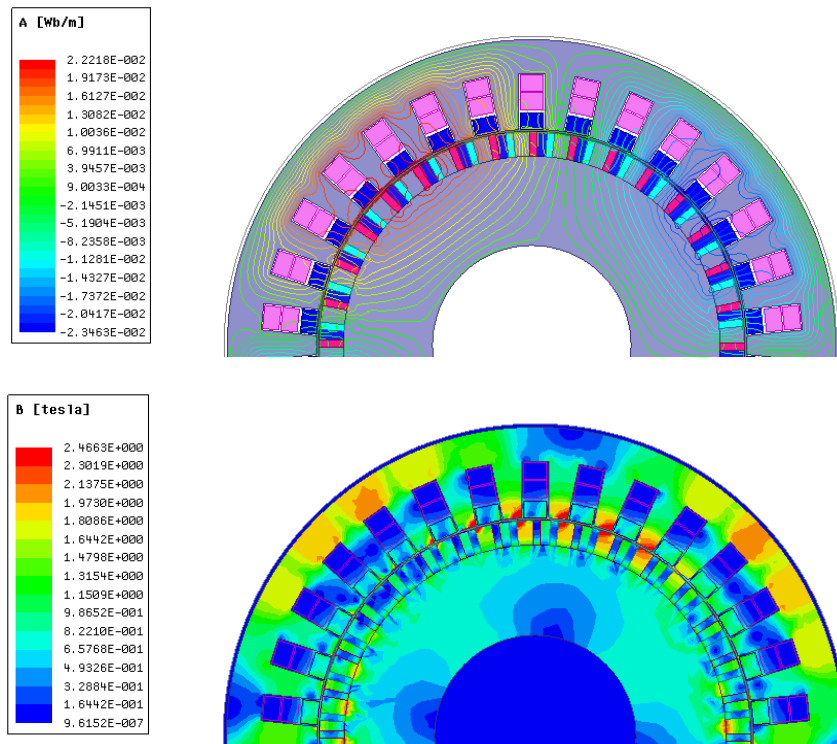


Fig. 4.14. The flux and magnetic field distributions of Motor II.

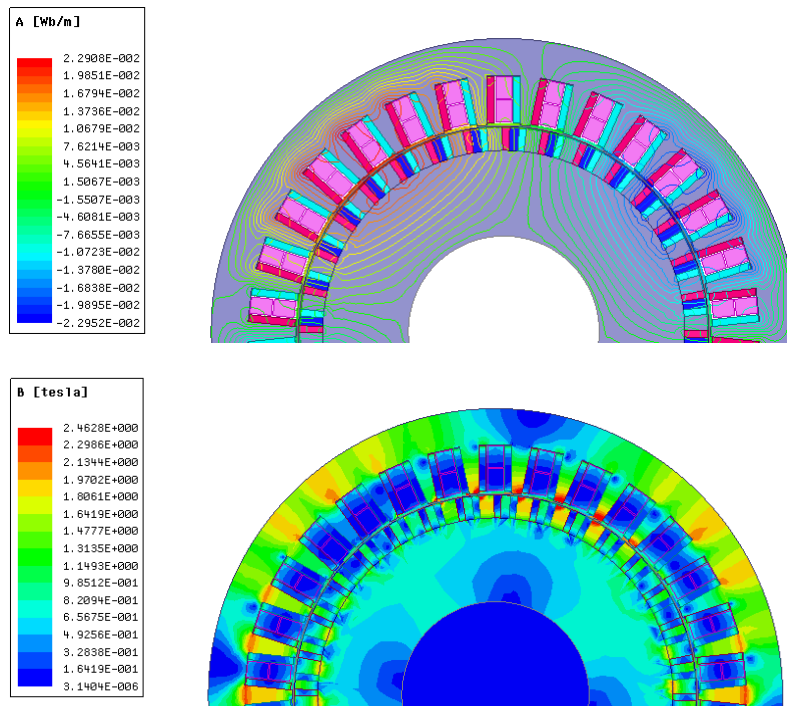


Fig. 4.15. The flux and magnetic field distributions of Motor III.

4.5 Conclusion

This chapter presents a performance comparison of DPME motors with different PM arrangements. The results show that the optimized DPME synchronous motor can achieve higher torque density and higher efficiency, but the utilization of PMs should be improved further. The optimization method for the PM arrangement can provide an effective design approach for PM machines.

Reference Part D

- [D1] S. L. Ho, S. Niu, and W. N. Fu, "Transient analysis of a magnetic gear integrated brushless permanent magnet machine using circuit-field-motion coupled time-stepping finite element method," IEEE Trans. Magn., vol. 46, no. 6, pp: 2074-2077, 2010.

- [D2] Jian Linni, K. T. Chau and J. Z. Jiang, "A magnetic-g geared outer-rotor permanent-magnet brushless machine for wind power generation," *IEEE Trans. Industry Applications*, vol. 45, no. 3, pp. 954-962, May-June 2009.
- [D3] L. L. Wang, J. X. Shen, Y. Wang and K. Wang, "A novel magnetic-g geared outer-rotor permanent-magnet brushless motor," 4th IET Conference on Power Electronics, Machines and Drives, 2-4 April 2008, pp. 33-36.
- [D4] R. Hosoya and S. Shimomura, "Apply to in-wheel machine of permanent magnet vernier machine using NdFeB bonded magnet - fundamental study," 8th International Conference on Power Electronics (ECCE), pp. 2208-2215, May 30 - June 3, Korea, 2011.
- [D5] W. N. Fu and S. L. Ho, "A quantitative comparative analysis of a novel flux-modulated permanent-magnet motor for low-speed drive," *IEEE Trans. Magn.*, vol. 46, no. 1, pp.127-134, Jan. 2010.
- [D6] S. L. Ho, S. Niu, and W. N. Fu, "Design and comparison of Vernier permanent magnet machines," *IEEE Trans. Magn.*, vol. 47, no. 10, pp. 3280-3283, 2011.
- [D7] S. Niu, S. L. Ho, W. N. Fu, and L. L. Wang, "Quantitative comparison of novel Vernier permanent magnet machines," *IEEE Trans. Magn.*, vol. 46, no. 6, pp. 2032-2035, 2010.
- [D8] Z. Q. Zhu, and D. Howe, "Halbach permanent magnet machines and applications: a review," *IEE Proc.-Electr. Power Appl.*, vol. 148, no. 4, pp. 299-308, July. 2001.
- [D9] Yang Shen, and Zi-Qiang Zhu, "General analytical model for calculating electromagnetic performance of permanent magnet brushless machines having segmented Halbach array," *IET Electrical Systems in Transportation*, vol. 3, no. 3, pp. 57-66, 2013.
- [D10] J. H. Lang, "A comparative analysis of torque production in Halbach and conventional surface-mounted permanent-magnet synchronous motors," *Conference Record of the 1995 IEEE Industry Applications Conference*, 8-12 Oct. 1995, vol. 1, pp. 657-663.
- [D11] P. O. Rasmussen, T. O. Andersen, F. T. Jorgensen, and O. Nielsen, "Development of a high-performance magnetic gear," *IEEE Trans., Ind. Appl.*, vol. 41, no. 3, pp. 764-770, May/June. 2005.
- [D12] W. N. Fu, P. Zhou, D. Lin, S. Stanton and Z. J. Cendes, "Modeling of solid conductors in two-dimensional transient finite-element analysis and its application to electric machines," *IEEE Trans. Magn.*, vol. 40, no. 2, pp. 426-434, March 2004.
- [D13] W. N. Fu and S. L. Ho, "Enhanced nonlinear algorithm for the transient analysis of magnetic field and electric circuit coupled problems," *IEEE Trans. Magn.*, vol. 45, no. 2, pp.701-706, Feb. 2009.

- [D14] D. Lin, P. Zhou, W. N. Fu, Z. Badics and Z. J. Cendes, "A dynamic core loss model for soft ferromagnetic and power ferrite materials in transient finite element analysis," *IEEE Trans. Magn.*, vol. 40, no. 2, pp. 1318-1321, March 2004.

Chapter 5 Three-layer PM-excited synchronous motor

5.1 Introduction

In low-speed large-torque applications, a mechanical gear is usually employed to lower the output speed of an electric motor to be applicable to mechanical load [E1]. However, the mechanical gear brings some problems, such as low energy transmission efficiency, high acoustic noises and more regular maintenance. Nowadays magnetic gears (MGs) may take the place of the mechanical ones [E2]. The MG can also be directly integrated with a conventional outer-rotor permanent magnet (PM) motor housed inside a low-speed rotating frame [E3-E5].

Increasing attentions are given to direct-drive electric machines, especially in the areas of wind power generation, electric vehicles, etc., as it is highly desirable to do away with the mechanical gearboxes. Common direct-drive machines usually refer to multi-pole PM machines without gears [E6]. They can operate at low speed with high power efficiency. In order to improve their performance, different topologies have been presented.

In recent years one hot research topic is a flux-switching motor which has PMs on its stator [E7]. It has the merits in some special applications, such as when there is a need for linear motors. Furthermore, a simple magnetic flux modulated motor that integrates MG with a conventional outer-rotor PM brushless motor has been presented recently [E8-E9]. As this

motor has only one rotary part, the output torque cannot be amplified. Its torque density is similar to or slightly larger than those from conventional PM motors [E8].

Actually, one effective and plausible method to increase the torque density is to properly increase the amount of the PMs inside the motors, as this is the only way to increase the strength of the magnetic field without energy consumption. In this section a novel dual-layer PM-excited (DPME) structure is presented first, which has PMs on both the stator and the rotor. Because of this DPME structure, the magnetic field strength can be improved and hence the output torque can be increased.

Along such direction, in this chapter, a novel triple-layer PM-excited (TPME) synchronous motor is further presented with the similar principle of the DPME motor, which has the merit of having a higher torque density than conventional synchronous motors and the DPME motor. The performances of the novel DPME and TPME synchronous motors are analyzed using time-stepping finite-element method (TS-FEM) and compared with those of a conventional PM synchronous motor, and a conventional DPME synchronous motor.

5.2 Configurations

5.2.1 Conventional PM synchronous motor

For the purpose to compare the performances of the proposed motors, the configuration of a conventional PM synchronous motor is shown in Fig. 5.1 and it is referred as Motor I. The key design data of this motor are listed in Table 5.1.

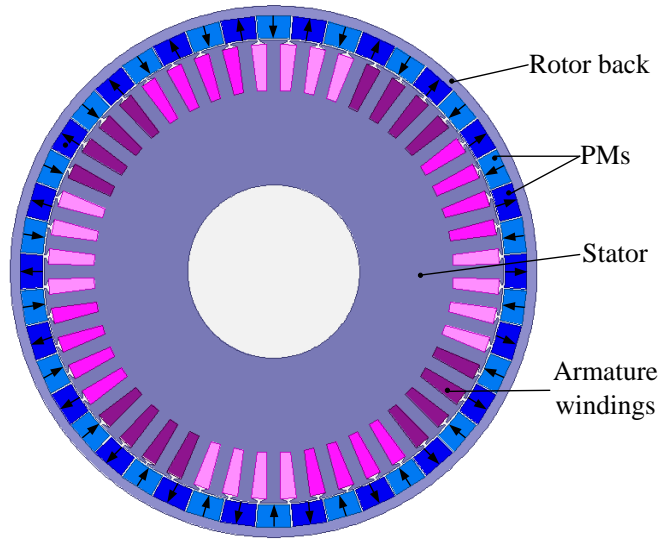


Fig. 5.1. A conventional outer-rotor PM synchronous motor (Motor I).

Table 5.1 Key design data of a conventional PM synchronous motor (Motor I)

Parameter	Value
Axial length	40 mm
Outside radius of outer rotor	92 mm
Outside radius of PMs	88.6 mm
Inside radius of PMs	80.8 mm
Outside radius of stator	80.2 mm
Number of outer rotor pole pairs	22
Number of stator slots	48

5.2.2 Conventional DPME synchronous motor

A conventional DPME synchronous motor [E10-E11] is shown in Fig. 5.2 and is referred as Motor II. There is a set of p pole-pair three-phase windings wound on the outer stator. The PMs in all the slots have the same magnetization polarity. The stator magnets facing the air gap side are N pole while the rotor magnet facing the air gap side are S pole.

Compared with the conventional flux-modulated PM motors [E8], the DPME motor is the same as the flux-modulated PM motors in that additional PMs are inserted inside the slots of the stator armature winding. The open-slot structure on the outer stator is employed to modulate the magnetic field which is produced by the windings and the PMs on the rotor.

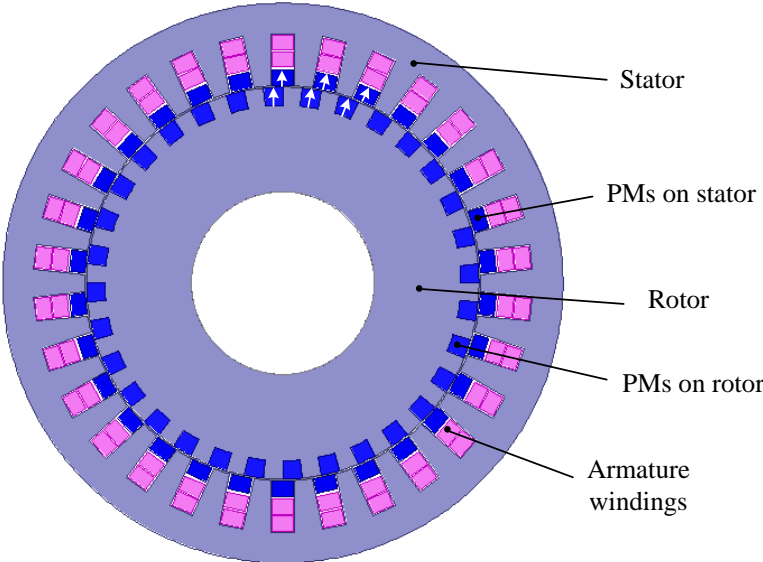


Fig. 5.2. A conventional DPME synchronous motor (Motor II).

5.2.3 New DPME synchronous motor

The configuration of the DPME synchronous motor proposed in this section is shown in Fig. 5.3 and it is referred as Motor III. Different from Motor II, it has an inner stator with a salient pole structure. The basic design data of this motor are listed in Table 5.2.

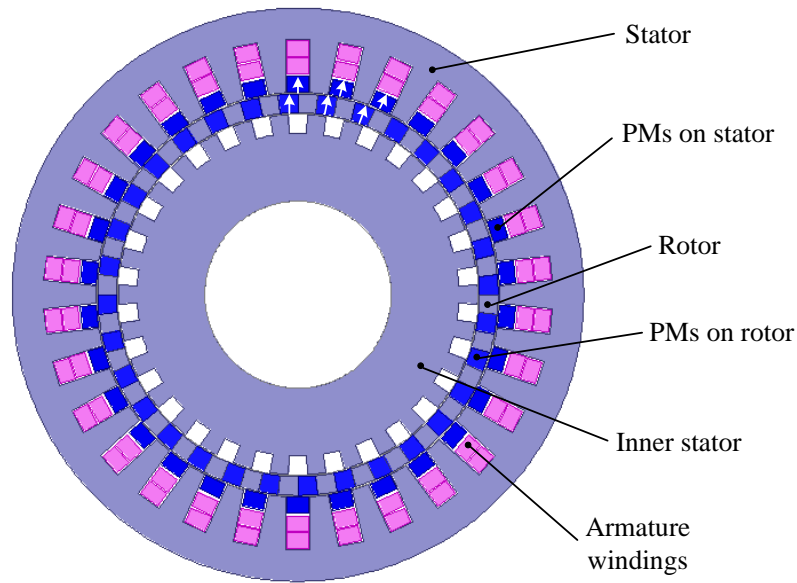


Fig. 5.3. The proposed novel DPME synchronous motor (Motor III).

Table 5.2 Main Design Parameters of the Motors

Parameter	Value
Axial length	40 mm
Outside radius of outer stator	92 mm
Inside radius of outer stator	65 mm
Outside radius of rotor	64.4 mm
Inside radius of rotor	58.4 mm
Outside radius of inner stator tooth	57.8 mm
Inside radius of inner stator tooth	51.8 mm
Number of stator slots	30
Number of armature winding pole pairs	2
Number of rotor pole pairs	32
Number of inner stator pole pairs	30

5.2.4 Novel TPME synchronous motor

The configuration of the TPME synchronous motor proposed in this paper is shown in Fig.

5.4 and it is referred as Motor IV. The design data of this motor are basically the same as the Motor III, except that it has PMs in the slots of the inner stator. Unlike conventional DPME structures, it has one outer stator and one inner stator arranged along the radial direction. The additional inner stator carries surface mounted PMs and it also has an open-slot structure.

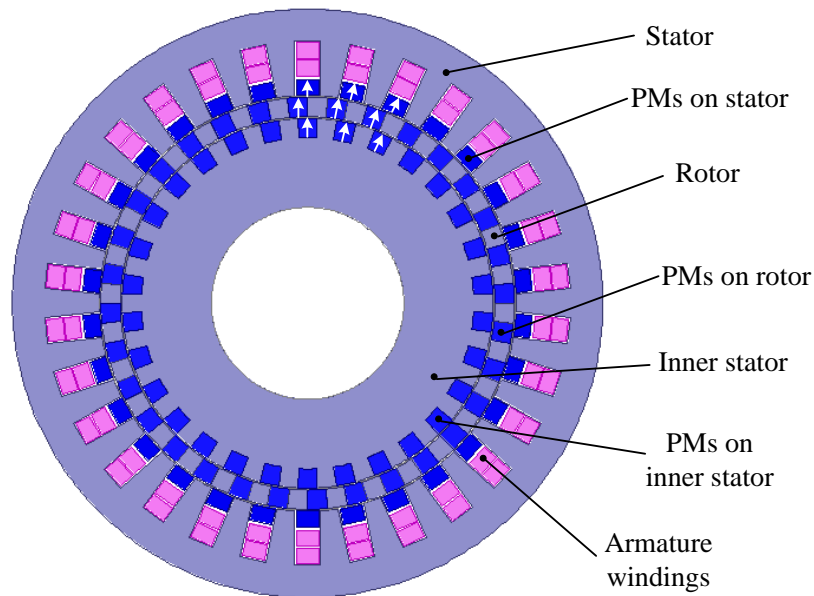


Fig. 5.4. The proposed novel triple-PM-excited (TPME) synchronous motor (Motor IV).

5.3 Working principle

According to the fundamental rule of flux modulation [D28-D31], in a flux-modulated machine the relationship of the pole-pair numbers of different parts should meet the following relationship

$$p_{PM} \pm p_W = p_{Fe}, \quad (5.1)$$

where p_{PM} is the number of pole pairs of PMs; p_W is the number of pole pairs of the three-phase armature winding; and p_{Fe} is the number of ferromagnetic segments for flux modulation.

The numbers of pole pairs and rotating speeds of each part should follow the following relationship

$$p_{PM}\omega_{PM} \pm p_W\omega_W = p_{Fe}\omega_{Fe}, \quad (5.2)$$

where ω_{PM} is the rotating speed of PMs; ω_{Fe} is the rotating speed of the ferromagnetic segments; and ω_W is the rotating speed of magnetic field produced by the stationary three-phase armature winding:

$$\omega_W = 2\pi f_W / p_W, \quad (5.3)$$

where f_W is the frequency of current in the stator winding.

In the DPME and TPME machines, the numbers of pole pairs of the stator winding, the PMs in the rotor, and the open-slot structure in the stator follow the relationship of

$$p_{PM_Rotor} - p_W = p_{Fe_Stator}, \quad (5.4)$$

where p_{PM_Rotor} is the number of pole pairs of PMs in the rotor; and p_{Fe_Stator} is the number of salient pole pairs produced by the open-slot structure in the stator. The relationship determined by Eq. 5.4 meets the condition of Eq. 5.1. Therefore, it constitutes a flux-modulated motor. According to Eq. 5.2, the speed ω_{Rotor} of the rotor can be determined by

$$p_{PM_Rotor}\omega_{Rotor} - p_W\omega_W = 0. \quad (5.5)$$

On the other hand, the numbers of pole pairs of the stator winding, the PMs in the stator, and the salient-pole structure in the rotor follow the relationship of

$$p_{PM_Stator} + p_W = p_{Fe_Rotor}, \quad (5.6)$$

where p_{PM_stator} is the number of pole pairs of PMs in the stator; and p_{Fe_Rotor} is the number of salient pole pairs produced by the ferromagnetic segments in the rotor. The relationship

determined by Eq. 5.6 also meets the condition of Eq. 5.1. Therefore, it constitutes another flux-modulated motor. According to Eq. 5.2, the speed ω_{Rotor} of the rotor can be determined by

$$P_W \omega_W = P_{Fe_Rotor} \omega_{Rotor} \cdot \quad (5.7)$$

In the proposed design,

$$P_{PM_Stator} = P_{Fe_Stator} \cdot \quad (5.8)$$

$$P_{Fe_Rotor} = P_{PM_Rotor} \cdot \quad (5.9)$$

substituting Eqs. 5.8 and 5.9 into Eqs. 5.6 and 5.7, one has

$$P_{Fe_Stator} + P_W = P_{PM_Rotor} \cdot \quad (5.10)$$

$$P_W \omega_W = P_{PM_Rotor} \omega_{Rotor} \cdot \quad (5.11)$$

The equation Eq. 5.10 is just the same as Eq. 5.4, and Eq. 5.11 is just the same as Eq. 5.5. It means that, the DPME and TPME machines can be realized in one integrated machine.

In this study the outer stator has 30 slots which carries one set of three-phase 2 pole-pair armature winding. The rotor has 32 salient PM pole pairs. The inner stator has 30 salient PM pole pairs.

Based on the magnetic fields produced by the armature windings and the PMs in the rotor side, the inner stator plays the same roles as the teeth-slots and PMs in the outer stator, resulting in corresponding increases in output torque from the motor. In the proposed TPME machine, when the rotor rotates,

(1) the windings and PMs on the outer stator, and the salient rotor constitutes one pair of

flux-modulated motor;

(2) the windings on the outer stator, the tooth-slot effect of the outer stator and the inner stator, together with the PMs on the rotor constitutes another pair of flux-modulated motor;

(3) the windings on the outer stator, the salient rotor, and the PMs on the inner stator constitutes yet the third pair of flux-modulated motor.

All electromagnetic torques produced by the three parts of motors will be added together and the overall torque being transmitted is enhanced significantly. The unused space inside the inner part of conventional motors can also be properly and fully utilized. Quantitative analysis using TS-FEM shows that the proposed machine has a better performance than its conventional counterparts.

5.4 Performance analysis

To evaluate the performance of these two proposed motors, a TS-FEM of magnetic field and mechanical motion coupled computation is employed to evaluate the electromagnetic torque comprehensively [E12]. To reveal the advantage of the proposed DPME and TPME synchronous motors, their performances are compared with motors designed on conventional topologies.

To demonstrate the merits of the novel PM motors, the output torques are compared with various conventional synchronous motors. For the sake of making a fair comparison on the performances of different configurations, the same constraints are employed to determine all their geometric parameters, including the axial length of iron core stack, outside frame radius, number of conductors in each slot, stator pole-pair number, and rotor pole-pair number as

well as the thickness of PMs. They also have the same electrical loading (the product of electric current in the windings and the total number of conductors in all slots). The excitation currents in the motor windings are assumed to be sinusoidal at a frequency of 320 Hz. The rated rotor speed is 600 rpm.

5.4.1 Torque waveforms

The torque curves at full load with different configurations are shown in Fig. 5.5. From Fig. 5.5 one can see that the average full-load torque of the proposed TPME synchronous motor is 98.6 Nm. In essence, the proposed TPME synchronous motor (Motor IV) is a perfect combination of three flux-modulated PM synchronous motors inside one frame with the same overall machine size. It takes full advantage of the motor space to allow it to output very large torque when compared with other motors with the same geometrical size and electrical loading.

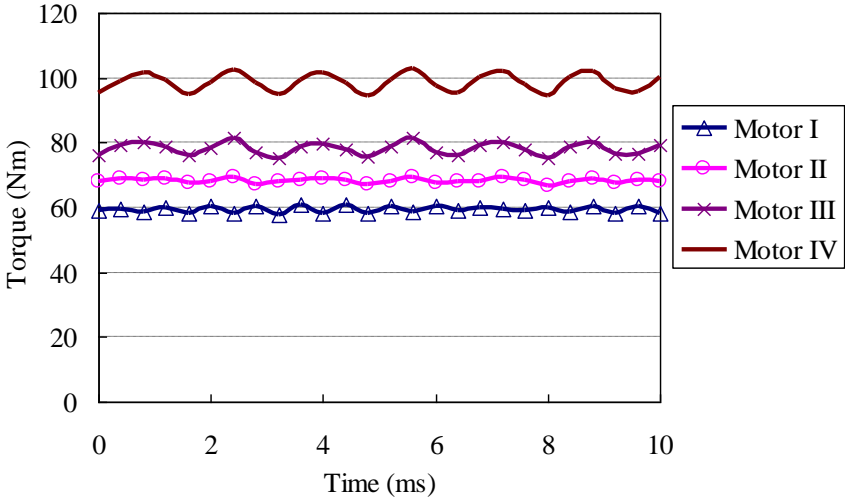


Fig. 5.5. Torque at full-load operation with different configurations.

5.4.2 Flux line contours

The flux line contours of different configurations are shown in Fig. 5.6. The yoke area of the

inner rotor is not fully used in Motor II. In Motor III, the inner yoke area is utilized to produce additional variation of magnetic reluctance along the circumferential direction of the air-gap, but it is not fully utilized as PMs can also be added inside all slots.

As the proposed motors have fully utilized its space to carry PMs, they can reach a higher output torque when using the same overall volume of the machine. Consequently, the proposed DPME and TPME synchronous motors are good choices in low-speed drives.

From Fig. 5.6 one can see that the full use of inner yoke area enhances the magnetic field strength in the motor, which results in higher torque density. To avoid the influence of saturation on the performance comparison of different configurations, appropriate geometrical parameters have been chosen using optimization method.

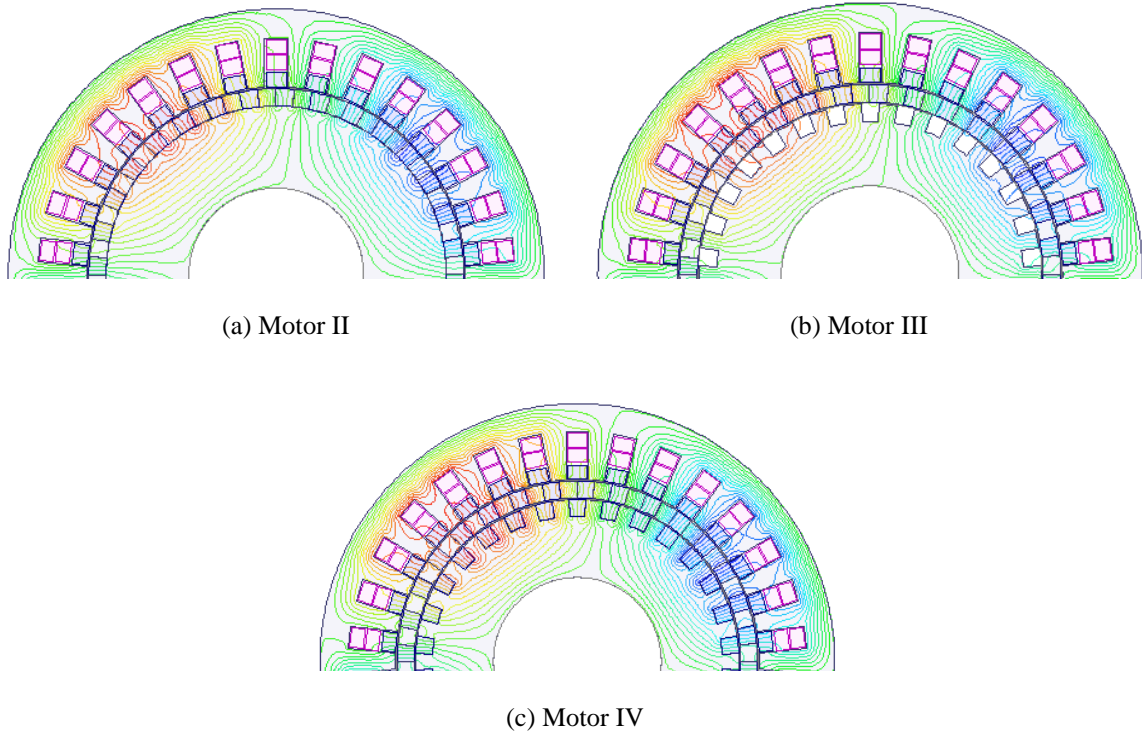


Fig. 5.6. Flux line contour of different configurations.

5.4.3 Comparison of torque density

The characteristic data of these four afore-mentioned motors are summarized in Table 5.3, and the torques per unit volume of total motor and the torques per unit volume of magnets are compared. It can be shown that the torque per unit volume of total motor of the proposed TPME synchronous motor is the highest among the four configurations; and the torque per unit volume of magnets of the proposed DPME synchronous motor is the highest among the four configurations. Quantitative numerical analysis has shown that the proposed DPME synchronous motor can offer at least 37.5% higher torque density when compared to that of the conventional PM synchronous motor, and the proposed TPME synchronous motor can offer about 70% higher torque density when compared to that of the conventional PM synchronous motor.

Table 5.3 Torque comparison of four configurations

Configuration	Torque/Total volume (kNm/m ³)	Torque/PM volume (kNm/m ³)
Motor I	56	384
Motor II	65	773
Motor III	77	885
Motor IV	95	761

5.4.4 Losses and efficiency comparison

The input power, copper loss regarding windings, core loss, eddy-current loss in magnets, and corresponding power efficiency of the four afore-mentioned motors are summarized in Table 5.4. The mechanical loss is ignored in this discussion. It can be shown that the copper loss, core loss and eddy-current loss in PMs become larger as the amount of PM materials used is increased. However, as the output powers also increase, their power efficiencies are

not low. The quantitative numerical analysis has shown that the proposed TPME synchronous motor can keep high efficiency when compared to that of the conventional PM synchronous motor.

Table 5.4 Performance comparison of four configurations

Configuration	Input Power (W)	Copper loss (W)	Core loss (W)	Eddy-current loss in PMs (W)	Efficiency (%)
Motor I	3962.1	134.48	87	6	94.25
Motor II	4703.16	172.24	212	27	91.26
Motor III	5286.29	172.24	179	23	92.92
Motor IV	6560.96	172.24	165	28	94.43

5.5 Conclusion

This chapter presents two novel PM motors in low-speed applications. The structure of the first novel configuration has extra PMs in the outer stator and extra salient teeth in an inner stator when compared with conventional PM motors; and the structure of the second novel configuration has three PM layers when compared with conventional PM motors, which creatively constitutes multi motors inside one frame with only one shared set of three-phase armature windings, resulting in significant increases in the output torque density. Their performances are elaborated using TS-FEM. They have significant advantage of producing a high torque density at full load when compared to those of their conventional counterparts. Based on the FEM analysis result, the proposed DPME motor can output an additional 37.5% more torque when compared to that by a conventional PM synchronous motor. The proposed TPME motors can output an additional 70% more torque with a similar power efficiency when compared to that by a conventional PM synchronous motor.

Reference Part E

- [E1] K. Atallah, and D. Howe, "A novel high-performance magnetic gear," *IEEE Trans. Magn.*, vol. 37, no. 46, Jul 2001, pp. 2844 - 2846.
- [E2] K. Atallah, S. D. Calverley and D. Howe, "Design, analysis and realisation of a high-performance magnetic gear," *IEE Proceedings - Electric Power Applications*, vol. 151, no. 2, Mar 2004, pp. 135-143.
- [E3] C. C. Huang, M. C. Tsai, D. G. Dorrell and B. J. Lin, "Development of a magnetic planetary gearbox," *IEEE Trans. Magn.*, vol. 44, no. 3, March 2008, pp. 403-412.
- [E4] K. T. Chau, C. C. Chan, and C. Liu, "Overview of permanent-magnet brushless drives for electric and hybrid electric vehicles," *IEEE Trans. Ind. Electron.*, vol. 55, no. 6, pp. 2246–2257, Jun. 2008.
- [E5] L. Jian, K. T. Chau, and J. Z. Jiang, "A magnetic-gearing outer-rotor permanent-magnet brushless machine for wind power generation," *IEEE Trans. Ind. Appl.*, vol. 45, no. 3, pp. 954–962, May–Jun. 2009.
- [E6] J. Chen, C. V. Nayar, and L. Xu, "Design and finite-element analysis of an outer-rotor permanent-magnet generator for directly coupled wind turbines," *IEEE Trans. Magn.*, vol. 36, no. 5, pp. 3802–3809, Sep.2000.
- [E7] M. Cheng, W. Hua, J. Z. Zhang, and W. X. Zhao, "Overview of stator-permanent magnet brushless machines," *IEEE Trans. Industrial Electronics*, vol. 58, no. 11, pp. 5087-5101, Nov. 2011.
- [E8] W. N. Fu and S. L. Ho, "A quantitative comparative analysis of a novel flux-modulated permanent-magnet motor for low-speed drive," *IEEE Trans. Magn.*, vol. 46, no. 1, pp.127-134, Jan. 2010.
- [E9] A.B. Proca, A. Keyhani, and A. EI-Antably, "Analytical model for permanent magnet motors with surface mounted magnets," *IEEE Trans. Energy Conversion*, vol. 18, no. 3, pp.386-391, Sept. 2003.
- [E10] Y. Tasaki, Y. Kashitani, R. Hosoya, and S. Shimomura, "Design of the Vernier machine with permanent magnets on both stator and rotor side," *7th International Power Electronics and Motion Control Conference - ECCE Asia*, 2 - 5 June, 2012, China, pp. 302 - 309.
- [E11] A. Ishizaki, T. Tanaka, K. Takasaki, and S. Nishikata, "Theory and optimum design of PM Vernier motor," *IEE Proceedings - Electric Machines and Drives*, 11 - 13 September, 1995, pp. 208 - 212.

- [E12] W. N. Fu, P. Zhou, D. Lin, S. Stanton and Z. J. Cendes, "Modeling of solid conductors in two-dimensional transient finite-element analysis and its application to electric machines," *IEEE Trans. Magn.*, vol. 40, no. 2, March 2004, pp. 426-434.

Chapter 6 Dual-electrical-port synthetic-slot PM motor

6.1 Introduction

Transport electrification has been proposed as a promising solution when facing increasingly urgent challenges regarding global warming, environmental pollution, and energy crisis. Recently, the concept of vehicle-to-grid is becoming compelling. With the aid of bidirectional power conversion technologies, electric vehicles (EVs) can be directly connected to a power grid, rather than simply drawing power from the grid, and feed energy from the onboard batteries back to the grid when needed. Therefore, the EVs can also be considered as a distributed energy storage system with the benefit to the balance of the demand and supply in the electricity market in the future. The vehicle-to-grid option can assist to improve the reliability and efficiency of the power grid, as well as reduce the overall cost and carbon emission [F1-F4]. Nevertheless, different from conventional hybrid EVs, this kind of EVs requires to be equipped with large volume batteries and the onboard electric drive system supplies the main electric power. Thus, the research on high performance drive motors which can offer strong power with light weight and compact size has become attractive for the development of EVs.

In-wheel motors, getting rid of complicated transmission mechanisms, have become competitive candidates for the electric drive systems of EVs [F5-F6]. Recently, most in-wheel motors are designed with very high rated speed (higher than 3000 r/min) to achieve

high power density. A speed reduction planetary mechanical gear is employed to match with relatively low speed of the wheels (around 1000 r/min). However, the mechanical gears have inevitable shortcomings, such as mechanical vibration, audible noise, frictional losses, and the need for regular maintenance and lubrication. To overcome these issues, in-wheel direct-drive motors, which can offer direct-drive operation without speed reduction gears, have been put forward [F7-F8]. Low torque density is the biggest bottleneck of the in-wheel motors. The demand for high rated torque usually results in bulky motor size and heavy weight [F9]. This not only makes it difficult for the motor to be mounted inside the wheels, but also affects the dynamic performance of the vehicle. Therefore, the in-wheel direct drive has become the future direction of EV technology, as it can realize distributed and flexible control according to vehicle's operating conditions.

Permanent magnet (PM) electric machines have wide applications as they can realize large electromagnetic torque transmission without extra external excitation [F10]. Effective utilization of PM materials will obviously improve the torque capability of the in-wheel motors, promote the overall efficiency and reduce the temperature rise. Magnetic gear (MG) can be directly combined with a conventional PM machine which will improve the system torque density significantly. However, it has the disadvantage of requiring two rotating parts and complicated mechanical structure [F11]. In [F12], a flux-modulated motor was designed with only one rotary part in which a MG is integrated into a conventional outer-rotor PM brushless motor. Most of PM machines have PMs mounted only on the stator or only on the rotor [F13-F17]. In [F18], a dual-PM-excited (DPME) synchronous motor was presented which was designed with PMs on both the stator and the rotor. The PMs in all the slots have the same magnetization polarity. The PMs on the stator facing the air gap side are N poles and the PMs on the rotor facing the air gap side are S poles, as a consequent-pole-type PM

arrangement.

In this chapter, a synthetic-slot permanent-magnet (SSPM) motor is presented. It can be regarded as a combination of an outer-rotor dual-flux-modulated PM motor and an inner-rotor flux-modulated motor. A novel general synthetic-slot structure is proposed and employed to the stator slots of the proposed SSPM motor to achieve high torque density. The proposed SSPM motor can offer considerably high torque capability and relatively small cogging torque, as well as wide speed range and high power efficiency in all four-quadrant operations, so as to satisfy the specific requirements in vehicle applications.

6.2 Machine configurations

A conventional outer-rotor PM machine, as shown in Fig. 6.1, is designed for performance comparison. One preliminary design of the proposed synthetic-slot PM motor for the in-wheel direct drive in EVs is shown in Fig. 6.2. A general pattern of the synthetic-slot structure is proposed, as shown in Fig. 6.3. In the synthetic slot, one piece of PM may be mounted in the opening of the slot and magnetized along the radial direction. Other two pieces of PMs may be installed on the two inner sides of the slot and magnetized along peripheral clockwise direction and anti-clockwise direction, respectively, to produce flux focusing effect. As deep slots may be intentionally designed, the large surface area of the PMs can produce high magnetic flux density in the air gap of the proposed SSPM motor. To reduce the magnetic reluctance in the magnetic circuit of the PMs in the slot, ferromagnetic material is also properly embedded in the slot. Therefore, the slot contains synthetic materials, including copper, PMs, ferromagnetic materials, and insulators. In contrary to existing PM machines in which the PMs are usually equipped on the rotor, the proposed

SSPM motor employs PMs both on the rotor and inside the stator slots.

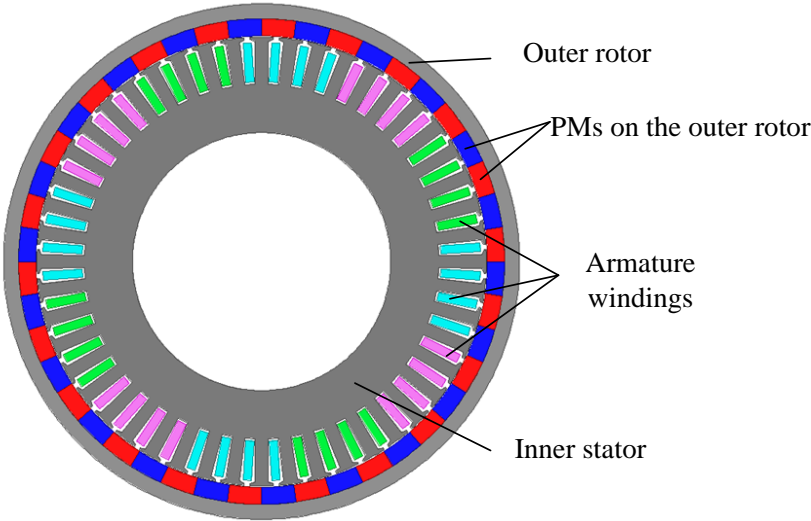


Fig. 6.1. A conventional PM motor.

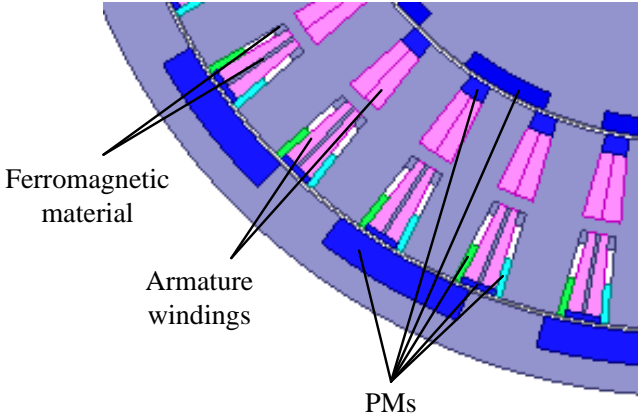
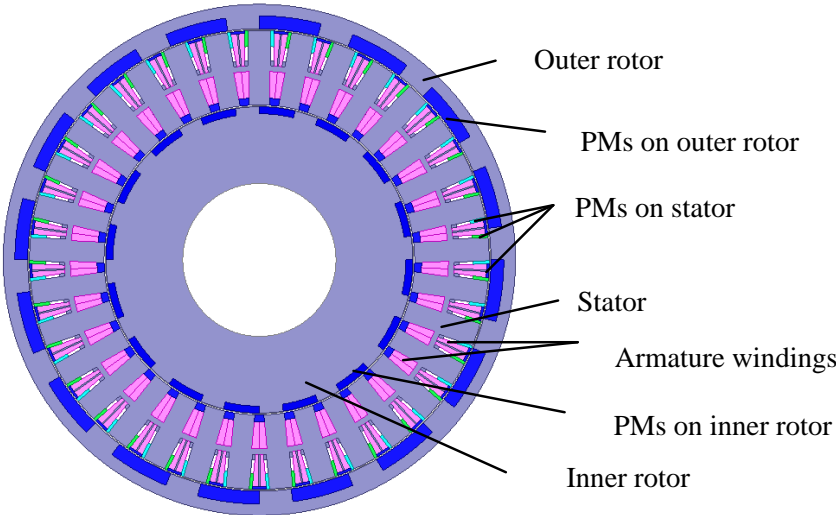


Fig. 6.2. The proposed SSPM motor and partially enlarged detail.

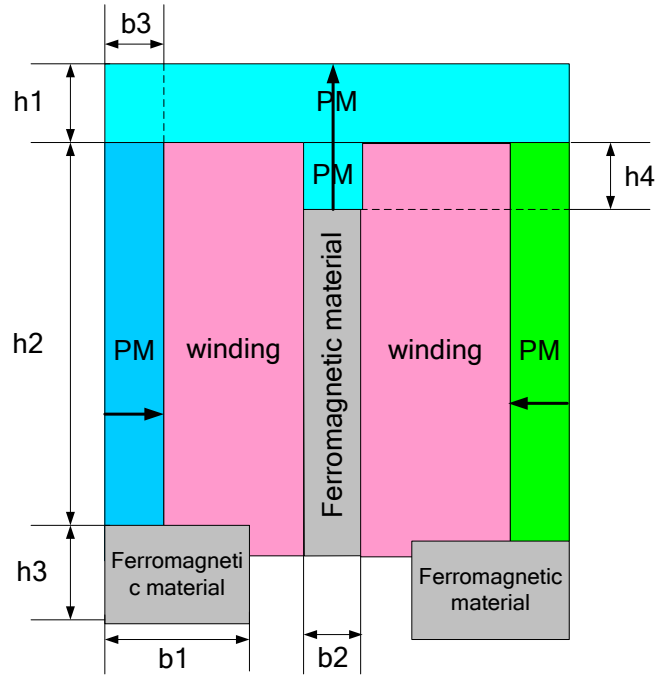


Fig. 6.3. A general pattern of the synthetic-slot structure.

6.3 Working principle of the SSPM motor

The operating principle of the outer-rotor PM motor in the proposed SSPM motor lies in the dual-flux-modulation method [F19-F21]. If ignoring the nonlinear factors of the magnetic field, the outer-rotor part of the proposed SSPM motor can be regarded as the combination of two separate machines, one is rotor-PM-excited machine and the other is stator-PM-excited machine. The outer armature windings with p_w pole pairs, the PMs on the outer rotor with p_2 pole pairs, and the Z_1 teeth serving as modulation teeth on the outer stator, produce a flux-modulated machine. Their pole pairs and the outer stator teeth meet the condition of

$$Z_1 = p_2 + p_w \quad (6.1)$$

Different from conventional electric machines, this outer-rotor PM motor in the proposed machine has PMs in each outer stator slot. The outer armature windings with p_w pole pairs, the PMs in the outer stator slots with p_1 pole pairs, and the Z_2 teeth serving as modulation

teeth on the outer rotor, realize a flux-switching machine. Their pole pairs and rotor teeth meet the condition of

$$Z_2 = p_1 - p_w \quad (6.2)$$

In this design, one intentionally lets $p_2 = Z_2$, which means that the outer rotor has been designed with a consequent-pole PM arrangement; one also intentionally lets $p_1 = Z_1$, which means that the stator also has consequent-pole PMs in the stator slots. Therefore, the equations (6.1) and (6.2) can be satisfied simultaneously, which means that these two machines can all work simultaneously. Once these two machines are combined into one frame with a shared stator armature winding, it will offer higher torque capability than one separate single-flux-modulated machine.

The operating principle of the inner-rotor PM motor in the proposed SSPM motor also lies in the dual-flux-modulation method. The pole pairs of the inner armature windings, the pole pairs of the PMs on the inner rotor, and the number of the modulated teeth on the inner stator meet the condition (6.1). The pole pairs of the inner armature windings, the pole pairs of the PMs in the inner stator slots, and the number of the modulated teeth on the outer rotor meet the condition (6.2).

6.4 Design and optimization of the SSPM motor

6.4.1 Excitation distribution of the two sets of windings

The proposed SSPM motor is particularly suitable for in-wheel direct drive in EVs. With the dual-electrical-port structure it gets rid of the complicated transmission mechanisms to serve as a powerful, flexible, compact, and high efficient drive system for EVs. Its application can further increase the drive distance as well as reduce the greenhouse gas emission and the

reliance of fossil fuels.

The combination of the excitation distribution in the inner windings and the outer windings plays a vital role in the power conversion of the motor. The optimal excitation distribution is believed to contribute to higher power density with the same total loss. Thus, the excitation distribution has been investigated as following.

If only the outer windings are excited with the current of I_1 , the output torque of the motor is denoted as T_1 and the copper loss of the windings is denoted as $P_{\text{loss}1}$. If only the inner windings are excited with the current of $I_2 = I_1$, the output torque is denoted as T_2 . The copper loss of the windings is denoted as $P_{\text{loss}2}$.

When the outer excitation is varied from I_1 to I_{1x} , the corresponding output torque and copper loss can be approximately derived as:

$$T_{1x} = \frac{I_{1x}}{I_1} T_1, \quad (6.3)$$

$$P_{\text{loss}1x} = \frac{I_{1x}^2}{I_1^2} P_{\text{loss}1}. \quad (6.4)$$

When the inner excitation is varied from I_2 to I_{2x} , the corresponding output torque and copper loss can be obtained as:

$$T_{2x} = \frac{I_{2x}}{I_2} T_2, \quad (6.5)$$

$$P_{\text{loss}2x} = \frac{I_{2x}^2}{I_2^2} P_{\text{loss}2}. \quad (6.6)$$

Assuming the relationship of the inner and outer excitation as:

$$I_{1x} = kI_{2x}, \quad (6.7)$$

based on the following assumption of the relationship of the respective copper loss:

$$P = P_{\text{loss}1x} + P_{\text{loss}2x} = \frac{I_{1x}^2}{I_1^2} P_{\text{loss}1} + \frac{I_{2x}^2}{I_2^2} P_{\text{loss}2} = C, \quad (6.8)$$

the total output torque can be expressed as:

$$T = T_{1x} + T_{2x} = \frac{I_{1x}}{I_1} T_1 + \frac{I_{2x}}{I_2} T_2, \quad (6.9)$$

where C is a constant value. Substituting (6.7) and (6.8) into (6.9), the expression of the total output torque T can be derived. To determine the maximum value of the total output torque T with the optimal k , one has

$$\frac{dT}{dk} = 0. \quad (6.10)$$

Calculating the differential equation above, the optimal value of k can be obtained, then the relationship of $I_{1x} = k \cdot I_{2x}$ can be determined. For the proposed SSPM motor in this paper, the k has been determined as 1.677. The calculated result shows that the coefficient k is greater than one, which means that smaller current would be applied to the inner armature windings of the stator. With the dual-electrical-port structure the flux-weakening effect can also be realized through the appropriate control of the inner windings. It would be an assistance in the braking process of the SSPM motor in EV.

The waveforms of the output torque of the SSPM motor, when only outer windings or inner windings are excited, are shown in Fig. 6.4. It can be found that much larger excitation needs to apply to the armature windings to achieve the same torque density if there is only one flux-modulated motor existed in the proposed SSPM motor. The dual-electrical-port

structure of the proposed SSPM motor has realized the sufficient utilization of the inner space of the motor.

For in-wheel direct drive of EVs, the required rotary speed of the motors should reach to about 1000 r/min. Fractional-slot windings are not suitable to a relatively high-speed motor and hence concentrated windings are employed in the proposed SSPM motor. With very short end windings, the copper loss of the SSPM motor can be significantly reduced.

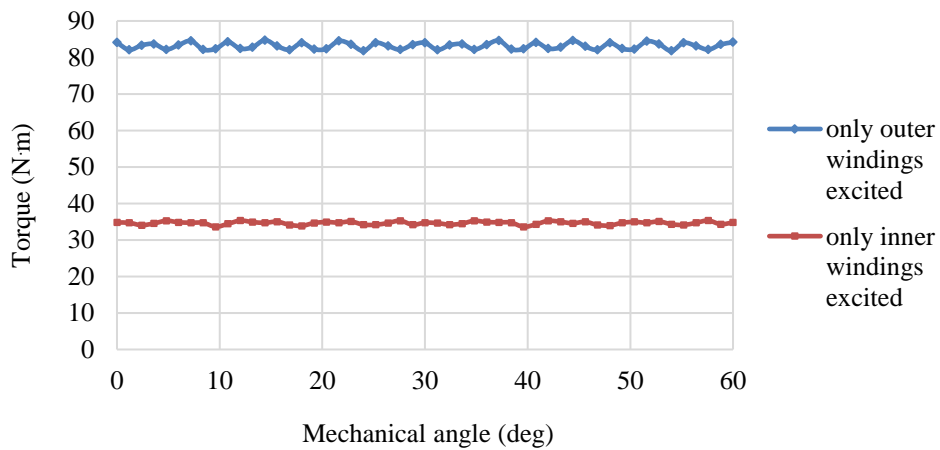


Fig. 6.4. The output torque waveforms when only one set of windings is excited.

6.4.2 Relative position between the inner rotor and the outer rotor

In the proposed SSPM motor, the inner stator and outer stator are combined into one frame sharing the same stator yoke. Hence, the relative position between the inner rotor and the outer rotor may influence the mutual effect of the magnetic fields produced by the inner motor and the outer motor. Optimal interaction can considerably improve the overall performance of the SSPM motor. Thus, the relative position between the two rotors is

required to be investigated before the two rotors being mechanically connected together as a single rotor. Fig. 6.5 shows one relative position between the inner rotor and the outer rotor. The simulation results of the investigation are summarized in Fig. 6.6. The optimal relative position can be determined from the obtained waveform.

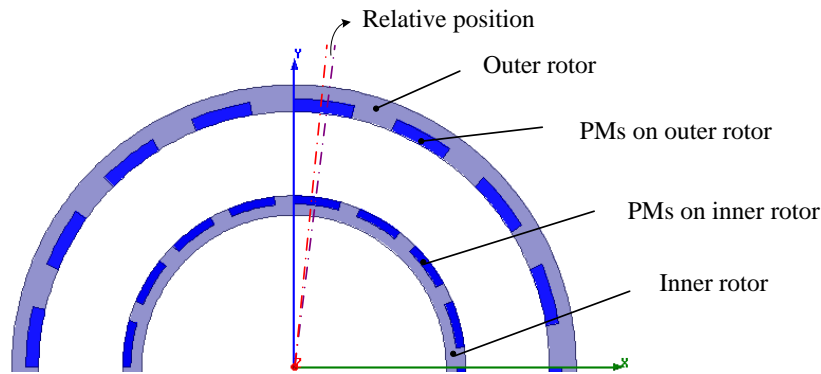


Fig. 6.5. The relative position of the inner rotor and the outer rotor.

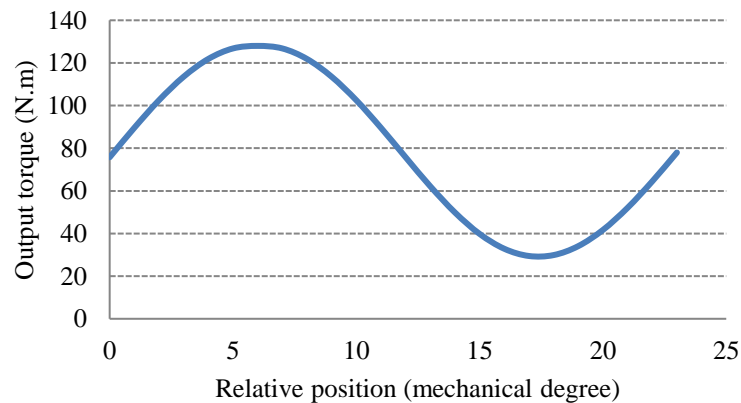


Fig. 6.6. The output torque with different relative positions of the two rotors.

6.4.3 Optimization of parameters

The pole-pair/tooth/slot combinations and local magnetic saturation at the iron cores are the main causes of torque ripple. Therefore, the combination of the pole pairs of the PMs, the number of slots, the arrangement of the armature windings, the winding coefficient, and the physical dimensions are included in the optimal design. In this work, the pole-pair/tooth/slot combination has been determined in the previous research for the further parameter

optimization.

A parameterized model of the proposed SSPM motor with synthetic slots is established to accomplish automatic parameter optimization process. The outer diameter and the active length of the SSPM motor are determined by the space available in EVs. Beyond that, all other parameters of the motor should be optimally designed, such as the sizes of the two rotors and the stator, the slot sizes, as well as the sizes of the PMs on both the stator and the rotor.

The flow chart of the parameter optimization is shown in Fig. 6.7. An in-house developed optimization software package, including multi-objective and single-objective algorithms, has been employed to the optimization of the SSPM motor. The software can read the design data file from the program of finite element method (FEM) and utilize mathematical optimization algorithms to obtain a set of optimized candidate designs. With the customer interface, it is obviously convenient to set the variable ranges and the corresponding steps, as well as the population and the maximum evaluations.

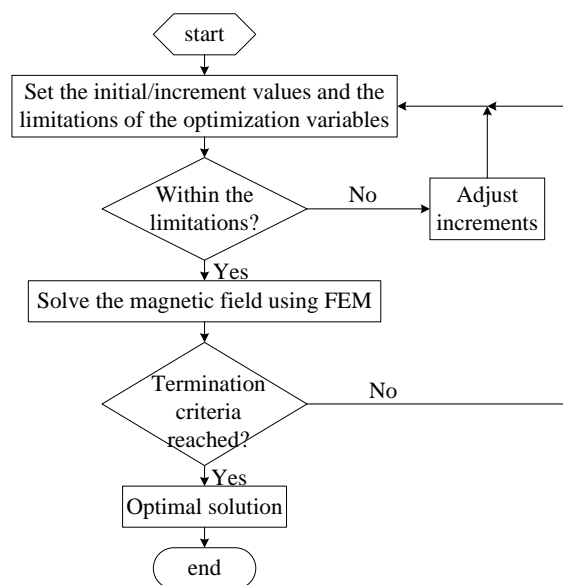


Fig. 6.7. The flow chart of the parameter optimization of the SSPM motor.

The key design data of the proposed SSPM motor are listed in Table 6.1. The design parameters are analyzed systematically and determined after many times of FEM computations. To reduce the total computing time, a parallel computing method is engaged in the optimization process.

Table 6.1 Key design data of the proposed SSPM motor

Parameters	Initial value	Final value
Thickness of the outer rotor	10.10 mm	11.40 mm
Thickness of the PMs on the outer rotor	5.40 mm	5.40 mm
Thickness of the inner rotor	12.90 mm	8.20 mm
Thickness of the PMs on the inner rotor	3.00 mm	3.50 mm
The ratio of the PMs on the outer rotor	0.58	0.6
The ratio of the PMs on the inner rotor	0.58	0.7
Thickness of the PMs in the outer stator rabbet	1.50 mm	3.00 mm
Width of the PMs in the outer stator rabbet	7.07 mm	7.85 mm
Thickness of the PMs in the outer stator slots	5.28 mm	4.56 mm
Width of the PMs in the outer stator slots	1.16 mm	1.98 mm
Thickness of the PMs in the inner stator rabbet	3.00 mm	3.10 mm
Width of the PMs in the inner stator rabbet	4.14 mm	5.34 mm
Slot depth in the outer stator	12.40 mm	9.00 mm
Slot depth in the inner stator	11.50 mm	9.00 mm
Thickness of the stator yoke	3.00 mm	10.00 mm

6.5 Simulation results and analysis

6.5.1 Performance comparison

The magnetic fields of the SSPM motor and a conventional PM motor are analyzed using time-stepping FEM [F22-F24]. The main performances of the proposed SSPM motor with initial and optimal configurations are compared and summarized in Table 6.2. One can see that the torque capability of the SSPM motor is enhanced considerably with small decrease of efficiency compared with the conventional PM motor. The influence of the excitation distribution on the performance of the SSPM motor is also reflected in the table. The output torque of the SSPM motor with excitation distribution optimization is 11.4% higher than that of with initial design. The efficiency of the proposed SSPM motor may be lower when considering the losses in the permanent magnets. In the optimal SSPM motor, the analyzed solid loss in PMs is 158W, so the efficiency will be reduced to 90.54%.

Table 6.2 Performance of the proposed SSPM motor

Item	Output torque (N·m)	Core loss (W)	Copper loss (W)	Efficiency (%)
Conventional PM motor	85.0	534	101	93.34
SSPM motor with initial design	120.7	528	538	92.21
SSPM motor with parameter optimization	125.5	684	581	91.22
SSPM motor with optimization of excitation distribution	134.5	687	627	91.47

6.5.2 Optimized configuration

The optimized configuration of the proposed SSPM motor is shown in Fig. 6.8. The width of the stator slots has been enlarged and the sizes of the PMs are more visible. The basic

schematic installation topology is shown in Fig. 6.9.

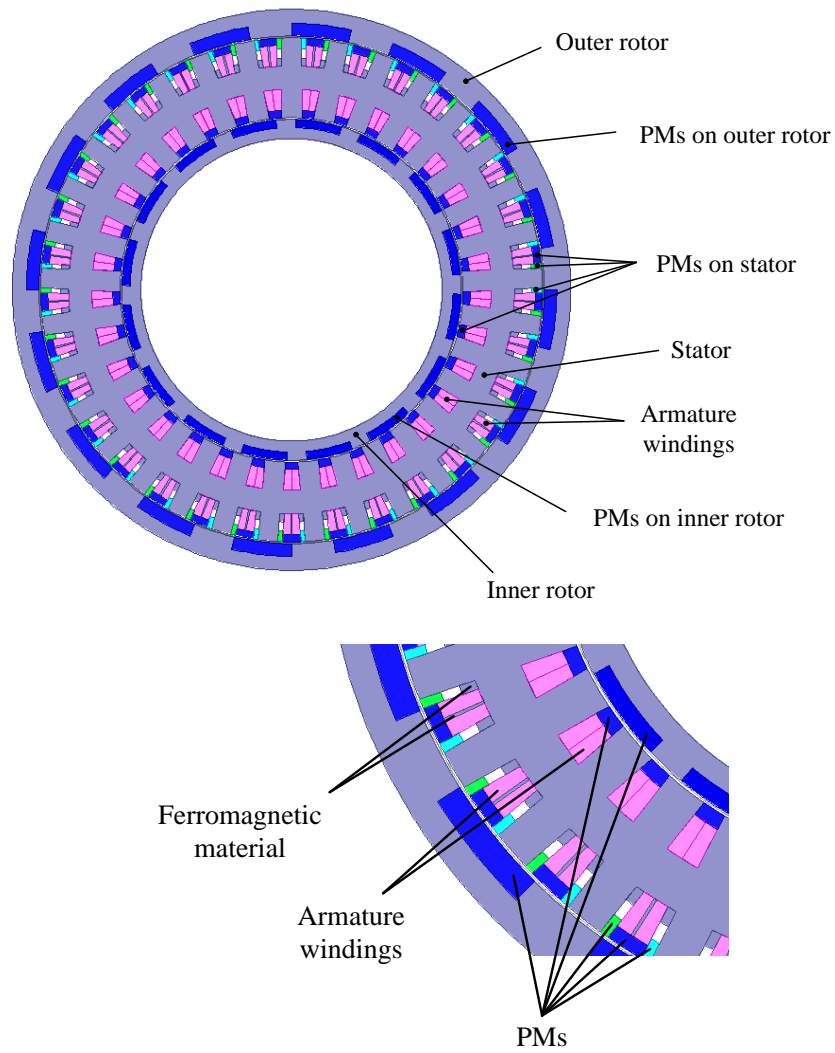


Fig. 6.8. The optimized configuration of the proposed SSPM motor and partially enlarged detail.

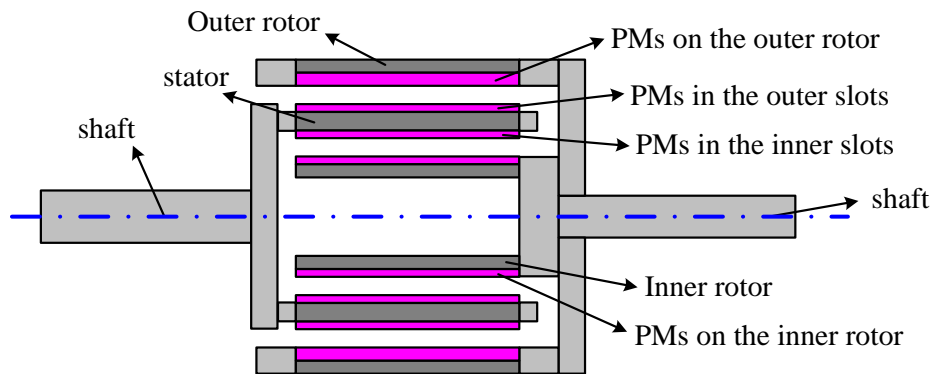


Fig. 6.9. The schematic installation topology of the proposed SSPM motor.

6.5.3 Torque and induced voltage

The waveform of the output torque of the SSPM motor is shown in Fig. 6.10. The waveforms of the induced voltage of the two sets of three-phase windings are shown in Fig. 6.11. Fig. 6.12 and Fig. 6.13 display the induced voltage versus the input current of the outer Phase A and the inner Phase A. It intuitively indicates that the proposed SSPM motor has high power factor, since the current and the voltage are nearly in phase.

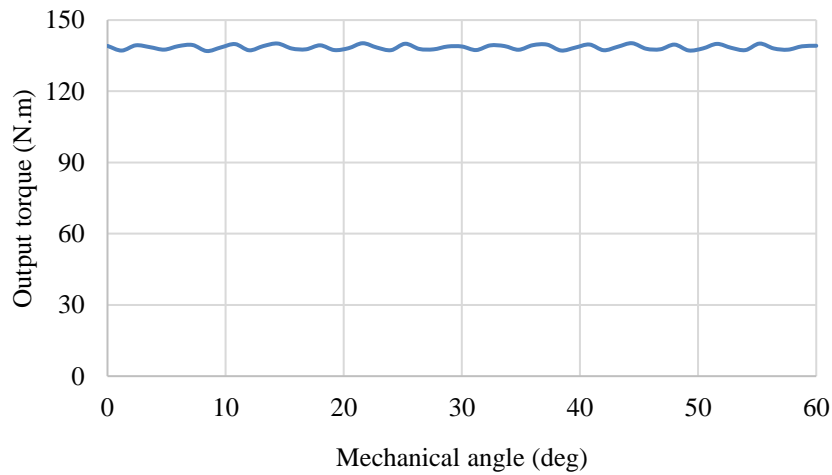


Fig. 6.10. The output torque waveform.

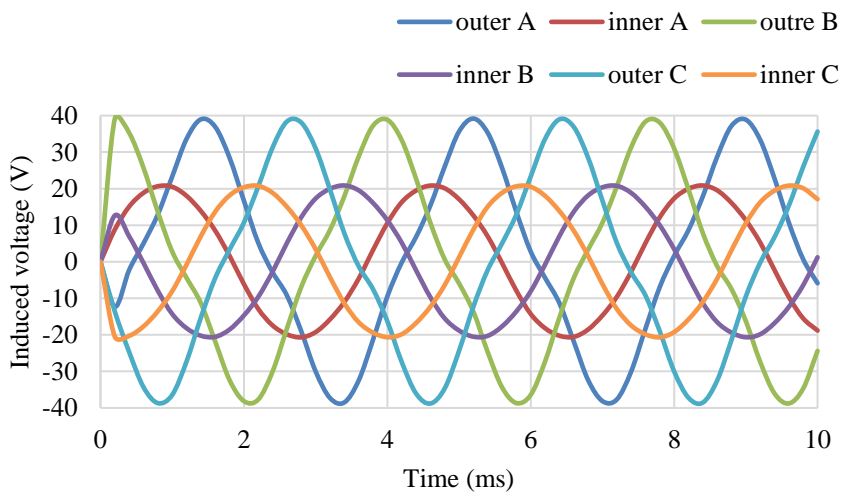


Fig. 6.11. The induced voltage waveform of the windings.

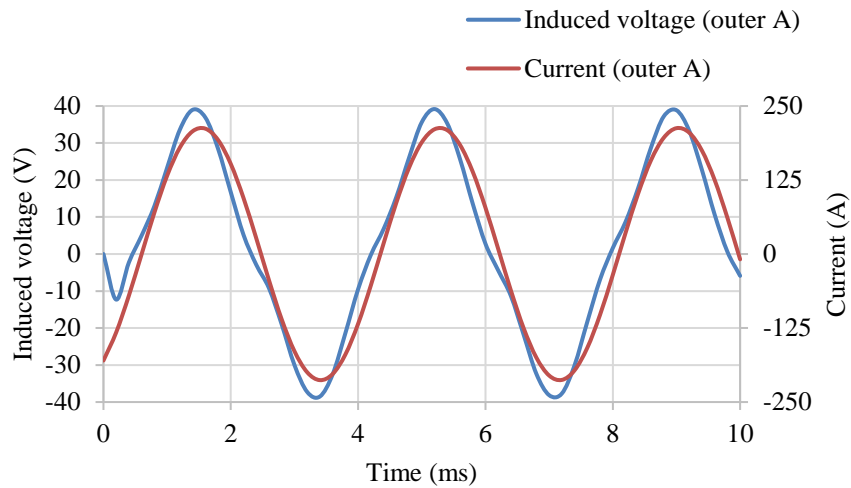


Fig. 6.12. The induced voltage vs input current of the outer winding.

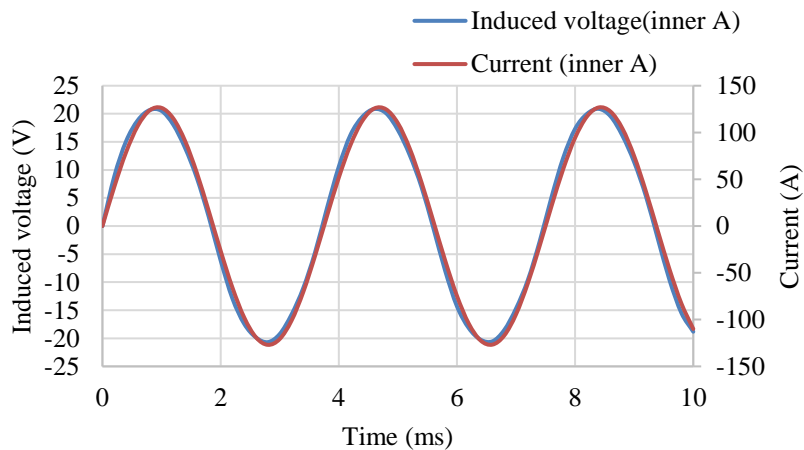


Fig. 6.13. The induced voltage vs input current of the inner winding.

6.5.4 Harmonics analysis

Fig. 6.14 and Fig. 6.15 present the radial flux density in the outer airgap and inner airgap, respectively. Each harmonic component has been clearly exhibited. The amplitudes of the fundamental components of magnetic fields in the outer and inner airgaps are about 1.75T and 1.45T, respectively. In the proposed SSPM motor, the number of pole pairs of the PMs on the rotor is 16 and the number of pole pairs of the stator armature windings is 17. Thus, the main harmonic components of the produced magnetic fields are 16th, 17th, 32nd, 33rd,

and 49th.

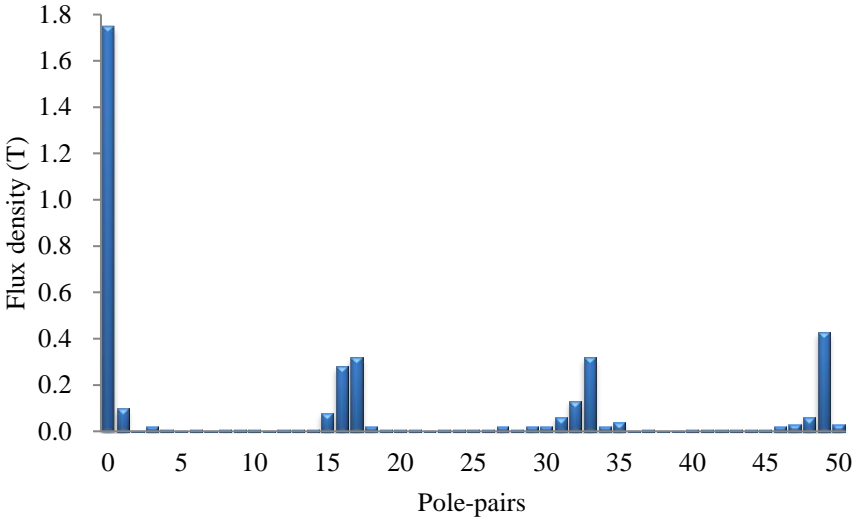


Fig. 6.14. Radial flux density in the outer airgap.

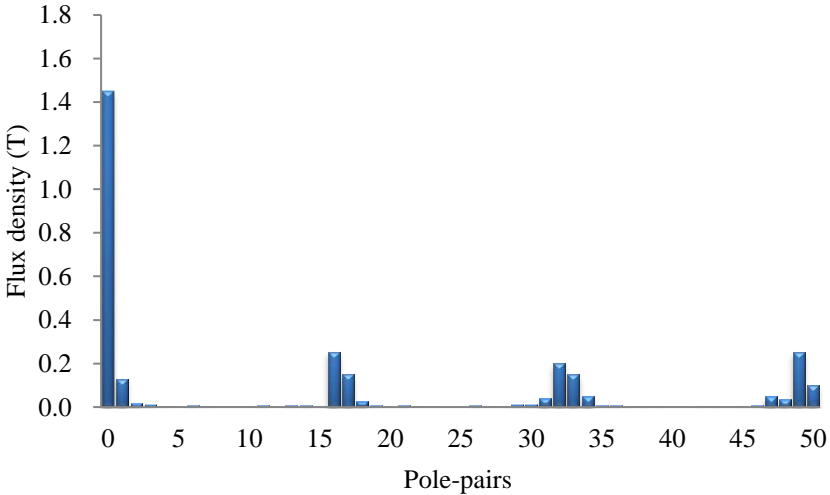


Fig. 6.15. Radial flux density in the inner airgap.

6.5.5 Flux and magnetic field distributions

The flux line contour and magnetic density distribution of the SSPM motor are shown in Fig. 6.16 and Fig. 6.17, respectively.

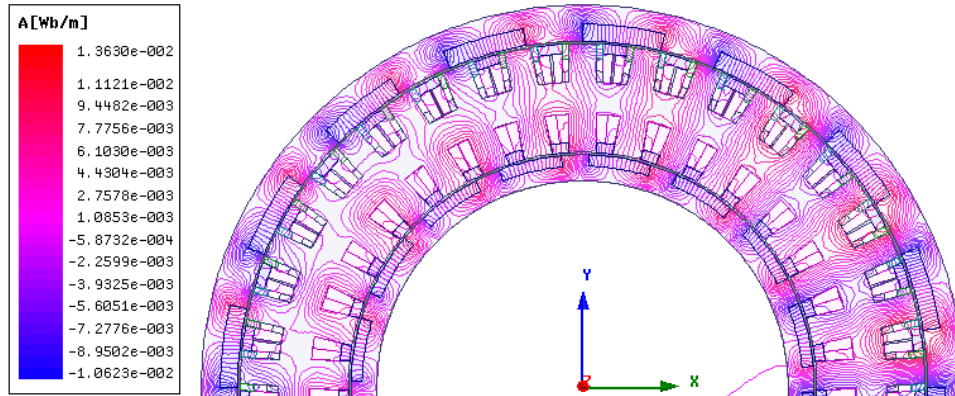


Fig. 6.16. Flux line contour.

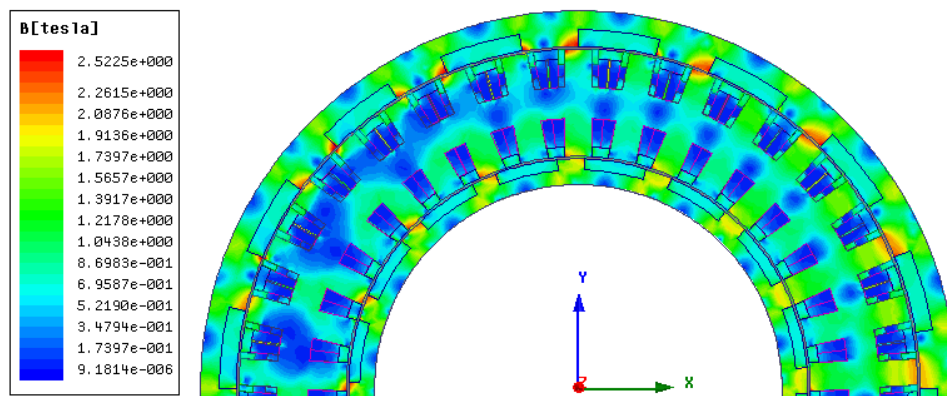


Fig. 6.17. Magnetic density distribution.

6.6 Prototype and experimental investigation

6.6.1 Prototyped SSPM motor

Two prototypes of the proposed synthetic-slot PM motor, as shown in Fig. 6.8, are fabricated for laboratory experiments and on-vehicle test of a two-wheel-drive EV. Fig. 6.18 shows the combined rotor with PMs mounted on the rotor surface (a), the stator with armature windings and PMs (b), and the packaged motor with end cover and bearing (c).



(a)



(b)



(c)

Fig. 6.18. The prototype of the proposed synthetic-slot PM motor.

6.6.2 Designed EV frame

To realize two SSPM motor prototypes being installed on the rear wheels of an EV frame, a simulation model of the EV frame is designed and established using software Solidworks. Fig. 6.19 displays the designed configuration of the EV frame and the connection structure

between the wheel and the vehicle.

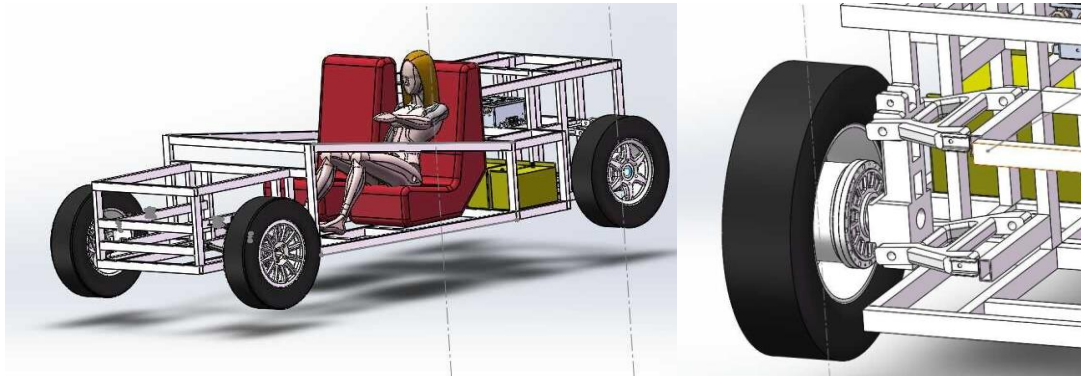


Fig. 6.19. The model of the automobile framework and the connection structure between the wheel and the frame.

6.6.3 Test bench and real EV frame

A test system has been established in the laboratory to test the performance of the prototype, as shown Fig. 6.20. Fig. 6.21 (a) shows the fabricated EV frame to perform as an experiment platform. For the convenience of transport and storage, the EV frame is manufactured to be detachable. Fig. 6.21 (b) displays one SSPM motor housed inside the wheel hub of a R15 tyre, connected with an oil brake. Fig. 6.21 (c) shows the complete vehicle control system and the lithium batteries serving as the power supply. The voltage of power supply is 72V. The control system is developed based on Digital Signal Processor (DSP). With the dual-electrical-port structure, the proposed SSPM motor can be controlled more flexibly. More importantly, large bus voltage can be avoided in the actual control process.

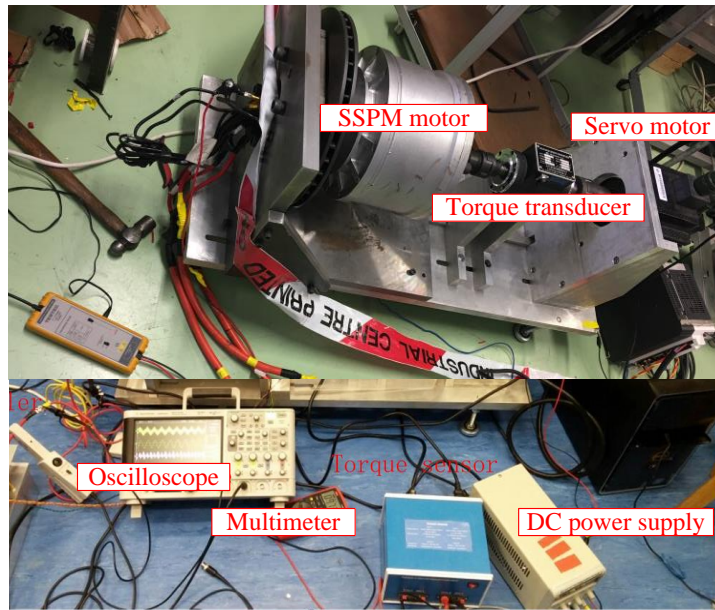


Fig. 6.20. The test system of the proposed SSPM motor.

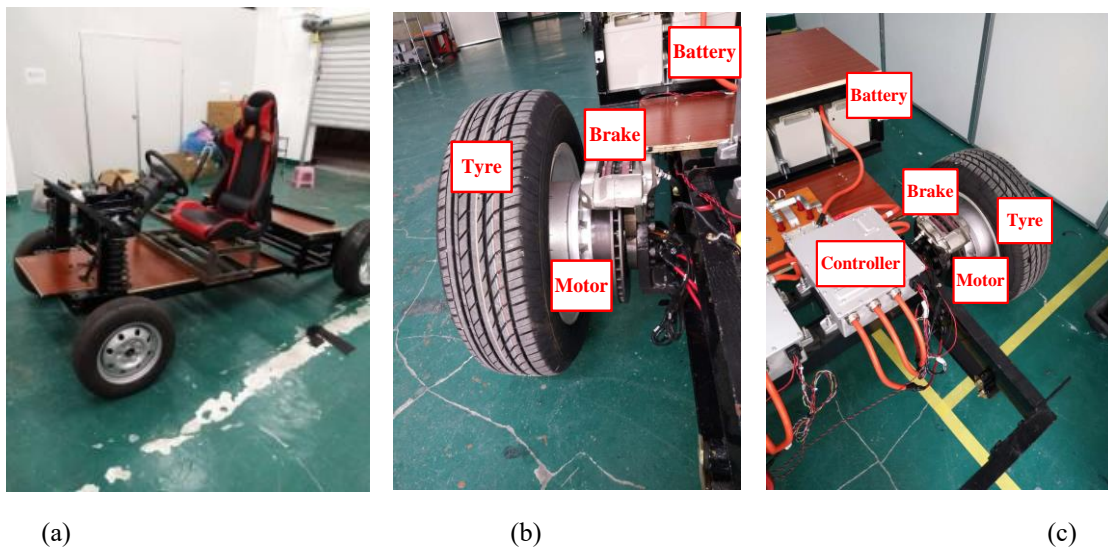


Fig. 6.21. The real EV frame with the SSPM motors, the controllers and the power supply.

6.6.4 Back EMF

In the no-load test, the peak to peak values of the back electromagnetic force (EMF) of the windings are measured when the rotor rotates at the speed of 100 r/min, 200 r/min, 300 r/min, 400 r/min, 600 r/min, 800 r/min, 1000 r/min, respectively. Fig. 6.22 and Fig. 6.23 present the simulation and experimental induced voltage of the outer and inner windings when the

rotor speed is 100 r/min, respectively. Fig. 6.24 and Fig. 6.25 show the simulation and experimental induced voltage of the outer and inner windings when the rotor speed is 200 r/min, respectively. Fig. 6.26 and Fig. 6.27 display the simulation and experimental induced voltage of the outer and inner windings when the rotor speed is 300 r/min, respectively. The data are collected and listed in Table 6.3. The comparison indicates that the simulation results of the no-load back EMF of the windings are verified by the experimental results. The measurements of the resistance and inductance of the windings of the SSPM motor are conducted.

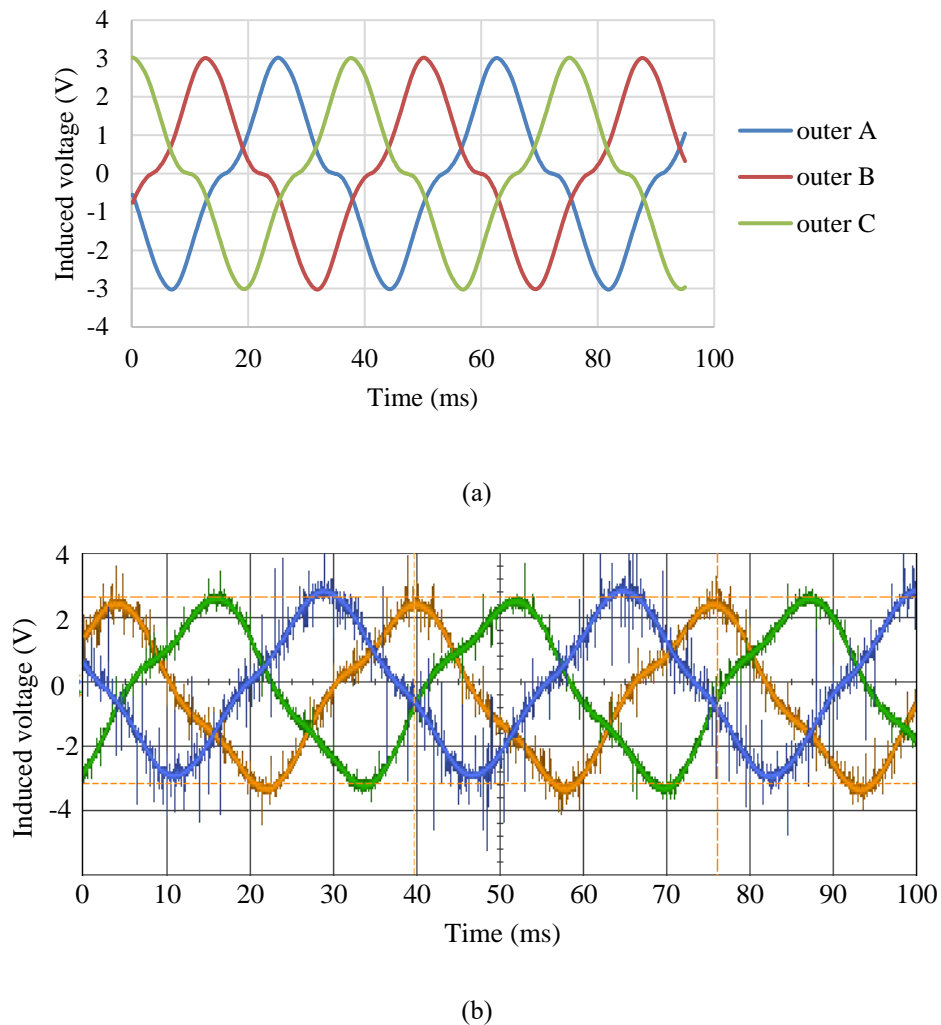
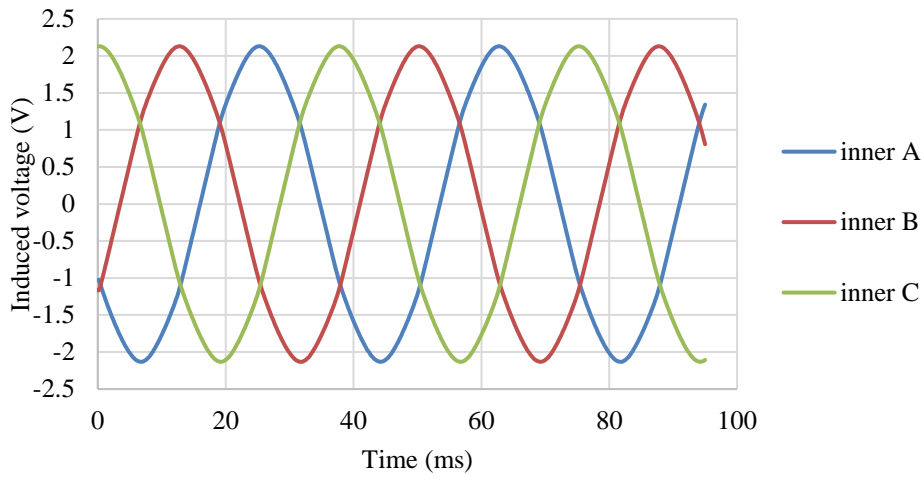
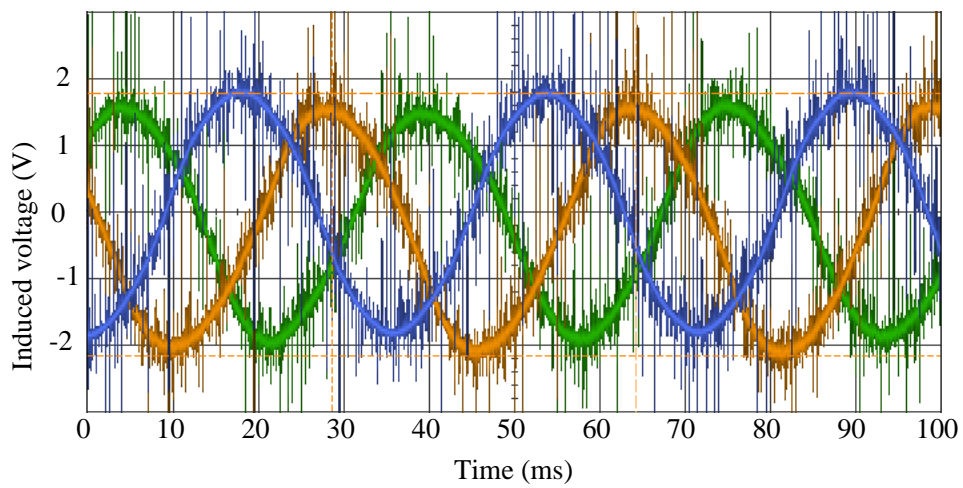


Fig. 6.22. The simulated and experimental no-load back EMF of the outer windings of the proposed SSPM motor when the speed is 100 r/min.

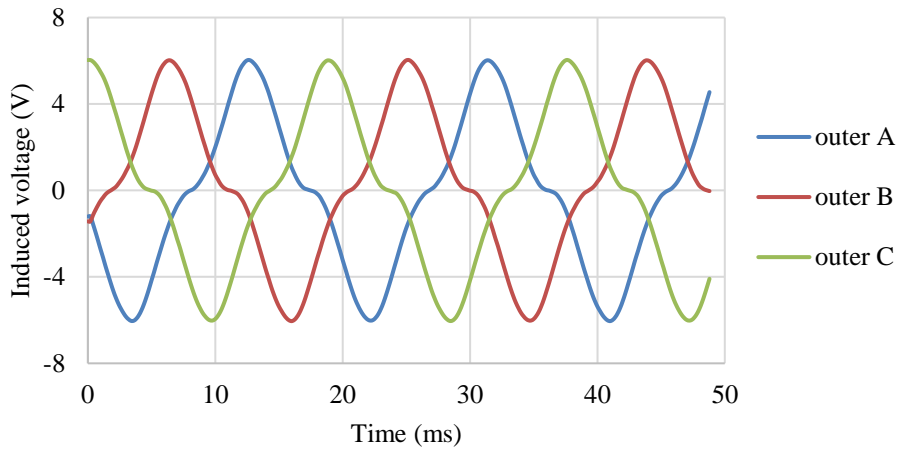


(a)

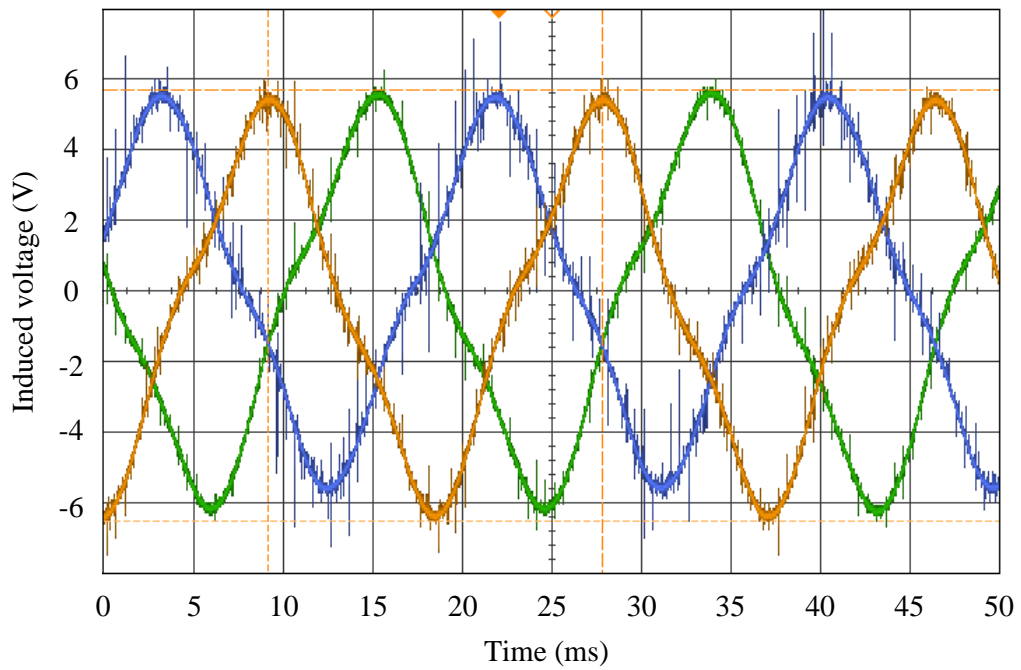


(b)

Fig. 6.23. The simulated and experimental no-load back EMF of the inner windings of the proposed SSPM motor when the speed is 100 r/min.

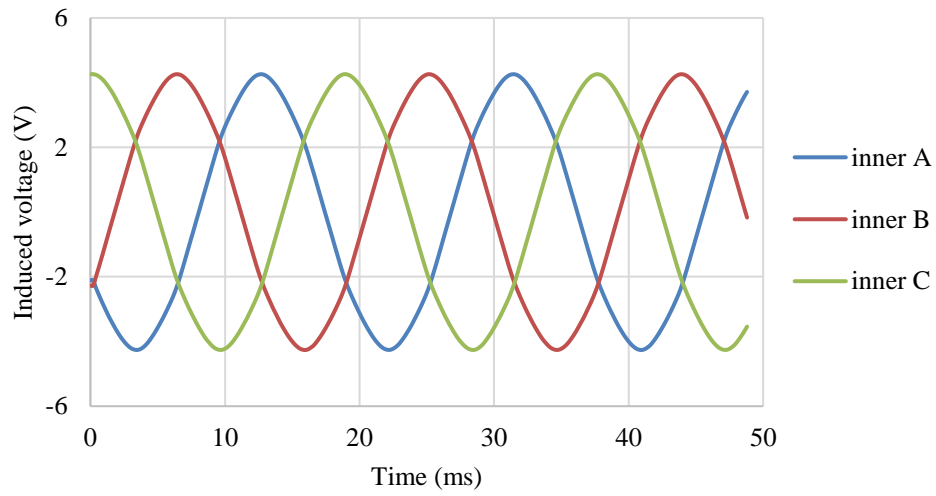


(a)

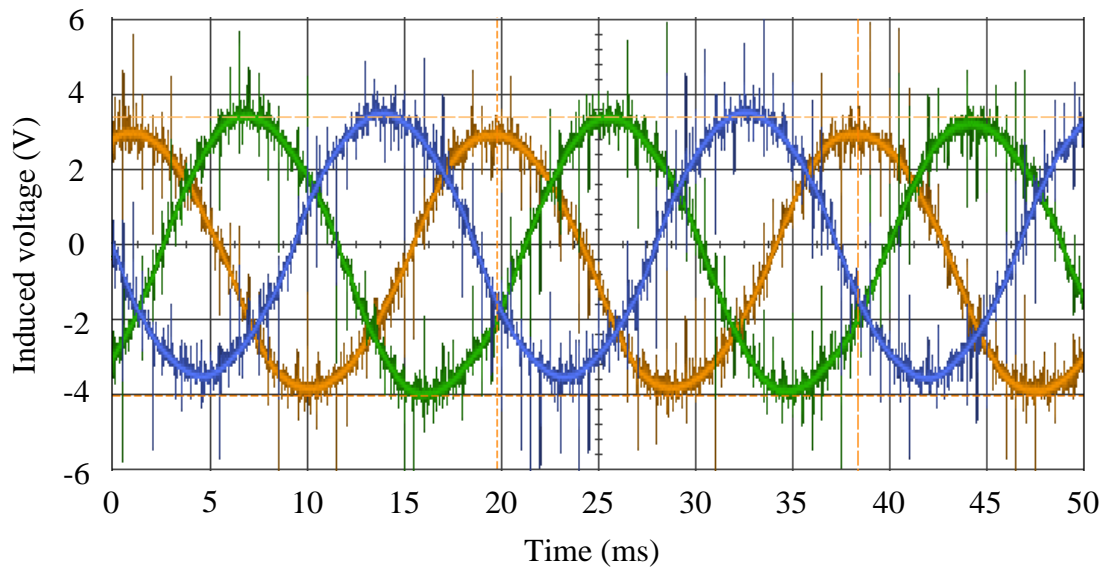


(b)

Fig. 6.24. The simulated and experimental no-load back EMF of the outer windings of the proposed SSPM motor when the speed is 200 r/min.

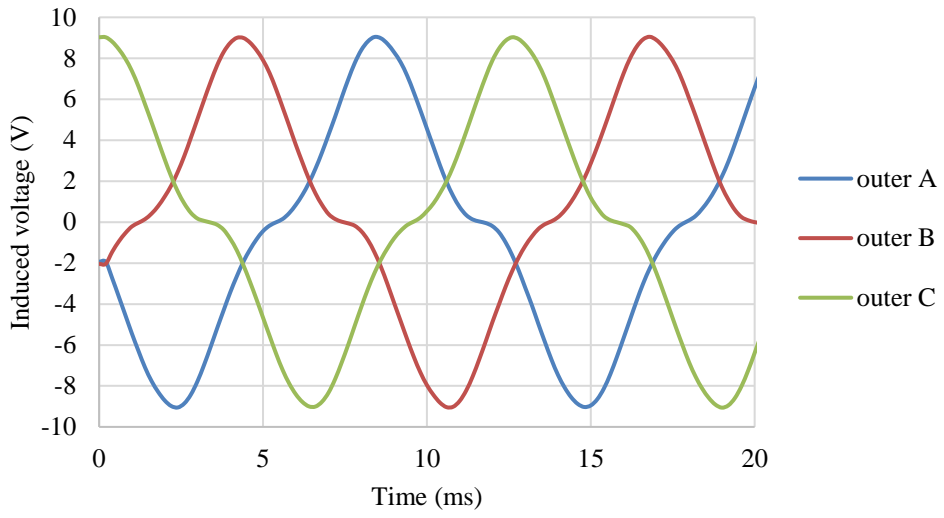


(a)

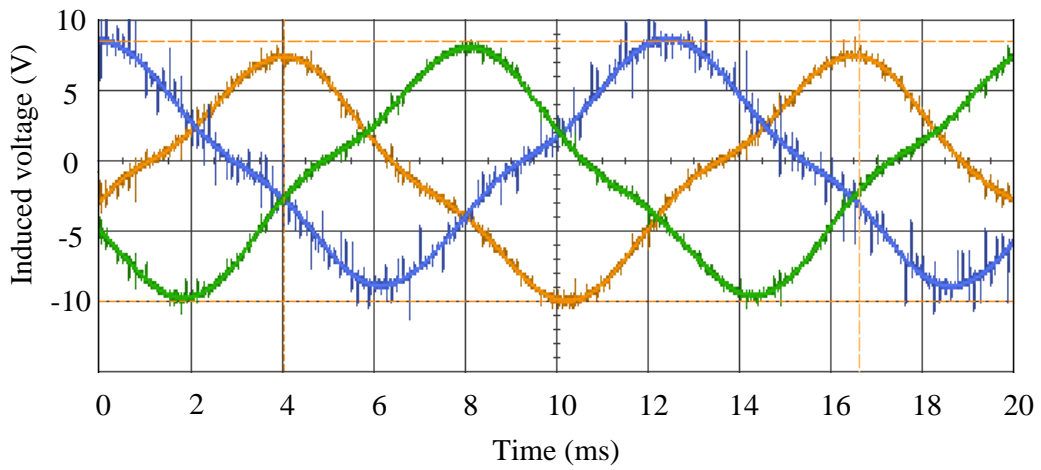


(b)

Fig. 6.25. The simulated and experimental no-load back EMF of the inner windings of the proposed SSPM motor when the speed is 200 r/min.

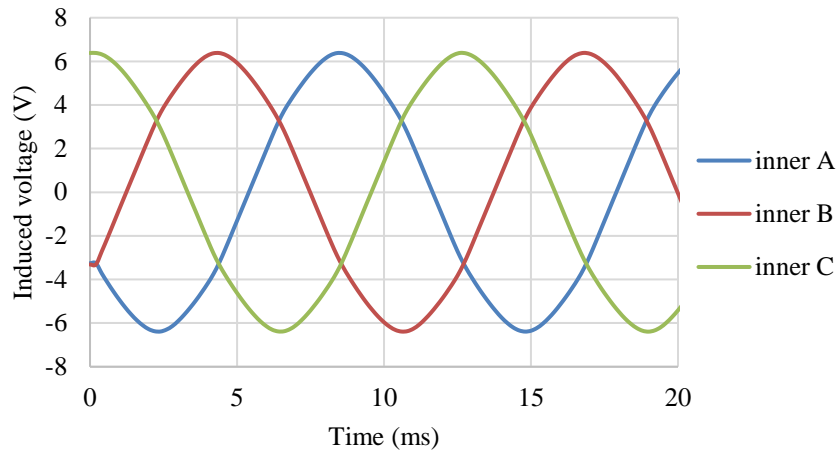


(a)

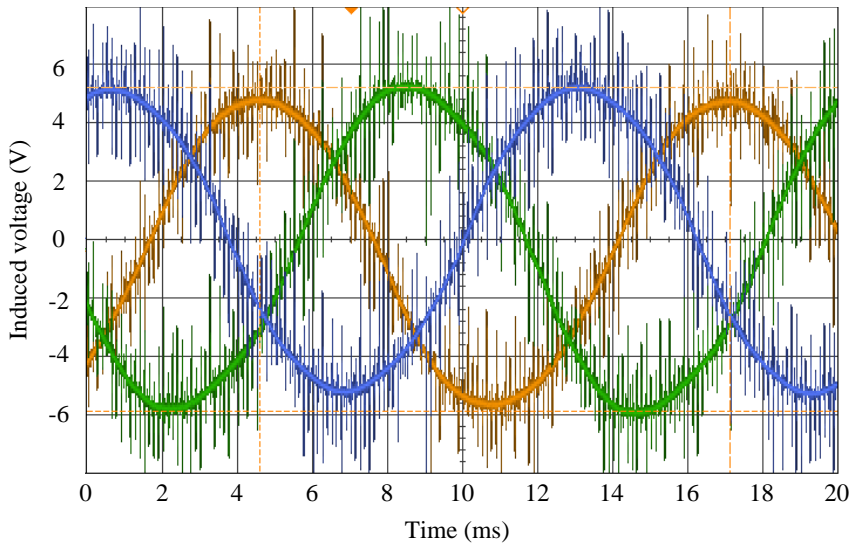


(b)

Fig. 6.26. The simulated and experimental no-load back EMF of the outer windings of the proposed SSPM motor when the speed is 300 r/min.



(a)



(b)

Fig. 6.27. The simulated and experimental no-load back EMF of the inner windings of the proposed SSPM motor when the speed is 300 r/min.

Table 6.3 Peak to peak values of the no-load back EMF of the windings

Item	100 r/min	200 r/min	300 r/min
Simulated back EMF of outer windings	6.0V	12.0V	18.0V
Experimental back EMF of outer windings	5.78V	12.18V	18.50V
Simulated back EMF of inner windings	4.2V	8.5V	12.7V
Experimental back EMF of inner windings	3.95V	7.45V	11.08V

6.6.5 Inductance test

Fig. 6.28 summarizes the self and mutual inductance of the armature windings.

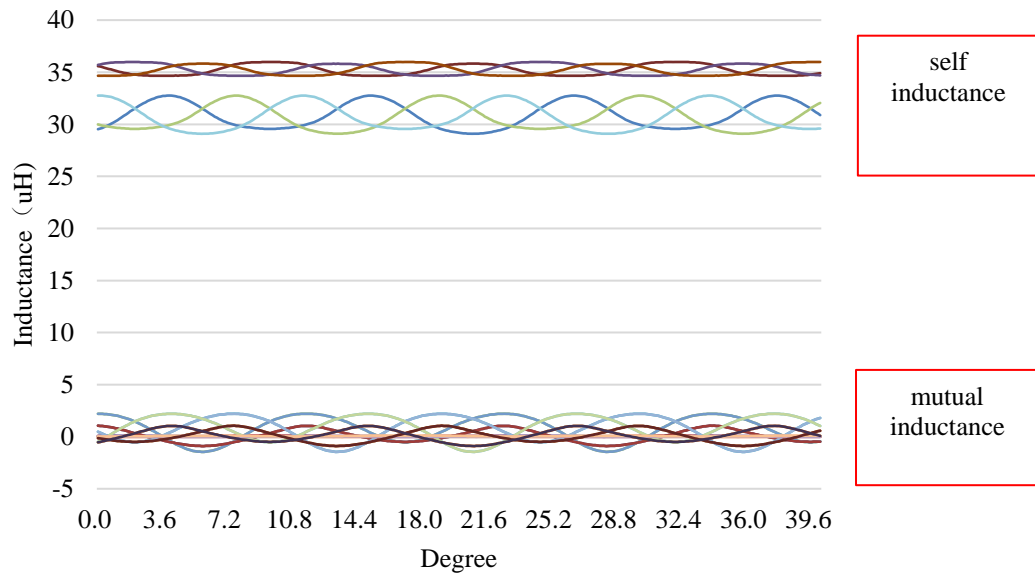


Fig. 6.28. The self and mutual inductance of the windings.

6.6.6 No-load mechanical loss

To measure the mechanical loss of the SSPM motor, a servo motor is performed to drive the SSPM motor rotating at different speeds while the armature windings of the motor are in open circuit. In this case all the output power of the servo motor is considered as the mechanical loss of the SSPM motor. Fig. 6.29 shows the no-load mechanical loss when the motor rotates at different speeds.

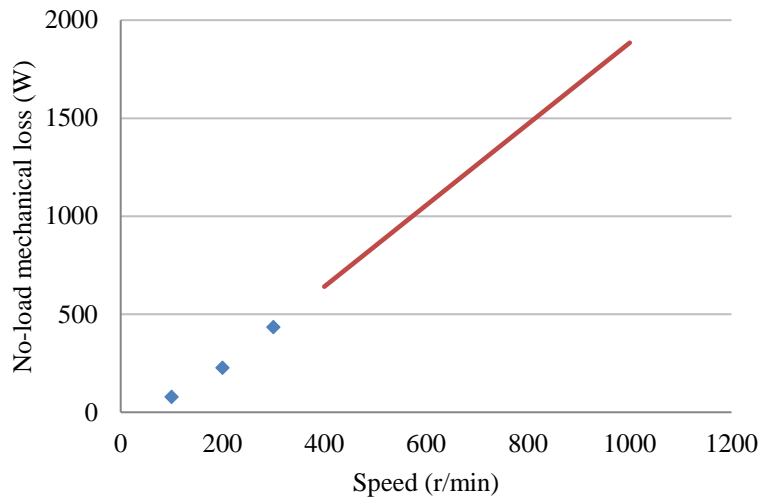


Fig. 6.29. The no-load mechanical loss of the proposed SSPM motor.

6.6.7 Loaded winding current

With the dual-electrical-port structure, the electromagnetic torque of the proposed SSPM motor is mainly determined by the excitation of the outer and inner windings, as well as the PMs. The relationship between the electromagnetic torque and the winding excitation has been investigated. The electromagnetic torque may be proportional to the product of the sum of the two currents of the outer and inner windings. It is believed that the saturation situation appeared in the stator core may affect this relationship. If the outer windings and inner windings are connected in series, the electromagnetic torque may be proportional to the square of the winding current. Fig. 6.30 shows the relationship of the electromagnetic torque and the winding current.

Fig. 6.31 displays the winding current under certain load conditions when the SSPM motor rotates at the speed of 100 r/min. Fig. 6.32 displays the winding current under certain load conditions when the SSPM motor rotates at the speed of 200 r/min. Fig. 6.33 displays the winding current under certain load conditions when the SSPM motor rotates at the speed of

300 r/min. During the actual control process, the SSPM motor is supplied with pulse-width modulation (PWM) voltages.

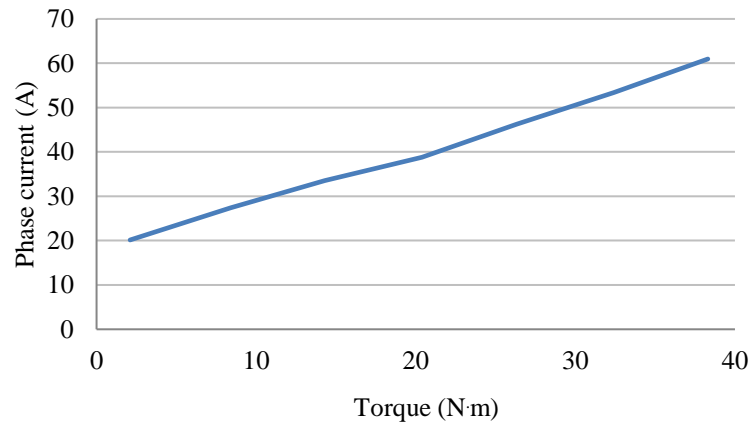


Fig. 6.30. The relationship of electromagnetic torque and the winding current.

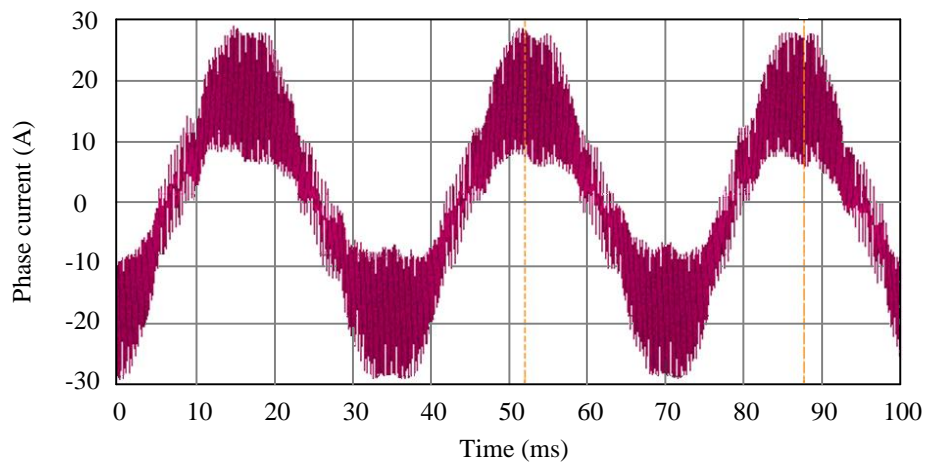


Fig. 6.31. The winding current under load conditions when the speed is 100 r/min.

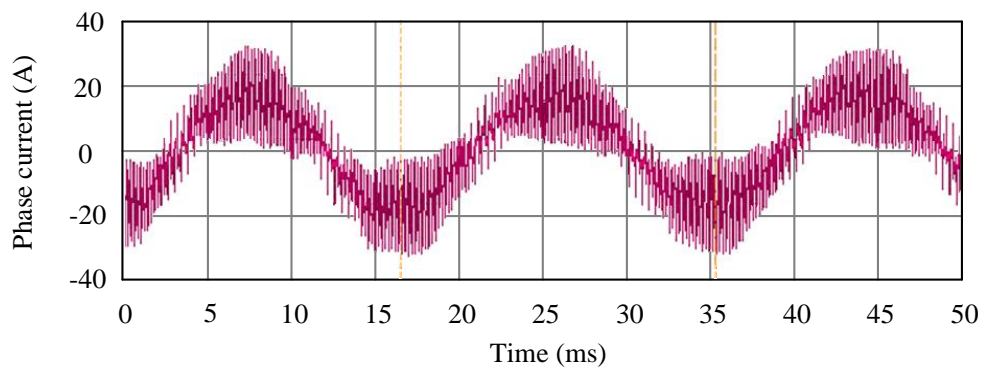


Fig. 6.32. The winding current under load conditions when the speed is 200 r/min.

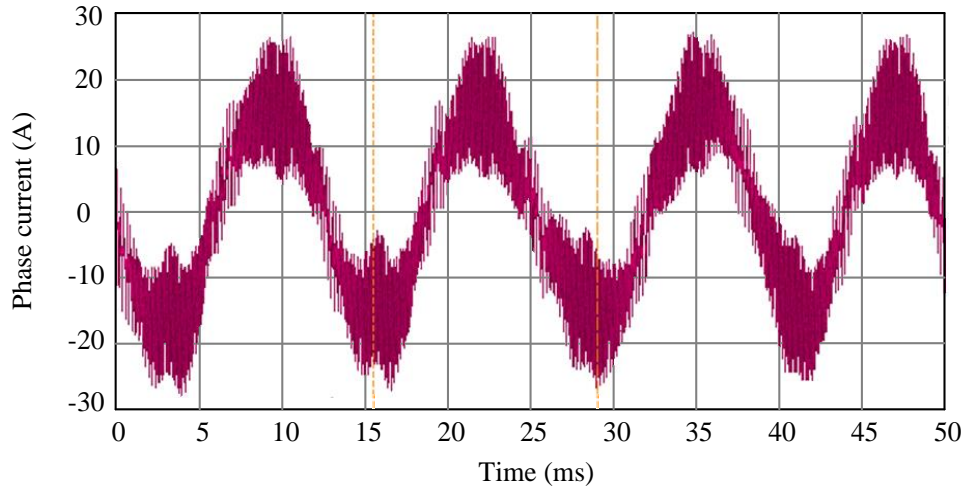


Fig. 6.33. The winding current under load conditions when the speed is 300 r/min.

6.6.8 Mechanical characteristic

The mechanical characteristic of the proposed SSPM motor is shown in Fig. 6.34. It indicates that the motor keeps operating in constant-torque mode below the base speed and the phase angle of inner excitation would be adjusted to realize flux-weakening mode for high speed operation.

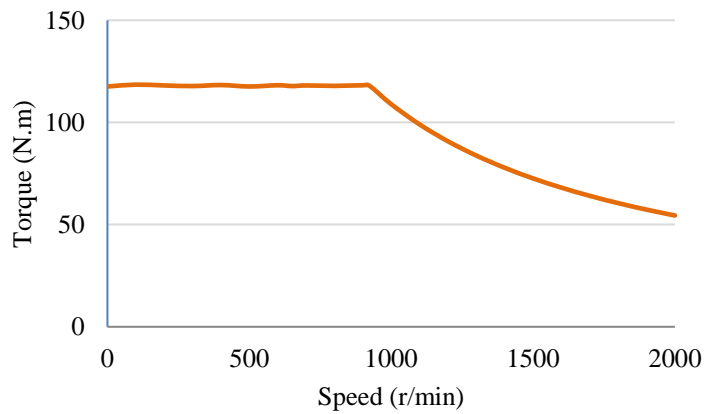


Fig. 6.34. The mechanical characteristic of the proposed SSPM motor.

6.6.9 Efficiency map

The efficiency map of the SSPM motor is drawn as Fig. 6.35. The prototypes of the SSPM motor were fabricated only to conduct the laboratory experiments, and the new structure was unfamiliar to the workers in factory to process. The mechanical loss may be too large resulting from low machining precision and poor coaxiality. Therefore, the experimental efficiency is lower than the corresponding simulation results. The efficiency map indicates that the efficiency of the SSPM motor under the condition of the rated load and operating at rated speed is about 83%.

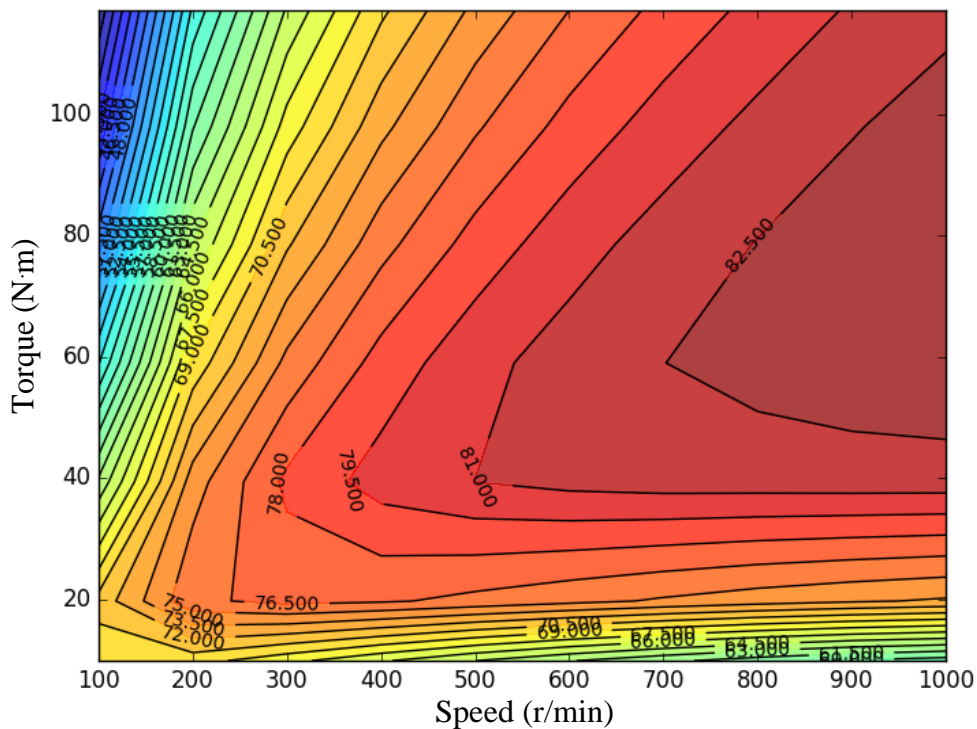


Fig. 6.35. The efficiency map of the proposed SSPM motor.

6.6.10 On-vehicle test

The EV has completed a testing of short operation in campus. Fig. 6.36 shows the recorded operation state of the vehicle, including the acceleration, deceleration and reverse. The

corresponding torque and speed are presented clearly in the figure.

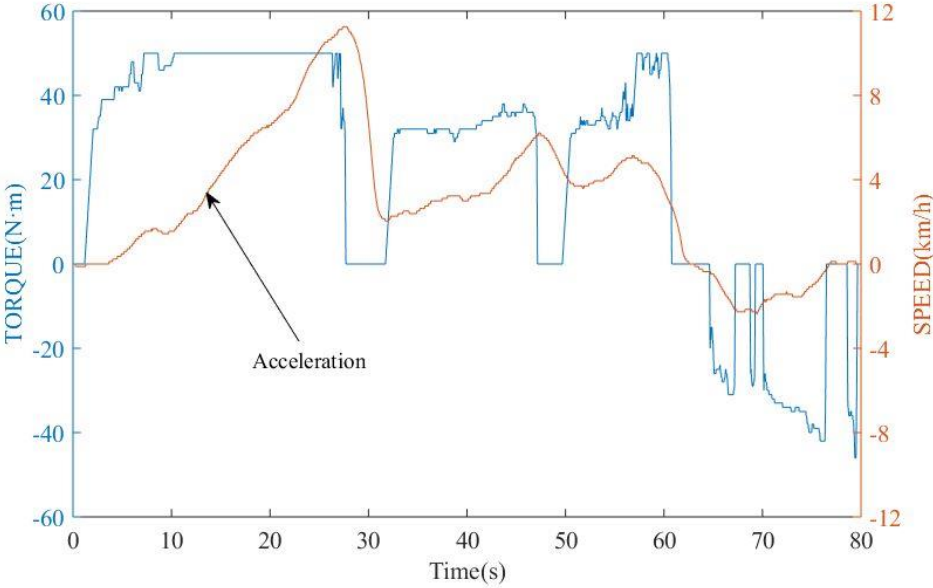


Fig. 6.36. The operation condition of the EV in low speed.

6.7 Conclusion

A dual-electrical-port synthetic-slot permanent-magnet (SSPM) motor for in-wheel direct drive in EVs is proposed in this chapter. The torque capability of the proposed SSPM motor is enhanced significantly with similar efficiency compared with a conventional PM motor. The proposed SSPM motor can produce 42% higher torque compared with the conventional one. The output torque of the SSPM motor with excitation distribution optimization has been promoted 11.4% more than that of initial design. The experimental results and on-vehicle testing results have verified the performance of the proposed SSPM motor for EV applications.

Reference Part F

- [F1] M. Brenna, F. Foiadelli, and M. Longo, "The exploitation of vehicle-to-grid function for power quality improvement in a smart grid," *IEEE Trans. Intell. Transport. Syst.*, vol. 15, no. 5, pp: 2169-2177, Oct. 2014.
- [F2] Yimin Zhou and Xiaoyun Li, "The state-of-art of the EV charging control strategies," *Proceedings of the 34th Chinese Control Conference*, Hangzhou, China, July 28-30, 2010, pp: 7916-7921.
- [F3] Rong Yu, Weifeng Zhong, and Shengli Xie, "Balancing power demand through EV mobility in vehicle-to-grid mobile energy networks," *IEEE Trans. Ind. Informat.*, vol. 12, no. 1, pp: 79-90, Feb. 2016.
- [F4] Kun Wang, Liqiu Gu, and Xiaoming He, "Distributed energy management for vehicle-to-grid networks," *IEEE Network*, vol. 31, no. 2, pp: 22-28, Mar. 2017.
- [F5] C. J. Ifedi, B. C. Mecrow, T. M. Brockway, et al., "Fault-tolerant in-wheel motor topologies for high-performance electric vehicles," *IEEE Trans. Ind. Appl.*, vol. 49, no. 3, pp. 1249-1257, May-June 2013.
- [F6] S. P. Nikam, V. Rallabandi, and B. G. Fernandes, "A high-torque-density permanent-magnet free motor for in-wheel electric vehicle application," *IEEE Trans. Ind. Appl.*, vol. 48, no. 6, pp. 2287-2295, Nov.-Dec. 2012.
- [F7] C. Liu, "Design of a new outer-rotor flux-controllable Vernier PM in-wheel motor drive for electric vehicle," *Proceeding of ICEMS*, pp. 1-6, 20-23 Aug. 2011.
- [F8] K. Atallah, J. Rens, S. Mezai, and D. Howe, "A novel 'Pseudo' direct-drive brushless permanent magnet machine," *IEEE Trans. Magn.*, vol. 44, no. 11, pp: 4349-4352, Nov. 2008.
- [F9] B. Hredzak and S. Gair, "Elimination of torque pulsations in a direct drive EV wheel motor," *IEEE Trans. Magn.*, vol. 32, no. 5, pp: 5010-5012, Sep. 1996.
- [F10] S. L. Ho, S. Niu, and W. N. Fu, "Transient analysis of a magnetic gear integrated brushless permanent magnet machine using circuit-field-motion coupled time-stepping finite element method," *IEEE Trans. Magn.*, vol. 46, no. 6, pp: 2074-2077, 2010.
- [F11] Jian Linni, K. T. Chau and J. Z. Jiang, "A magnetic-gear outer-rotor permanent-magnet brushless machine for wind power generation," *IEEE Trans. Ind. Appl.*, vol. 45, no. 3, pp. 954-962, May-June 2009.

- [F12] L. L. Wang, J. X. Shen, Y. Wang and K. Wang, "A novel magnetic-g geared outer-rotor permanent-magnet brushless motor," *4th IET Conference on Power Electronics, Machines and Drives*, York, UK, 2-4 Apr. 2008, pp. 33-36.
- [F13] G. Pellegrino, A. Vagati, P. Guglielmi, and B. Boazzo, "Performance comparison between surface-mounted and interior PM motor drives for electric vehicle application," *IEEE Trans. Ind. Electron.*, vol. 59, no. 2, pp. 803-811, Feb. 2012.
- [F14] Y. Fan, L. Zhang, M. Cheng, and K. T. Chau, "Sensorless SVPWM-FADTC of a new flux-modulated permanent-magnet wheel motor based on a wide-speed sliding mode observer," *IEEE Trans. Ind. Electron.*, vol. 62, no. 5, pp. 3143-3151, May 2015.
- [F15] L. Xu, G. Liu, W. Zhao, and X. Yang, "Hybrid stator design of fault-tolerant permanent-magnet Vernier machines for direct-drive applications," *IEEE Trans. Ind. Electron.*, vol. 64, no. 1, pp. 179-190, Jan. 2017.
- [F16] M. Cheng, W. Hua, J. Zhang, and W. Zhao, "Overview of stator-permanent-magnet brushless machines," *IEEE Trans. Ind. Electron.*, vol. 85, no. 11, pp. 5087-5101, Nov. 2011.
- [F17] Z. Xiang, X. Zhu, L. Quan, Y. Du, and C. Zhang, "Multilevel design optimization and operation of a brushless double mechanical port flux-switching permanent-magnet motor," *IEEE Trans. Ind. Electron.*, vol. 63, no. 10, pp. 6042-6054, Oct. 2016.
- [F18] R. Hosoya and S. Shimomura, "Apply to in-wheel machine of permanent magnet Vernier machine using NdFeB bonded magnet - fundamental study," *8th International Conference on Power Electronics (ECCE)*, Korea, May 30 - June 3, 2011, pp. 2208-2215.
- [F19] W. N. Fu and S. L. Ho, "A quantitative comparative analysis of a novel flux-modulated permanent-magnet motor for low-speed drive," *IEEE Trans. Magn.*, vol. 46, no. 1, pp.127-134, Jan. 2010.
- [F20] S. L. Ho, S. Niu, and W. N. Fu, "Design and comparison of Vernier permanent magnet machines," *IEEE Trans. Magn.*, vol. 47, no. 10, pp. 3280-3283, 2011.
- [F21] S. Niu, S. L. Ho, W. N. Fu, and L. L. Wang, "Quantitative comparison of novel Vernier permanent magnet machines," *IEEE Trans. Magn.*, vol. 46, no. 6, pp. 2032-2035, 2010.
- [F22] W. N. Fu, P. Zhou, D. Lin, S. Stanton and Z. J. Cendes, "Modeling of solid conductors in two-dimensional transient finite-element analysis and its application to electric machines," *IEEE Trans. Magn.*, vol. 40, no. 2, pp. 426-434, Mar. 2004.

- [F23] W. N. Fu and S. L. Ho, "Enhanced nonlinear algorithm for the transient analysis of magnetic field and electric circuit coupled problems," *IEEE Trans. Magn.*, vol. 45, no. 2, pp.701-706, Feb. 2009.
- [F24] D. Lin, P. Zhou, W. N. Fu, Z. Badics and Z. J. Cendes, "A dynamic core loss model for soft ferromagnetic and power ferrite materials in transient finite element analysis," *IEEE Trans. Magn.*, vol. 40, no. 2, pp. 1318-1321, March 2004.

Chapter 7 Summary and future work

7.1 Summary

This thesis investigates a general and unified theory of flux-modulated electric machines and its application to innovation of machine topologies. The contents of this thesis are summarized as below.

Firstly, the literature review on different types of magnetic gears and flux-modulated (FM) machines is conducted, including the configuration, working theory, advantages and disadvantages. It gives a clear scope of the development of the current techniques.

Secondly, a concept of general flux-modulated electric machines (GFMMs) is proposed. A general and unified theory is introduced to explain the working principles of a basic flux-modulated motor, a flux-switching motor, a Vernier motor, and a dual-PM-excited motor with PMs on both rotor and stator.

Thirdly, a doubly-fed dual-stator (DFDS) motor based on the unified theory of GFMMs is presented. A design method using numerical finite-element method (FEM) and optimization algorithm is performed to analyze the performance of the DFDS motor. A testing platform for the prototyped DFDS motor is established for performance verification. The experimental results verify the design concept of the DFDS motor and show its outstanding potential.

Fourthly, to achieve high torque density and high efficiency, a performance comparison of dual-layer permanent-magnet-excited (DPME) motors with different PM arrangements is conducted. The results show the optimized DPME synchronous motor has higher torque capability, but the utilization of PMs should be improved further. The optimization method

for the PM arrangement can provide an effective design approach for PM machines.

Fifthly, in order to achieve higher torque density and higher efficiency, two novel PM motors in low-speed applications are proposed. A novel DPME motor, in which an extra set of iron teeth is employed in an inner stator between the PM rotor and the shaft, is introduced. It can provide additional variation of magnetic reluctance along the circumferential direction of the air-gap, and the strength of the flux modulation among the magnetic fields produced by the armature windings and the PMs is improved. The novel DPME motor has tactfully integrated the two pairs of flux-modulated motors inside one frame with one shared set of armature windings. The advantage of the novel DPME motor is that it offers much higher torque capability than its conventional counterparts, making it more competitive for low-speed high-torque applications. A novel triple-layer PM-excited (TPME) synchronous motor is further presented with the similar operating principle of the novel DPME, and it has three PM layers inside the frame. Finite-element method (FEM) of magnetic field with mechanical motion coupled computation is employed to evaluate the electromagnetic torque precisely, showcasing that the novel DPME motor can output an extra 37.5% more torque when compared to that from a conventional synchronous motor, and the proposed TPME motor can output an additional 70% more torque with a similar power efficiency when compared to that by the conventional PM synchronous motor.

Lastly, a dual-electrical-port synthetic-slot permanent-magnet (SSPM) motor is proposed. With dual-airgap configuration the torque capability of the SSPM motor can be improved by virtue of the increased total area of air-gap surface. The outer rotor and inner rotor are mechanically connected together as a single rotor to make the mechanical structure less complicated than two rotor machines. A new general pattern of a synthetic-slot structure, containing copper, permanent magnets, ferromagnetic materials, and insulators, is put forward and ingeniously employed to boost the torque density of the proposed SSPM motor.

The concentrated winding arrangement can be employed in the SSPM motor to reduce the end windings and the copper loss, even the speed of the motor for electric vehicle drive can be as high as 1000 r/min. A systematic optimization method is adopted to enhance the performance of the SSPM motor. The torque capability of the proposed SSPM motor is enhanced significantly with similar efficiency compared with a conventional PM motor. The proposed SSPM motor can produce 42% higher torque compared with the conventional one. The output torque of the SSPM motor with excitation distribution optimization has been promoted 11.4% more than that of initial design. The experimental results and vehicle-test results have verified the performance of the proposed SSPM motor for EV applications.

7.2 Future work

Although this thesis has done some researches for the general and unified theory of flux-modulated electric machines and its application to several machine topologies, there are still some aspects to be studied in the future work.

1) The unified theory of flux-modulated machines can be studied using different method, and the general model of flux-modulated machines needs to be extended further.

2) The PM arrangements and the rational utilization of the PMs in the machines need to be studied further to avoid demagnetization.

3) The structural complexity and feasibility of the machines in different applications during exploring new machine topologies need to be considered.

4) The design method of the GFMMs need to be perfect, and the optimization algorithm of the machines need to be improved.

5) More practical problems, such as technological issue and test method, need to be optimized.